

CWP-461
May 2003



Multiple scattering of surface waves

Kasper van Wijk

— Doctoral Thesis —
Geophysics

Defended on May 1, 2003

Committee Chair:	Prof. E. Craig Simmons
Advisor:	Prof. John A. Scales
Committee members:	Prof. Roelof K. Snieder
	Prof. Michael L. Batzle
	Prof. Thomas M. Boyd
	Prof. David M. Wood

Center for Wave Phenomena
Colorado School of Mines
Golden, Colorado 80401
(1) 303 273-3557

Abstract

Multiple scattering of elastic waves in disordered media offers a complexity of the wave field that is challenging to unravel. The subsurface is an example of a medium with disordered inhomogeneity at all scales. However, because waves that bounce around for a long time and/or distance sample the Earth well, they potentially offer great insight into the structure of the subsurface.

A surface wave scattering model is presented to aid the understanding of multiple scattering. Advantages of this model include accessibility of the wave field within the scattering medium, tunable scattering strength, availability of phase and amplitude information, and the relative longevity of surface waves. Accompanied by a state-of-the-art non-contacting data acquisition scheme, this system proved ideal for unveiling the effects of multiple scattering.

When a pulse is launched in a strongly scattering medium, it travels ballistically at first, but turns diffusive as multiply scattered waves interfere with the incident pulse. Radiative transfer has proven to describe both the transmission of the coherent pulse through the scattering media, as well as the diffusive energy that is dominant at later times. Advances in the the understanding of radiative transfer theory both experimentally, as well as theoretically, make it possible to quantify bulk properties of this scattering medium, including independent estimates of scattering attenuation and intrinsic absorption and energy velocity. Preliminary studies in full-waveform sonic logging show potential of such an analysis in terms of radiative transfer.

Small amplitude variations caused by scattering were also observed and confirmed by spectral-element numerical simulations. These included body-wave precursors to the dominant surface waves and flexural resonance of the scatterers.

As an application of this work, a model is presented that proved to be a successful test in applying a wave-equation based method to image, predict and subtract scattered waves, when the interest is in other events than the scattered field.

I'm pickin' up good vibrations
B. Wilson and M. Love
SMiLE, 1966

Table of Contents

Acknowledgments	viii
Chapter 1 Introduction	1
1.0.1 Matter of Scales	2
1.1 Wave propagation in (grooved) aluminum	3
1.2 Multiple scattering at the macroscopic scale	3
1.3 Strong scattering at the mesoscopic scale	4
1.4 Multiple scattering at the microscopic scale	4
1.5 Near surface statics estimation	4
Chapter 2 Surface waves in theory and experiment	5
2.1 Summary	5
2.2 Introduction	5
2.3 Rayleigh waves in an elastic and isotropic half-space	5
2.4 Source and receiver in the laboratory	7
2.4.1 The Rayleigh wave source	7
2.4.2 The laser vibrometer detector	8
2.5 Surface wave propagation in homogeneous aluminum	8
2.6 When a surface wave meets a groove	9
2.6.1 Measurements on the top	10
2.6.2 Measurements on the side	12
Chapter 3 Multiple scattering at the macroscopic scale	13
3.1 Summary	13
3.2 Introduction	13
3.3 The grooved aluminum model	13
3.4 A tunable multiple-scattering system	15
3.4.1 Group velocity vs. scattering strength	17
3.5 Strongest scattering	19
3.6 Ensemble measurements	20
3.6.1 Discussion	23
Chapter 4 Multiple scattering at the mesoscopic scale	25
4.1 Summary	25

4.2	Introduction	25
4.3	The radiative transfer equation	26
4.4	Radiative transfer in 1D	28
4.4.1	The Green's function of the total intensity	30
4.5	Radiative transfer on the grooved face	32
4.5.1	Fitting the data with radiative transfer	34
4.6	Conclusions	38
Chapter 5 Multiple scattering at the microscopic scale		39
5.1	Summary	39
5.2	Introduction	39
5.3	Numerical modeling	40
5.4	Scanning the grooves	40
5.5	Comparing data and simulations	41
5.6	Precursors	44
5.7	Conclusions	47
Chapter 6 Measuring, imaging and suppressing scattered surface waves		49
6.1	Summary	49
6.2	Introduction	49
6.3	Scattered noise model	50
6.4	Inverse scattering	50
6.5	Experiment 1: a surface wave test	51
6.5.1	Results	52
6.6	Experiment 2: a transmission model	56
6.6.1	Results	56
6.7	Conclusions	59
Chapter 7 Concluding remarks		61
References		63
Appendix A The angle-beam transducer source		69
A.1	The source on homogeneous aluminum	69
A.1.1	The vertical component of the source	70
A.1.2	The out-of-plane component of the source	70
A.1.3	The in-plane horizontal component of the source	72
A.2	The source on the grooves	72

Appendix B Insights in the radiative transfer equation	75
B.1 The coherent intensity and the O’Doherty-Anstey formula	75
B.2 The scattering cross-section in the limit of weak scattering	78
B.3 The Green’s function for the directional intensity	79
B.4 The diffusion approximation in infinite 1D media	81
B.5 The diffusion approximation in finite 1D media	83
B.6 Green’s function for diffusion in an infinite 1D medium	85
Appendix C Wave speeds in scattering media	87
C.1 Group velocity	87
C.2 Coherent velocity	88
C.3 Observations	88
C.4 Phase velocity of the ensemble-averaged trace	90
C.5 Conclusions	90
Appendix D scattering attenuation and absorption in sonic logging	91
D.1 Observations	91
D.2 Radiative transfer	91
D.3 Fitting the data	94
D.3.1 Relating to Q	95
D.4 Discussion	96
D.5 Conclusions	96
Appendix E The angle-beam transducer source	97

Acknowledgments

My gratitude goes to Dr. John A. Scales, who took it upon himself to show me how interesting, fun and rewarding research can be. I am grateful beyond words for this life-changing experience. In general, I thank everybody in the Physical Acoustics Lab for their input, not only the caffeine input, or academically, but also for dragging me along on long bike rides, swimming, soccer or other physical activity. It kept me (relatively) sane.

The Center for Wave Phenomena and its sponsors supported me in every possible way, not in the least financially. In particular, I thank Dr. Ken Larner for his suggestions, support and meticulous editing of papers that form the foundation of this thesis. I extend my thanks to all the students in CWP for their friendship and encouragements. In particular, I thank Matt Haney for discussions on radiative transfer theory and his insights in connecting it to the O'Doherty-Anstey formula.

Further, I thank my committee members for their interest, discussion and suggestions. Especially Dr. Roel Snieder and Dr. Mike Batzle contributed to the process of my research on a daily basis.

Large contributions to the content of the research were made by Dr. Dimitri Komatitsch and Dr. Jeroen Tromp, with their expertise in numerical simulations. The spectral-element simulations were obtained with their Fortran code. While Xander Campman and Dr. Gérard Herman deserve all credit for the theory and data processing in the near-surface scattering application.

I thank Dr. Bill Navidi and Dr. Luis Tenorio for our cooperation in inversion research, work that served as a comprehensive exam, was published, but not included in this thesis. I also acknowledge the valuable support of Barbara McLenon, Michelle Szobody, Lela Weber and Sara Summers, because we all know they run the show.

Last, but not least, I owe it all to Mila, my family and friends who all put up with me during this long strange trip, and whose support I could not have done without.

Chapter 1

Introduction

In geophysics many studies have been devoted to the topic of scattering from inhomogeneities in the Earth. Of course, we heavily rely on impedance contrasts in the Earth to reflect seismic energy back to the surface, but heterogeneity on a scale smaller than the dominant wavelength is known to influence the characteristics of the seismic signal. For instance, O'Doherty & Anstey (1971) show that reflections within thin layers alter the frequency content of the transmitted pulse, while Backus (1962) found that thin layering, or any preferred orientation of scatterers, makes the seismic velocities angle-dependent (i.e., anisotropic). In Kennett (1984), scattering from heterogeneity in the Earth's crust is shown to transfer energy from the vertical component to the horizontal components. Could this be an early report on a now well-known characteristic of multiple scattering called equipartition (Hennino *et al.*, 2001)? In addition, the scattering of energy due to inhomogeneities in the subsurface is known to attenuate the coherent signal (often referred to as the *first arrival* or *ballistic peak*). This mechanism for attenuation is coupled to intrinsic absorption. Attempts to decouple these for earthquake measurements by Wu (1985), Wu & Aki (1985) and Wu & Aki (1988) were noble and maybe ahead of their time, but hindered by limited data, both in bandwidth, as well as coverage.

This thesis is a study of multiple scattering of surface waves. While multiple scattering of elastic waves in the Earth is a growing topic of research (e.g., Margerin *et al.*, 1999; Hennino *et al.*, 2001; Wegler & Lühr, 2001; Campillo & Paul, 2003), much of its characteristics are still ill defined. The goal is to show that understanding multiply scattered energy can aid our understanding of the disordered systems like the Earth. In practice, however, exploiting multiply scattered waves to make inferences about a medium can be far more complicated than using single-scattering theory such as the Born approximation. In geophysics, nearly all data processing algorithms are based on single scattering theory (Aki & Richards, 1980), but a highly heterogeneous near-surface (Campman *et al.*, 2003), crust (Campillo *et al.*, 1999), and the boundary between core and mantle (Earle & Shearer, 1997; Margerin *et al.*, 1999) provide coherent and diffuse signal. In contrast, human tissue is such a strong scatterer of light that only diffuse (i.e. multiply scattered) light can be measured (Boas *et al.*, 1995).

A solid block of aluminum contains a number of surface wave models. Each face of the block represents a model with a certain level of complexity in surface wave propagation. In a way, this block is a mini-laboratory for the study of surface waves. Overall, each face of the block is large compared to the dominant wavelength, while surface scatterers are smaller than a wavelength. The smooth face of the block is used to determine the material and

source properties. One side of the block with a single groove is used to study the reflection, transmission and diffraction from such a scatterer, before we tackle the problem of surface wave propagation on a face with a multitude of such grooves. This model is a surface-wave equivalent of studies of seismic body waves in finely-layered structures that show multiple scattering by layers much smaller than the dominant wavelength determine the amplitude and the spectrum of the wavelet (O’Doherty & Anstey, 1971; Asch *et al.*, 1991) and cause the effective medium to be anisotropic (Backus, 1962). The final model in this mini-laboratory is a face of the aluminum block with cylindrical holes to test near-surface scattering in higher dimensions.

The reasons for studying surface waves are plentiful. First, surface waves travel – as their name suggests – along the surface of a solid. This makes them available to measure as they propagate, as opposed to body waves that typically can only be detected in transmission or reflection. Secondly, to make surface waves scatter, holes or grooves at the surface are easy to construct and describe. Tertiary, measurements of surface waves consist of phase and amplitude information, which is a crucial advantage over optic studies in multiple scattering where one typically only has measurements of the light intensity. Finally, surface waves decay less rapidly than body waves, because their energy spreads over only two dimensions as they propagate along a surface, while body waves spread spherically. This makes surface waves tractable for relatively large times and distances.

Especially the fields of optics and condensed matter have seen a growing interest in using effective medium theories such as radiative transfer to model the transport of energy in random media (Lemieux *et al.*, 1998). It is in these cases of strong scattering where phases become randomized, that the single scattering model loses its relevance. Radiative transfer models describe the coherent signal at early times and the diffuse waves at later times, providing information about the mean free scattering and absorption lengths as well as the diffusion constant. Beautiful examples of the transition from ballistic to diffuse propagation are presented in the propagation of bulk phonons at low temperature (Narayanamurti *et al.*, 1978), while time-resolved images of this transition in random media such as rocks have been presented in Scales & Malcolm (2003).

1.0.1 Matter of Scales

The chapters are divided by the level of detail describing the model and the multiple scattering phenomena. The coarsest level is called the *macroscopic* regime. It describes the model in terms of bulk properties, like attenuation and scattering strengths, group and phase velocity. At this scale, diffusion of energy is an accurate description of the energy in a strong scattering model beyond the scattering mean free path. Details about the multiple scattering that are at the *microscopic* level show the interaction between a single scatterer and the surface waves, i.e. on a scale much smaller than the scattering mean free path. This regime is governed by the wave equation, describing reflection, transmission and diffraction from a single groove and flexural resonance of scatterers.

In between these regimes is the *mesoscopic* regime. In multiple scattering of waves, this regime hinges on the scattering mean free path. While the macroscopic description of

the model is on length scales beyond a mean free path, and the microscopic scale is much smaller than that, the mesoscopic regime covers the length scale around one mean free path. Energy propagation in this regime is described by the theory of radiative transfer of energy.

1.1 Wave propagation in (grooved) aluminum

Chapter 2 concerns the theory of Rayleigh waves in a homogeneous elastic half-space and experiments in a (finite) aluminum block with and without a single groove. Both the end of the block and the groove diffract surface waves to body waves, but the finite depth of the groove makes reflection and transmission of the Rayleigh wave frequency dependent. In addition, the non-contacting data acquisition is introduced. Much experimental surface wave research is done in non-destructive testing, where one looks for small cracks in materials (see Hess, 2002, for an overview), but also in geophysics where surface waves are used in tomographic inversion for the structure of the Earth (Dahlen & Tromp, 1998), the influence of topography on seismic waves is tested (e.g., Komatitsch *et al.*, 1999) and dispersion curves of ground-roll are used to invert for layered models in near-surface geophysics (e.g., Xia *et al.*, 1999).

1.2 Multiple scattering at the macroscopic scale

To understand the different regimes of multiple scattering, describing the propagation of energy and their transitions, it is extremely useful to have a medium in which the scattering properties can be easily adjusted. For example, with phonon scattering one can control the mean free path via the temperature (Wolfe, 1998). If the mean free path is greater or equal to the size of the sample, then the phonons propagate ballistically. The more scattering between source and detector, the more diffusive the propagation. Chapter 3, based on Scales & van Wijk (1999, 2001), introduces such a surface model in our mini-laboratory. Here we use a face of the block with many grooves per wavelength. Waves propagating parallel to the grooves propagate nearly attenuation and dispersion free, but waves propagating normal to the grooves are dispersed and exponentially attenuated with distance as waves bounce between the grooves. This means that energy is transferred from the direct pulse to later times. This tail of energy is called the multiple-scattering coda. We measure this attenuation length and show that there is, in addition, a scattering induced anisotropy in the group and phase velocity.

By varying the source-receiver orientation with respect to the grooves and the distance between source and receiver, we are able to map out the transition from ballistic to diffusive energy propagation and measure the angle-dependent macroscopic properties of the medium, such as the group velocity, and the scattering mean free path. Finally, the observations around a mean free path are fit in the macroscopic description of diffusion.

1.3 Strong scattering at the mesoscopic scale

Chapter 4 is based on van Wijk *et al.* (2003b) and Haney *et al.* (2003), where radiative transfer theory describes data around a mean free path. It shows how this model describes both the coherent and the incoherent signal, while in Appendix B.1 the connection is made between the coherent energy and classic results in wave propagation in a thinly layered Earth (e.g., O'Doherty & Anstey, 1971; Banik *et al.*, 1985; Shapiro & Zien, 1993). Appendix B.4 shows how the incoherent signal signifies diffusive propagation of energy at late times. This radiative transfer model is thus a description of energy propagation in the *mesoscopic* regime (van Rossum & Nieuwenhuizen, 1999). The main practical advantage of the analysis of coherent *and* incoherent signal is the opportunity to separate scattering attenuation from intrinsic absorption. A feasibility study of determining intrinsic attenuation (also known as the Q-factor in geophysics), separately, is outlined in Appendix D.

1.4 Multiple scattering at the microscopic scale

Chapters 3 and 4 describe the model in terms of bulk properties, ranging from the diffusion constant derived from late times, to average scattering attenuation from the entire trace of observations. However, Chapter 5 concerns the small-scale features that are caused by scattering. A numerical spectral-element code – that proved its strength in global seismology (e.g., Komatitsch & Vilotte, 1998; Komatitsch & Tromp, 1999; Komatitsch *et al.*, 2002; Komatitsch & Tromp, 2002a,b) – is used to confirm these features that are often not much larger than the background noise level. To understand the physics of these phenomena, it is necessary to consider the governing wave equation with proper boundary conditions. In other words, this Chapter – based on van Wijk *et al.* (2003a) – analyzes scattering at the *microscopic* scale.

1.5 Near surface statics estimation

Current methodology in land exploration geophysics to correct for topographic or near-surface material property variations often rely on static time shifts, based on strong assumptions about wave propagation in the near surface. Chapter 6 – based on Campman *et al.* (2003) – introduces a wave-equation based method to apply static corrections caused by near-surface scattering. These corrections are true to the physics in the near-surface and thus include amplitude corrections. All theory and processing in this Chapter originate from Delft University of Technology, while the Physical Acoustics Laboratory provided the models and data acquisition capabilities to test the theory.

Chapter 2

Surface waves in theory and experiment

2.1 Summary

An aluminum block serves as a mini-laboratory for surface wave studies. It is large compared to the dominant wavelength and the aluminum behaves nominally elastic for our purposes. Grooves, which are small compared to the source wavelength, reflect, transmit and even convert the incoming surface wave energy to body waves. However, before we look at complicated interference of surface waves scattered on the face with a multitude of grooves, let us examine the theory of Rayleigh waves, their characteristics on a smooth face of the aluminum laboratory, and finally, on the face with a single groove.

2.2 Introduction

Quantifying the results of surface-wave scattering from lateral variations is of direct interest in geophysics. Scattering caused by topographic variations introduces dispersion of the early arriving energy, which competes with dispersion related to horizontally layered structures. In addition, in global seismology, surface topography or sedimentary basins can trap seismic energy (e.g., Komatitsch *et al.*, 1999), posing seismic hazard, while in exploration geophysics topography needs to be accounted for in terms of static corrections (e.g., Campman *et al.*, 2003).

The aluminum surface wave laboratory is 28 cm × 23 cm × 21.5 cm. A transducer mounted on the surface of an aluminum block excites surface waves. For a detailed analysis of the source characteristics, I refer you to Appendix A. The scattered wave field is recorded with a laser Doppler vibrometer. This entire setup is positioned on a vibration isolation table. This type of non-contacting data acquisition is used on a regular basis in non-destructive testing (see Hess, 2002, for an overview of the literature).

2.3 Rayleigh waves in an elastic and isotropic half-space

Navier's equation, the homogeneous equation of motion in a homogeneous elastic half-space, follows from a balance of forces (e.g., Aki & Richards, 1980):

$$(\lambda + \mu) \nabla (\nabla \cdot \mathbf{u}) + \mu \nabla^2 \mathbf{u} = \rho \ddot{\mathbf{u}}, \quad (2.1)$$

where the displacement \mathbf{u} is a function of space (\mathbf{x}) and time (t), ρ is the density, the partial derivatives with respect to space are $\nabla = (\partial_x, \partial_y, \partial_z)$ and (λ, μ) are the Lamé coefficients. The dots over the displacement vector on the right hand side denote a double partial derivative with time. Since \mathbf{u} is a vector field, we can apply Helmholtz Theorem to represent \mathbf{u} in terms of two potentials:

$$\mathbf{u} = \nabla\phi + \nabla \times \boldsymbol{\psi}, \quad (2.2)$$

where $\nabla \cdot \boldsymbol{\psi} = 0$. In addition, the curl of the divergence of any vector is zero, so that

$$\nabla \cdot \mathbf{u} = \nabla^2\phi \quad \text{and} \quad \nabla \times \mathbf{u} = -\nabla^2\boldsymbol{\psi}. \quad (2.3)$$

Taking the divergence of equation (2.1), we find that the scalar potential satisfies the scalar wave equation for compressional waves (P-waves):

$$\frac{\partial^2\phi}{\partial t^2} = \left(\frac{\lambda + 2\mu}{\rho} \right) \nabla^2\phi, \quad (2.4)$$

where the P-wave velocity $v_p = \sqrt{\frac{\lambda+2\mu}{\rho}}$. The curl of equation (2.1) leads to the vector potential satisfying the vector wave equation for shear waves (S-waves):

$$\frac{\partial^2\boldsymbol{\psi}}{\partial t^2} = \left(\frac{\mu}{\rho} \right) \nabla^2\boldsymbol{\psi}, \quad (2.5)$$

where the S-wave velocity $v_s = \sqrt{\frac{\mu}{\rho}}$. To simplify the notation, let us assume we are looking for a plane wave solution (ϕ and $\boldsymbol{\psi} \propto \exp(i\omega t)$) in 2 dimensions (2D). In this case, equations (2.4) and (2.5) simplify to

$$\frac{\partial^2\phi}{\partial x^2} + \frac{\partial^2\phi}{\partial z^2} + k_p\phi = 0 \quad \text{and} \quad \frac{\partial^2\boldsymbol{\psi}}{\partial x^2} + \frac{\partial^2\boldsymbol{\psi}}{\partial z^2} + k_s\boldsymbol{\psi} = 0, \quad (2.6)$$

where k_p and k_s are the compressional and shear wave numbers. If we consider solutions of harmonic waves propagating in the x -direction, the solutions are of the form

$$\phi = F(z) \exp(i(kx - \omega t)) \quad \text{and} \quad \boldsymbol{\psi} = G(z) \exp(i(kx - \omega t)). \quad (2.7)$$

Inserting these solutions in equation (2.6) gives us

$$\frac{d^2F(z)}{dz^2} - (k^2 - k_p^2) F(z) = 0 \quad \text{and} \quad \frac{d^2G(z)}{dz^2} - (k^2 - k_s^2) G(z) = 0, \quad (2.8)$$

with solutions of the form $\exp(\pm\sqrt{(k^2 - k_{p,s})}z)$. We will show later that $k > k_p > k_s$, so physical solutions whose amplitude decays with depth are of the form:

$$\phi = A \exp(-qz) \exp(i(kx - \omega t)) \quad \text{and} \quad \boldsymbol{\psi} = B \exp(-sz) \exp(i(kx - \omega t)), \quad (2.9)$$

where $q^2 = k^2 - k_p^2$, $s^2 = k^2 - k_s^2$ and (A, B) are arbitrary constants. With the conditions that at the boundary of the elastic half-space the stresses are zero: σ_{zz} and $\sigma_{xz} = 0$, we can write B in terms of A , and find the characteristic relation between the k, s and q to be

$$4k^2qs - (k^2 + s^2)^2 = 0. \quad (2.10)$$

In terms of velocities, this is

$$\left(2 - \frac{c^2}{v_s^2}\right)^2 = 4\sqrt{1 - \frac{c^2}{v_p^2}}\sqrt{1 - \frac{c^2}{v_s^2}}, \quad (2.11)$$

where $c = \omega/k$. This equation is known as the Rayleigh equation, named after J. W. Strutt, Lord Rayleigh, who first published this in 1885 (Strutt, 1885). Mathematically, this equation has six roots for c , but as the Poisson's ratio lies between 0 and 0.5, and we know that the surface wave has to decay with depth, each elastic isotropic medium has one Rayleigh wave with a velocity c_R that ranges between 0.87 to 0.96 times the shear wave velocity, depending on the Poisson's ratio of the medium. Once c_R is known, we can determine individually the inhomogeneous longitudinal and shear wave components from equation (2.9) that are in a Rayleigh wave:

$$\phi = -A \exp(i(kx - \omega t) - qz) \quad \text{and} \quad \psi = iA \frac{2kq}{k^2 + s^2} \exp(i(kx - \omega t) - sz). \quad (2.12)$$

If we know v_p and v_s , the variables s, q are now known and A is a scaling term. From these equations one can see that the shear component is 90 degrees out of phase with the compressional component, due to the factor i . This causes the famous elliptical polarization of the Rayleigh wave. Worth pointing out is that even though the assumed model here is 2D, the out-of-plane shear-component of the vector potential turns out to be zero in a 3D analysis. Finally, equation (2.12) shows that the polarizations decay exponentially with depth, governed by q and s , respectively. Because s and q are proportional to frequency, low frequency Rayleigh-wave components sample the medium to a greater depth than high frequency components.

2.4 Source and receiver in the laboratory

This Section discusses in general terms the excitation and detection of Rayleigh waves in aluminum in the laboratory, but a much more detailed analysis of the source properties is laid out in Appendix A.

2.4.1 The Rayleigh wave source

In the laboratory, waves are excited with a piezo-electric crystal that has the ability to convert a voltage to a mechanical force. This crystal is mounted on a Lucite wedge and this wedge is mounted on the aluminum model. The angle of the wedge is such, that the horizontal component of the P-wave speed in Lucite matches the Rayleigh wave

speed in aluminum. This angle is generally known as the critical angle. The P-wave in Lucite propagates at 2681 m/s. Information about the experimental and analytically determined Rayleigh wave speed in the previous section, makes that the critical angle $\alpha = \arcsin(2681/2870) = 69$ degrees. This is close to the 68 degrees supplied by the Panametrics transducer for generic aluminum.

2.4.2 The laser vibrometer detector

The wave field is detected by a scanning laser interferometer that measures absolute particle velocity on the surface of the sample via the Doppler shift. The output of the vibrometer-head is a beam of diameter less than 1 mm and a wavelength of 633 nm (red). Once the beam reflects off a moving target, its frequency is Doppler shifted. The beat-frequency of the output plus the reflected signal is decoded in the hardware to give an absolute measurement of particle velocity, without contacting the medium. In contrast, contacting transducers are part of the model and can act as scatterers. In addition, contacting transducers of the size of the vibrometer beam are prone to ring: once excited, they *echo* on, due to their light weight. This limitation is tolerable for first arrival measurements, but pose a serious problem in multiple-scattering research.

The signal of the vibrometer is amplified with a low-noise preamplifier (SR 560 with 12 db/octave 10 kHz high-pass filter) and digitized at 14-bit resolution using a Gage digital oscilloscope card, attached to a PC. However, to ensure high signal-to-noise, reflective tape is applied to the model for a strong reflectivity of the interferometer beam. While stacking (averaging) of multiple shots improves data quality, experience tells us that higher levels of noise are mostly caused by a decrease in reflection strength of the interferometer beam. In practice, this often means that there is either an air-bubble between tape and the model, or the reflection strength of the tape is diminished by dirt.

The scanning head is programmed to move the beam after each measurement, so that we can record dense arrays of data, automatically. This stands in sharp contrast with time-consuming contacting transducer measurements, where individual receivers have to be moved manually. The possibility to record at many locations per wavelength allowing a dynamic data analysis (movies) and filtering techniques in space-domain, as are currently being investigated in exploration geophysics (Baeten *et al.*, 2000).

The flexibility of a small, non-contacting and programmable receiver, allows us to measure with relative ease and precision multiply-scattered waves, even between the scatterers.

2.5 Surface wave propagation in homogeneous aluminum

To study multiply scattered waves in grooved aluminum, we must first address wave propagation in the background medium. Figure 2.1 is the top-view of the experimental configuration (left) and the wave fields at each detector (right). The linear events are the direct wave followed by the reflection off the end of the block. These ray paths are drawn in the left panel. The direct arrival is followed by some weaker events that are caused by ringing of the source (see Appendix A for details). The reflected wave is less energetic than

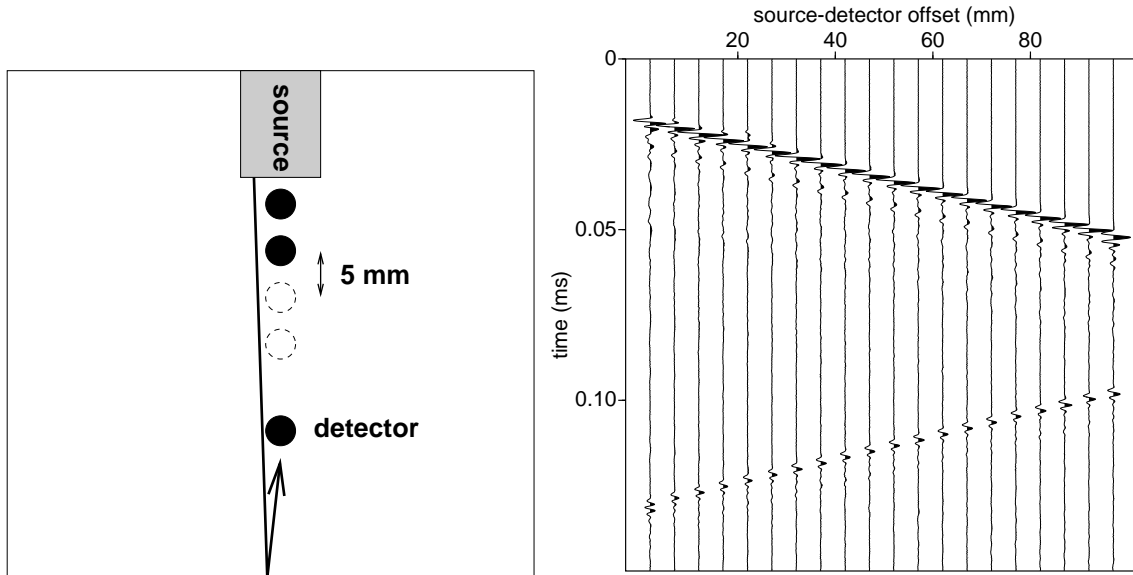


Figure 2.1. Top-view of the experimental configuration (left) on the smooth face of aluminum. The shaded box represents the source and the circles represent 20 equi-spaced detector locations. The wave field for each detector is shown on the right. The spot-size of the interferometer beam has a diameter of 1 mm, the source is 42 mm wide, and the dominant wave-length is on the order of 1 cm.

the direct wave, because energy is diffracted to body waves at the edge of the block. Since the amplitudes of the direct arrival (or of the reflection) vary insignificantly with source-detector distance, we consider the aluminum block to behave elastically and thus neglect intrinsic absorption.

The phase velocity of the Rayleigh wave on the smooth face of aluminum is experimentally determined from the move-out of a particular phase of the wave field, as a function of distance. Figure 2.2 shows the picks of the maximum energy in each trace and the regression through the picks. This measured phase velocity of the Rayleigh wave is $v_R \approx 2870 \pm 5$ m/s. Even though the documented material properties vary from one aluminum to the next (Anderson, 1989), with the knowledge of v_p and v_s from transmission measurements, equation (2.11) predicts the Rayleigh wave speed to be $v_R \approx 2864$ m/s.

2.6 When a surface wave meets a groove

A computer controlled milling machine etched a single 1-mm wide and 2.75-mm deep groove on one face of the aluminum block. When a Rayleigh wave encounters this groove, part of its energy is reflected and part is transmitted. However, just like the edge of the block, the groove diffracts energy to body waves as well. The magnitude of these parts is

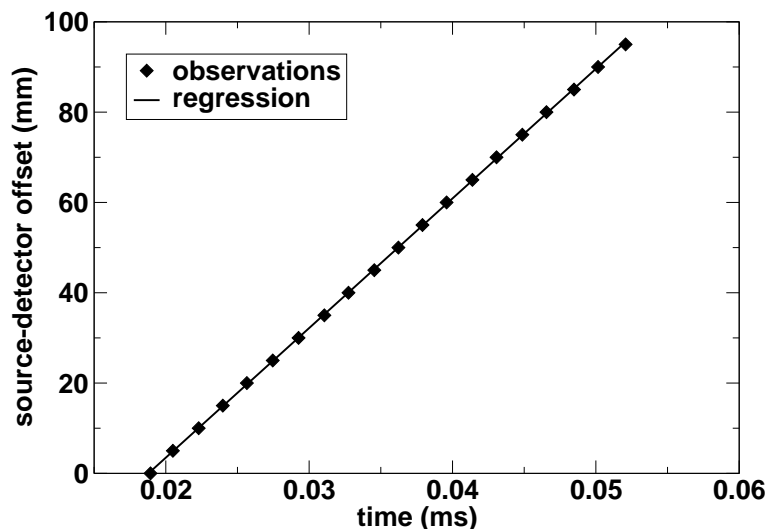


Figure 2.2. Arrival times of the maximum energy as a function of offset on the smooth face of aluminum and their regression. The regression shows that the Rayleigh wave velocity is $v_R \approx 2870 \pm 5$ m/s.

strongly dependent of the frequency content of the Rayleigh wave, but an analytic solution determining the proportions of transmitted, reflected and diffracted energy is unknown for this model. Viktorov (1967) describes the reflected and transmitted waves as a combination of tunneling under the groove, energy following the circumference of the groove, and actual oscillations of the two side-walls of the groove.

2.6.1 Measurements on the top

Figure 2.3 is the top-view of the experimental configuration that measures the reflected and transmitted Rayleigh wave on top of the block. The resulting wave field for one detector between the groove and the source (left) and for one past the groove (right) are depicted in Figure 2.4. Both wave fields show two dominating events. The left panel shows the direct Rayleigh wave followed by a reflection from the groove, while the right panel shows the wave field transmitted past the groove followed by the reflection from the end of the aluminum block. These ray paths are drawn in Figure 2.3. Overall, the amplitude of the transmitted wave is a factor 7 smaller than the incident wave. The reflection from the groove contains the high frequencies present in the source wavelet, because the higher frequencies sample the top-layer of the block and are therefore stronger reflected than lower frequencies. Whereas the lower frequencies dominate the transmitted energy, as that part of the incident energy that tunnels under the groove.

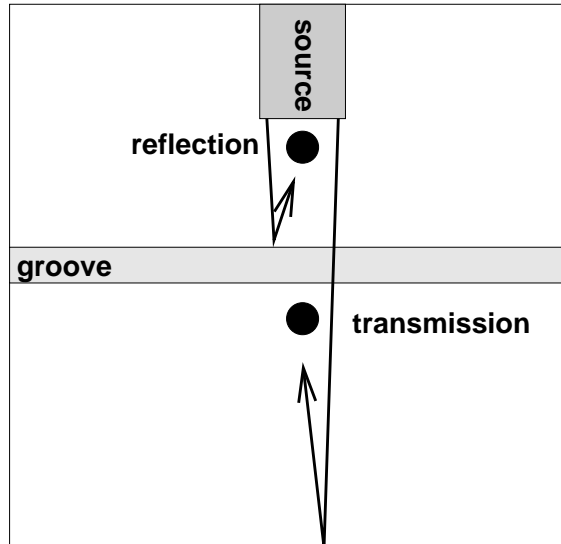


Figure 2.3. Top-view of the experimental configuration. The circles represent detector locations. The spot-size of the interferometer beam has a diameter of 1 mm, the source is 42 mm wide, and the dominant wave-length is on the order of 1 cm. The recorded wave field at these detectors is depicted in Figure 2.4.

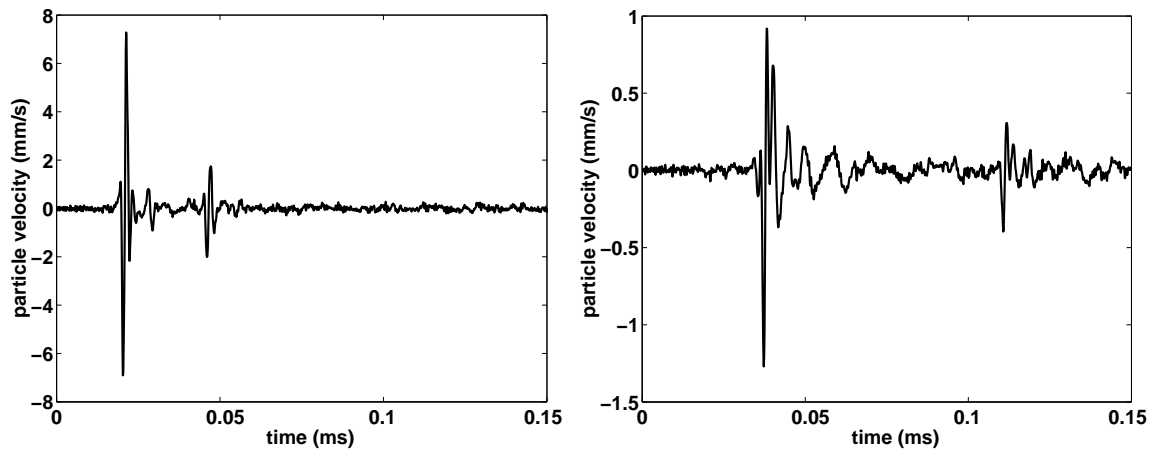


Figure 2.4. Reflection (left) and transmission (right) for a single groove. The primary peaks are the direct arrival. In the left panel, the secondary peak is a reflection from the groove, while in the right panel this secondary peak is the reflection from the end of the block.

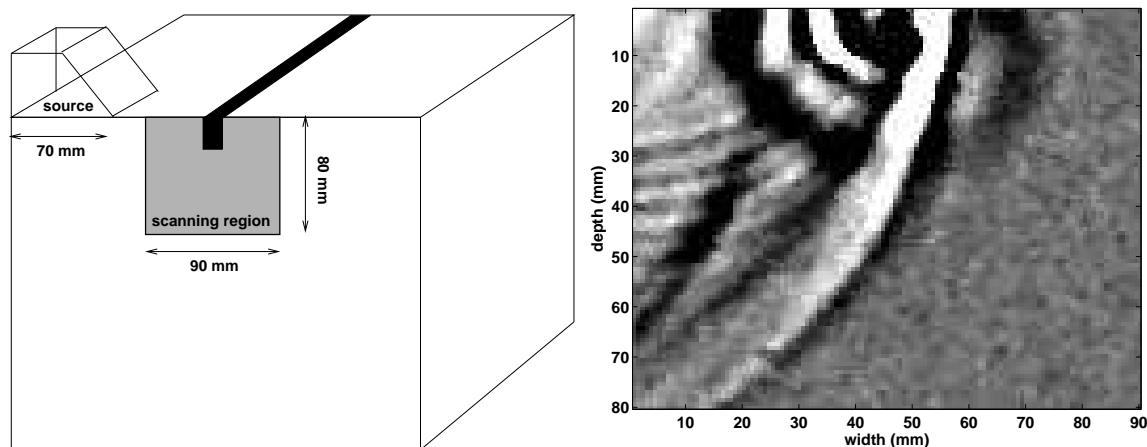


Figure 2.5. Left: experimental configuration, where the source is perpendicular to a single groove on the top of the block, while the detector scans the side. Right: snap-shot of particle motion in the scanned region after the incident field scattered off a single groove. Note that the groove is 1-mm wide, and 2.75-mm deep; a fraction of the dominant wavelength.

2.6.2 Measurements on the side

In an isotropic and elastic half-space, Rayleigh waves only have particle motion in the direction of propagation and in the vertical plane as shown in Section 2.3. However, placing the source on the edge of the aluminum block, breaks the symmetry and excites an out-of-plane component. This component is measured on the side in an area surrounding a single groove (left panel of Figure 2.5). A snap-shot of the wave field (i.e. an image of the wave field at a single point in time) shortly after the incident Rayleigh wave interacted with the groove is shown in the right panel. The almost linear white event is the transmitted field, with the S-wave at greater depth (see Appendix A for details about the source wavelet). The other white event is the reflected Rayleigh wave. In the left side of the right panel one can observe weak body waves excited by the source. The semi-circles centered around the groove are body waves that are diffracted as the Rayleigh wave encounters the groove. This body-wave energy is lost from the surface-wave energy, making the grooved model not truly 1D. In theory, these body waves can return to the surface, after reflecting off the bottom of the block. However, for the time that we record, the body waves do not re-enter the surface model. This is why the body-wave diffractions are treated as a loss term in a 1D surface-wave model.

Chapter 3

Multiple scattering at the macroscopic scale

3.1 Summary

This Chapter describes wave propagation on a face of our aluminum laboratory with many grooves. Waves traveling parallel to the grooves do not encounter the scatterers, but as I rotate the angle between the direction of propagation and the groove orientation, scattering gets stronger, causing attenuation, dispersion and a decrease in seismic velocities. Ensemble measurements of wave propagation perpendicular to the grooves are used to determine the scattering mean free path. Energy propagation at source-detector distances of a mean free path or beyond should – by definition – start to show diffusive behavior. The macroscopic description of diffusion of energy is confirmed by fitting the data to the Green’s function for the 1D diffusion equation.

3.2 Introduction

The influence of multiple scattering in wave propagation measurements can be seen in many ways. There are subtle, long-wavelength effects such as anisotropy (if the scatterers are aligned) and attenuation (as energy is shifted from the ballistic pulse into the multiple-scattering coda) (Groenenboom & Snieder, 1995). These effects are well known in seismology (e.g., Backus, 1962; Aki & Chouet, 1975; O’Doherty & Anstey, 1971) and have been used to interpret effective material properties from macroscopic measurements. However, in most cases the same phenomenon can be looked at from different points of view (such as ballistic propagation, diffusion or radiative transfer) depending, for example, on the wavelength of the probing beam relative to the size of the disorder and on the distance propagated. To understand these different regimes, a surface wave model is presented in which the scattering properties are easily adjusted.

3.3 The grooved aluminum model

On one face of the aluminum block, a computer-controlled milling machine etched a Fibonacci sequence¹ of aligned linear grooves (Figure 3.1). These sequences are frequently

¹From *Liber Abbaci*, 1202 but revised in 1228. meaning The Book of the Abacus (or The Book of Calculating). One of the problems in this book was about reproducing rabbits, which introduced the series 1,1, 2, 3, 5, 8, It was much later (around 1870) that Lucas named this series of numbers after Fibonacci.

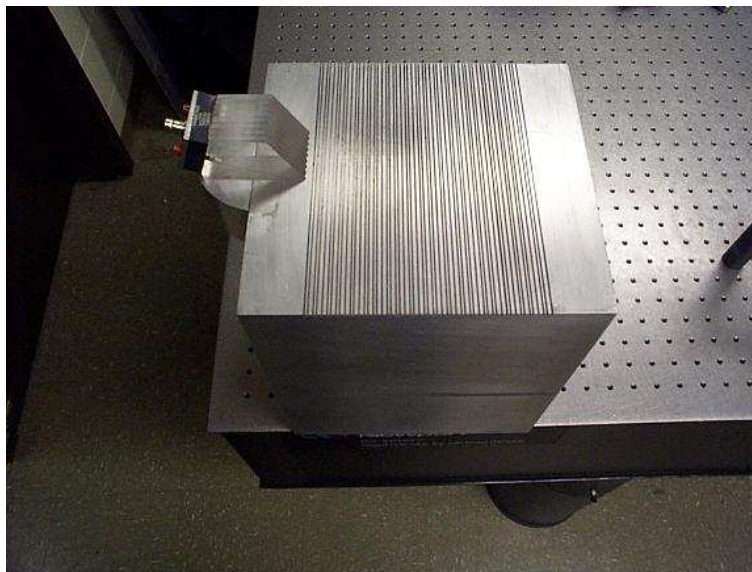


Figure 3.1. The grooved aluminum and the angle-beam transducer are positioned on the optical bench with vibration isolation.

used in studies of disorder since they are quasi-periodic yet exhibit considerable complexity as the order of the sequences increase (e.g., Toet *et al.*, 1991; Carpena *et al.*, 1995) and have even been observed to have localizing behavior (e.g., Gellermann *et al.*, 1994; Dal Negro *et al.*, 2003), meaning that certain wavelengths cannot be transmitted – and thus are localized or trapped (Anderson, 1958)– in such a sequence, due to destructive interference of the multiply scattered waves.

A Fibonacci sequence can be made by concatenating the previous two sequences in the series. Let $S(0) = A$ and $S(1) = B$ be the base elements of the sequence. Then the n -th order sequence is obtained via

$$S(j) = \{S(j-1), S(j-2)\}, \quad j = 2, 3, \dots, n. \quad (3.1)$$

The curly braces denote concatenation (as opposed to addition for the usual Fibonacci numbers). For example, A and B might denote the value of some physical property characterizing each of the base units of the sequence. In the present problem A and B are used to denote the presence or absence of a groove; for example, the sequence ABB is a groove followed by two non-grooves. If the basic unit of spacing (the width of a groove or a non-groove) is h , then ABB denotes a groove of width h followed by a non-groove of width $2h$. Nominally, the grooves are $h = 1$ mm wide and 2.75 mm deep, while the dominant wavelength of the surface waves on the smooth face of aluminum is on the order of 15 mm, so there are many scatterers per wavelength as waves propagate perpendicular to the grooves.

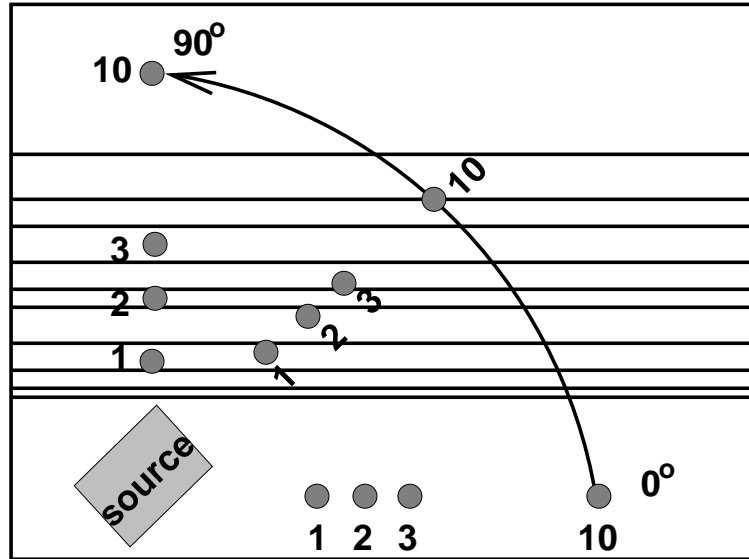


Figure 3.2. Top-view of the experimental configuration that measures the wave field at 10 source-detector offsets for 10 angles between the source-detector line and the grooves, ranging from 0 to 90 degrees.

3.4 A tunable multiple-scattering system

The basic measurement consists of the vertical component of particle velocity measured at 1-cm increments or *offsets*, along a line extending perpendicularly from the transducer front to a maximum offset of 10 cm. Such a measurement is called a *constant-angle section*. The line along which the measurements are made defines an angle relative to the orientation of the grooves. Constant-angle sections range from 0 to 90 degrees, with 10-degree spacing; 0 degrees being parallel to the grooves. Thus there are a total of 100 traces (10 angles and 10 offsets). The experimental configuration is sketched in Figure 3.2.

Figure 3.3 contains the wave fields for propagation parallel to the grooves. It shows that propagation at zero degrees with the grooves is essentially identical to propagation on the smooth surface of aluminum in Figure 2.1; both are nominally attenuation- and dispersion-free. An exception is the last trace, where the detector was positioned on the edge of the surface. There, a complicated super-position of the surface wave and the diffraction at the corner alter the measured wave field. However, as the angle of the propagation increases, scattering becomes significant. Figure 3.4 the source-detector line at 50 degrees with the grooves: an intermediate scattering strength. In this constant-angle section one can see dispersion and attenuation of the early arrivals, and multiple-scattered energy arriving at later times. Figure 3.5 shows the transition from ballistic propagation to strong multiple-scattering as the angle between surface wave propagation and the grooves is increased.

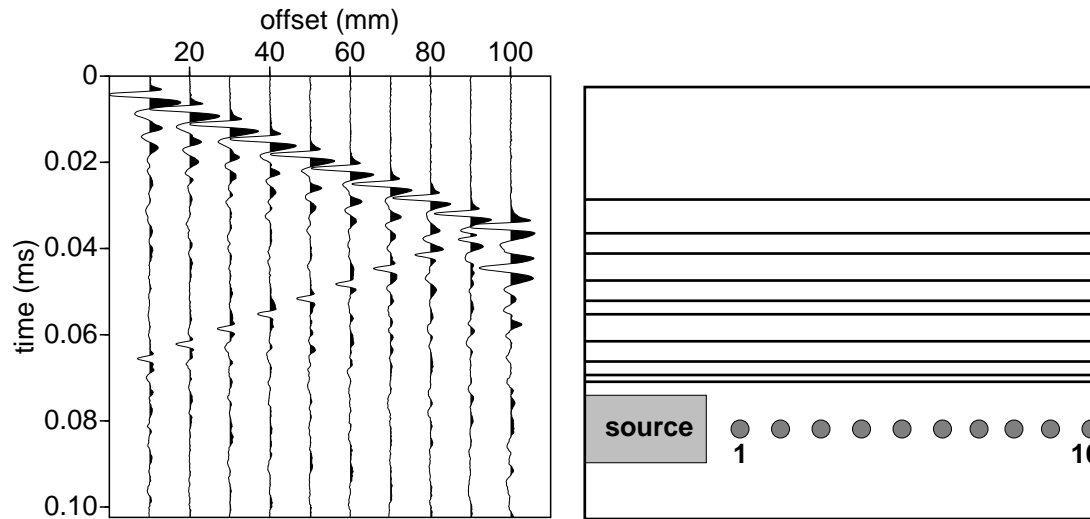


Figure 3.3. Surface wave propagation monitored at increasing source-detector offset, parallel to the grooves. Essentially, the propagation is identical to that on smooth aluminum. The final trace is distorted, being measured too close to the diffracting edge of the block.

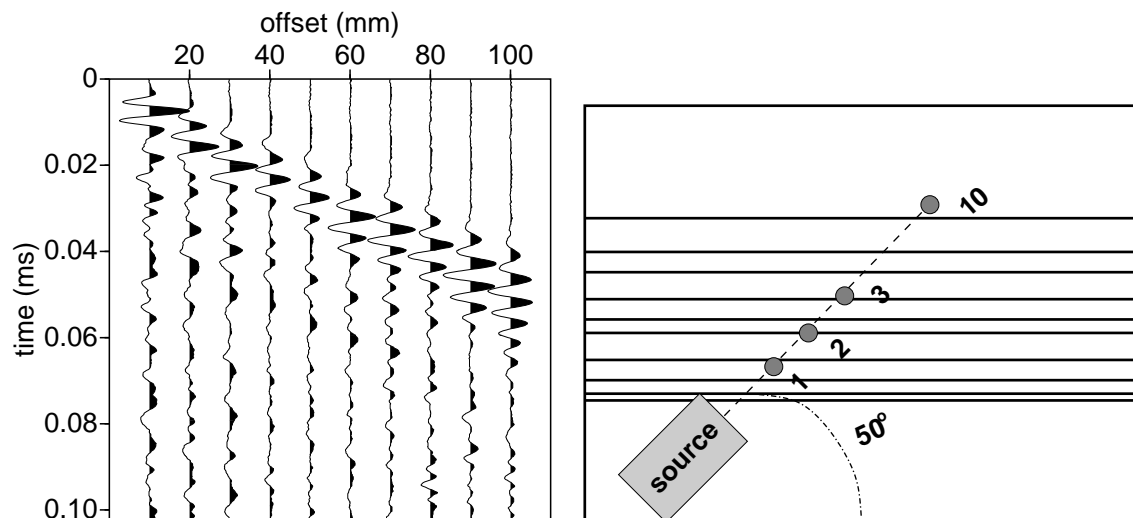


Figure 3.4. A constant-angle section (50°); that is, variable source-receiver distance at a fixed angle relative to the grooves.

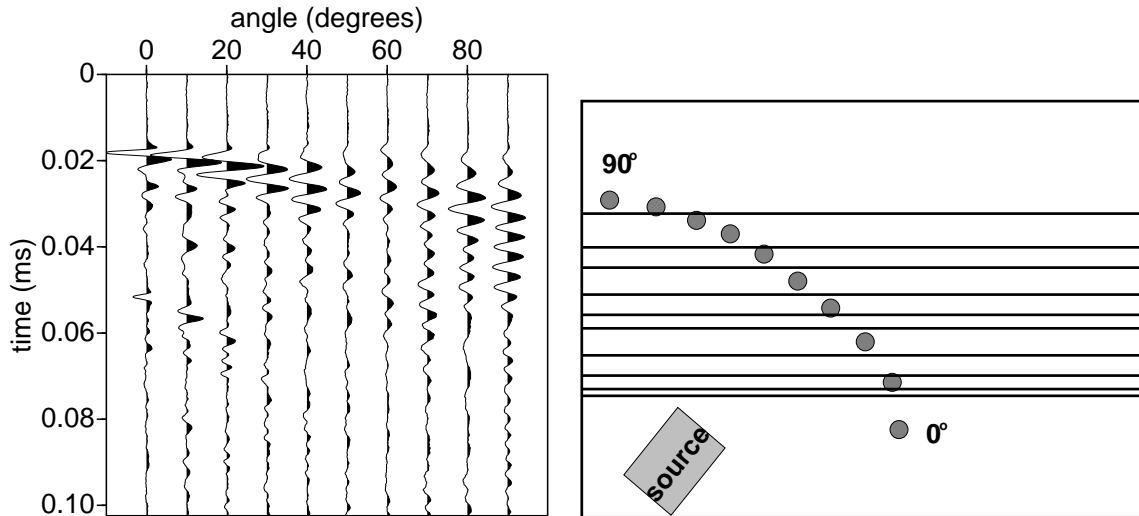


Figure 3.5. A constant-offset section (5 cm); that is, variable angles for a fixed source-receiver distance.

In the absence of scattering, the dominant frequency is that of the source wavelet; around 400 kHz. However, scattering reduces the high frequency power in the data in two ways. First, because the 2.75 mm-deep grooves scatter the shallower traveling high frequencies more effectively, they are poorly transmitted. Second, the interference of multiples in a cyclic system (aluminum/air) is known to reduce the frequency of the transmitted pulse. Basically, the multiples trailing in the forward direction have the same polarity, because they have changed sign twice at a boundary between aluminum and air (e.g., O’Doherty & Anstey, 1971; Mateeva, 2001). This means pulses of the same polarity arrive within a dominant wavelength, broadening the cumulative wavelet.

3.4.1 Group velocity vs. scattering strength

The longer effective path lengths of the multiply-scattered waves result in a significant slowing of the energy propagation. To estimate this group velocity as a function of angle, the data is sorted into constant-angle sections and the energy envelopes of each trace are computed. The peaks of these envelopes were picked automatically and the times taken to be the arrival times of the pulse. This gives an arrival time for each offset, the set of which were fit with a straight line to arrive at the group velocity (Figure 3.6). The error bars are 98% coverage intervals from the regression. Destructive interference or mode-conversion causes intensities from 60-80 degrees to be weaker, making the error bars in the group velocity estimate larger. The group velocity in the strongest scattering case (90 degrees) is discussed in Appendix C.

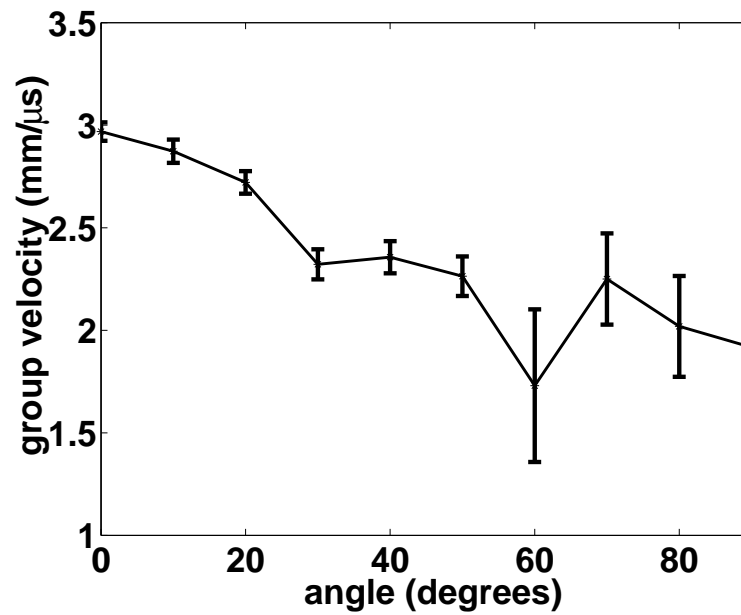


Figure 3.6. Group velocity decreases by 30 percent as the increasing scattering strength shifts energy to the coda. Larger error bars at 60-80 degrees are the result of destructive interference for the wave field at this angle.

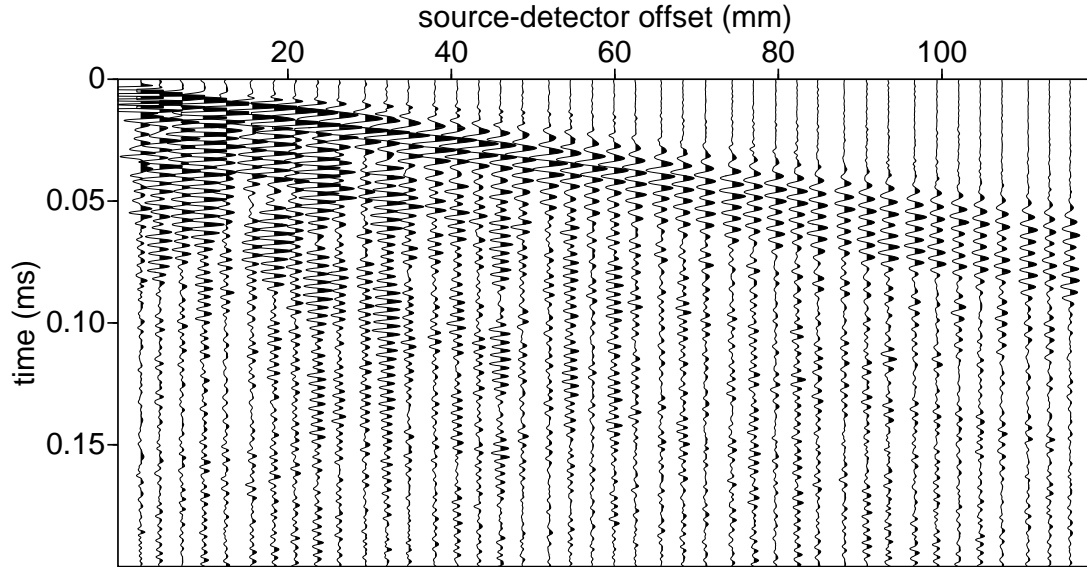


Figure 3.7. The wave field recorded on the grooved aluminum surface on each of the first 42 non-grooves.

3.5 Strongest scattering

Figure 3.7 contains the records of wave propagation normal to the grooves. The source is located before the groove sequence and the detectors are between the first 42 grooves. This area of aluminum is called a non-groove. Signal for the first traces in Figure 3.7 are clipped in amplitude, so that the traces with a larger source-detector separation show ample signal. This illustrates the strong attenuation of the first arrival, caused by scattering from the grooves; not only is energy diffracted to body waves, it is also delayed by bouncing around between grooves. This energy at late times is often called the coda.

The left panel of Figure 3.8 shows the peak amplitude of the first pulse as a function of distance from the source. The decay is well fit by an exponential. The decay length will vary according to the properties and distribution of the scatterers; in this particular case the $1/e$ decay length is about 25 mm. For a quasi-1D system such as this, this decay length can be taken to be the localization length (Scales & van Vleck, 1997). The right panel of Figure 3.8 shows the arrival time of a particular surface wave phase as a function of the source-receiver offset. The slope of the best fitting straight line gives an estimate of the phase velocity. For propagation on the smooth face, or for propagation parallel to the grooves, regression yields a phase velocity of 2870 ± 5 m/s, whereas for propagation normal to the grooves the phase velocity is 2801 ± 14 m/s. Since the depth of the medium is many wavelengths and the medium itself is homogeneous, except for the grooves (which

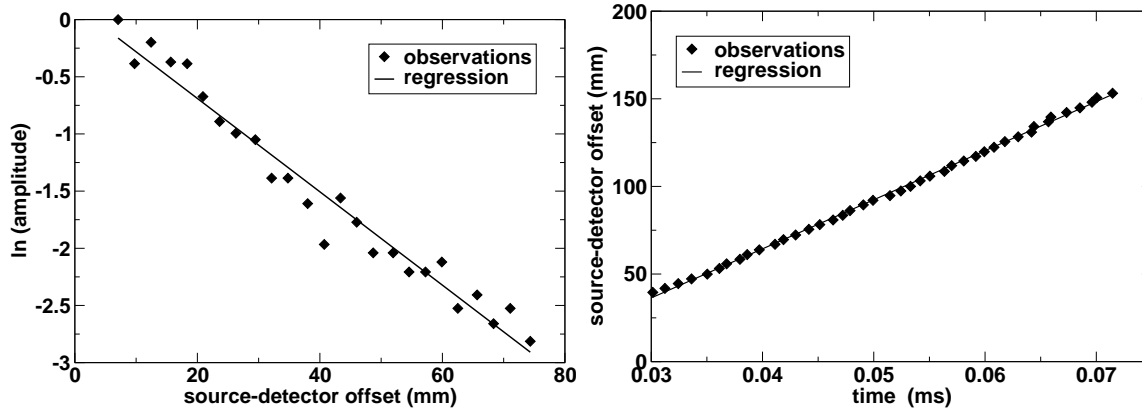


Figure 3.8. Attenuation of the first pulse and the best fitting exponential (left). The $1/e$ attenuation is achieved at 25 mm. A particular phase of the wave field as a function of source-detector offset. The phase velocity normal to the grooves is 2801 ± 14 m/s. This is 2.5 percent less than the phase velocity on the smooth face of aluminum: 2870 ± 5 m/s.

are perturbations of the free surface), this reduction in the phase velocity is due to the interference of the multiply scattered waves. In other words, for propagation normal to the grooves we see a long-wavelength effective anisotropy caused by the multiple scattering. This effect is well-known in seismology where geologic layering gives rise to long-wavelength transverse isotropy (e.g., Backus, 1962).

3.6 Ensemble measurements

Even though this grooved face is not a truly random medium, we can exploit the spatial disorder of the Fibonacci grooves (Carpena *et al.*, 1995) to estimate the scattering mean free path of the medium as well as study the transport of energy. Figure 3.10 shows the wave field at a fixed offset of 5 cm, for 38 different positions in the medium, as sketched in Figure 3.9. The location of the fixed source-detector pair is incremented between shots by 2 mm along the source-detector axis, perpendicular to the grooves. These traces have been corrected for minor positioning errors by aligning the traces via cross-correlation. This was done by cross-correlating each trace with the coherent (average) trace and then using the time associated with the peak of this cross-correlation as a static time shift.

Let $u(r_i, t)$ denote the i -th of 38 realizations of the measured field u (particle velocity). Appealing to ergodicity, we will treat the different traces as 38 realizations of a time-varying random process $u(\mathbf{r}, t)$. Angle brackets $\langle \cdot \rangle$ denote expectation with respect to this random process. The coherent field is then $\langle u \rangle$. The total field can be expressed $u = \langle u \rangle + u_f$, where u_f is the fluctuating part of the field. All intensities are ensemble averaged intensities. The total intensity I_t is the intensity of the total field: $I_t = \langle |u|^2 \rangle$. The coherent intensity is $I_c = |\langle u \rangle|^2$. For a plane wave normally incident in a semi-infinite

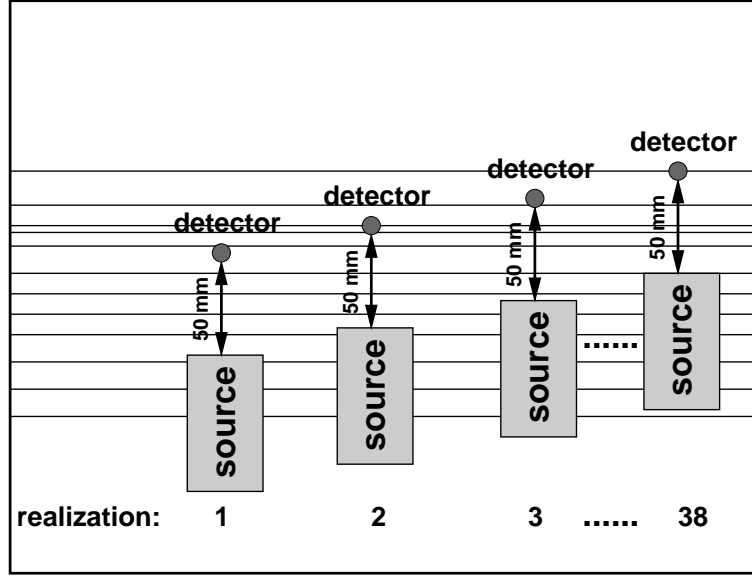


Figure 3.9. Top-view of the experimental configuration to measure the wave field at 38 locations at a fixed source-detector offset of 5 cm on the block.

medium filled with random scatterers, the total and coherent intensities are expected to decay exponentially as (see Ishimaru, 1997), section 14-3): $I_t(x) = I_0 \exp(-x/\ell_a)$ and $I_c(x) = I_0 \exp(-x/\ell_a) \exp(-x/\ell_s)$, where ℓ_a and ℓ_s are the absorption and scattering mean free paths, respectively. Therefore, the ratio of these two intensities decays exponentially, depending only on the scattering mean free path (De Rosny & Roux, 2001):

$$\frac{I_c(x)}{I_t(x)} = \exp(-x/\ell_s) = \exp(-vt/\ell_s) = \exp(-t/\tau_s), \quad (3.2)$$

where v is the group velocity and τ_s is the scattering mean free time.

Numerically, the coherent intensity I_c is the intensity of the average trace, while the total intensity I_t is the average of the intensities of the individual traces. The ratio of I_c to I_t is shown in Figure 3.11. Fitting an exponential to the portion of the curve after the coherent arrival (about $30 \mu\text{s}$), the mean free time $\tau_s = 24 \mu\text{s}$. Since this measurement is for propagation at 90 degrees with respect to the grooves, the group velocity is around $2 \text{ mm}/\mu\text{s}$, which gives a mean free path of just under 5 cm. Thus we are in a regime in which the wavelength is large compared to the size of an individual scatterer, but small compared to the mean free path; while we have measurements with source-detector offsets as large as 2 mean free paths. In this sense one observes here the transition from ballistic to diffusive propagation. With this estimate of the scattering mean free path, the coherent intensity decays exponentially with an absorption length $\ell_a \approx 50 \text{ mm}$. This absorption describes the loss of energy from diffractions off the bottom of the grooves.

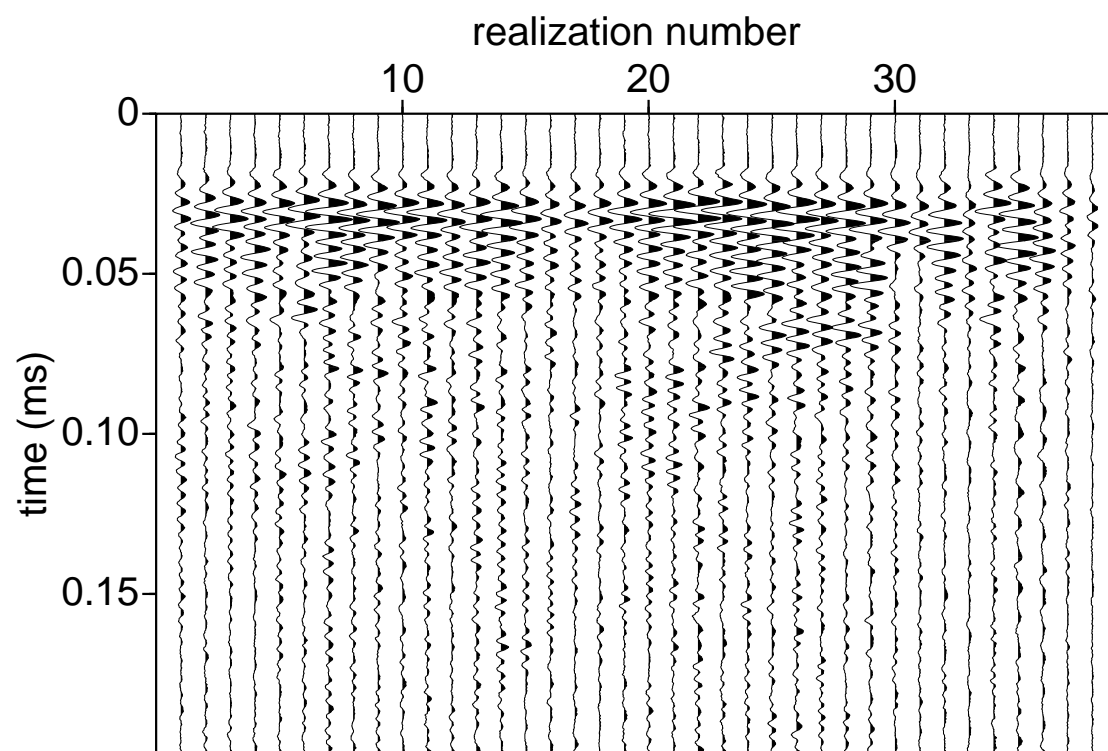


Figure 3.10. 38 records of the wave field at a fixed offset of 5 cm on the block. The source/receiver combination was moved by 2 mm between shots.

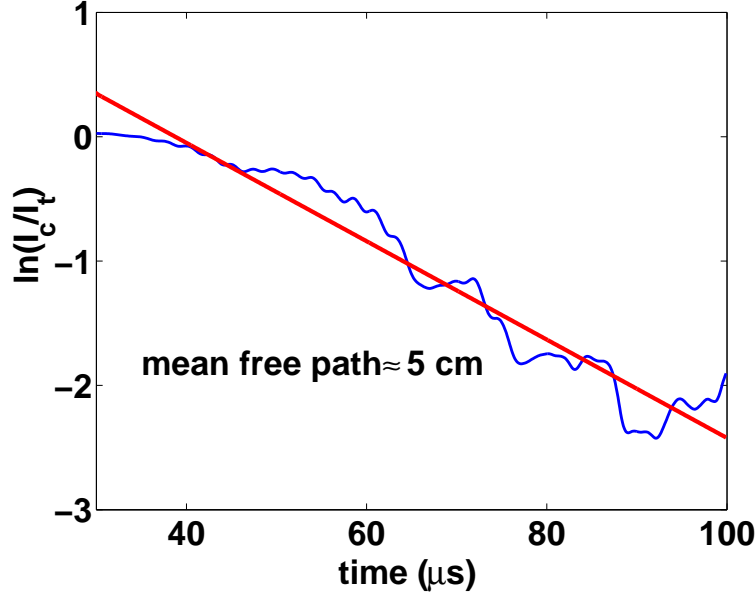


Figure 3.11. Ratio of coherent to total intensities averaged over the ensemble of realizations. The curve decays after the coherent arrival. This decay is fit with an exponential the decay constant of which is the mean free time; in this case, $24 \mu\text{s}$.

To get some idea of whether the total intensity behaves diffusively at 5 cm offset, as is suggested by our estimate of the mean free path, we fit the ensemble-averaged total intensities with an analytic model associated with propagation in a homogeneous diffusive, absorbing medium. We included absorption to account for diffraction losses off the grooves. The Green's function for this model is given by

$$I_t(x, t) = (4\pi Dt)^{-1/2} \exp\left(-\frac{x^2}{4Dt} - D\kappa^2 t\right), \quad (3.3)$$

where $\kappa = 1/\ell_a$ is the absorption coefficient, D is the diffusion constant and x is the propagation distance. This solution is derived in Appendix B.6. A fit to the data is shown in Figure 3.12.

3.6.1 Discussion

This fitting to the diffusion equation alone, cannot determine D , explicitly; the propagation distance is not well-defined since in the real experiment the waves propagate ballistically for some distance, whereas the model is for a homogeneous diffusive medium. However, we can get a rough estimate of the diffusion constant as follows. First $D = v\ell_{tr}/d$ where v is the transport velocity, ℓ_{tr} is the transport mean free path and d the dimension of the

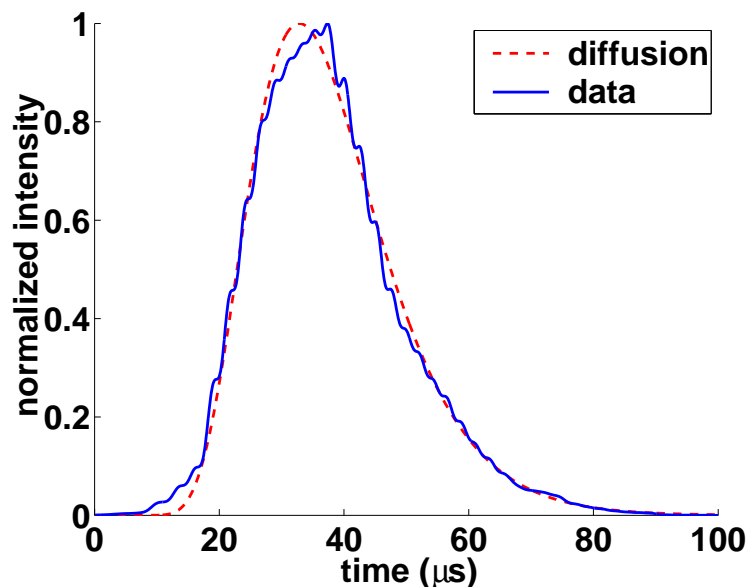


Figure 3.12. Fit of intensity to a model involving propagation in a 1D diffusive, attenuative medium. The attenuation is an approximation to diffraction losses off the bottom of the grooves.

experiment. Our method of measuring the energy envelope yields the group velocity for weak scattering, but for strong scattering the energy propagates according to the transport velocity. So for 90° propagation $v \approx 2 \text{ mm}/\mu\text{s}$. If in the strong scattering regime where the ensemble of wave forms was measured, the transport mean free path is equal to the scattering mean free path, the diffusion constant is $2 * 50 = 100 \text{ mm}^2/\mu\text{s}$ in 1D.

In the literature, energy propagation fits the macroscopic description of the diffusion approximation after several scattering mean free paths. The reason we see a good fit to the diffusion solution at one mean free path is aided by some smoothing of the total intensity. However, The next Chapters extend the ensemble measurements to distance dependence of the average intensity and treat the model in the mesoscopic regime, including an analytic derivation of the governing mathematics. It will show that the estimated scattering mean free path is not an artifact of the source-receiver distance in this particular ensemble measurement and that the exponential decay of the total and coherent intensities are approximations only valid for late time.

Chapter 4

Multiple scattering at the mesoscopic scale

4.1 Summary

Here we show detailed measurements of wave propagation in a 1D strongly scattering medium that fit the theory of radiative transfer for both early times (ballistic propagation) and late times (diffusive propagation). Using the radiative transfer model we are able to estimate the energy velocity and both the scattering and absorption mean free paths.

4.2 Introduction

When waves propagate through a medium they encode information about the properties of that medium. The information from multiply scattered waves has a very different character than that associated with directly propagating or singly-scattering waves. Consider two examples. A normal mode or standing wave can be thought of as the superposition of traveling waves that repeatedly sample a finite medium (by reflection from or propagation around boundaries). Thus small changes in the size or properties of the medium are amplified by each pass of the traveling waves; this amplification leads to the exquisite precision of spectroscopy, allowing one to infer properties that would be completely undetectable with directly propagating waves (Zadler *et al.*, 2003). On the other hand, suppose a wave passes through a cloud of similar scatterers; if some property of the scatterers changes, then this effect is repeatedly imparted on the multiply-scattered wave, making it potentially observable even when the perturbation of a single scatterer is unresolvable (Snieder *et al.*, 2002; Lemieux *et al.*, 1998; Cowan *et al.*, 2002).

Propagation of strongly scattering surface waves is analyzed in this Chapter using model of radiative transfer. Radiative transfer has its origins in the kinetic theory of gases and is sometimes referred to as the Boltzmann transport equation in honor of its earliest proponent. In the earth sciences, it first appeared within the context of light propagation through the atmosphere (Schuster, 1905). Recently, geophysicists have begun to address the applicability of radiative transfer to multiply-scattered seismic waves (e.g., Hennino *et al.*, 2001; Campillo & Paul, 2003; van Wijk *et al.*, 2003b; Wegler & Lühr, 2001; Wu & Aki, 1988).

By squaring a wave field and averaging over many realizations of random disorder, the phase information of the underlying wave field is lost. What remains is the average intensity. Radiative transfer is a phenomenological theory for the spatial and temporal evolution of a wave field's average intensity. The theory's strengths lie in the ability to provide statistical

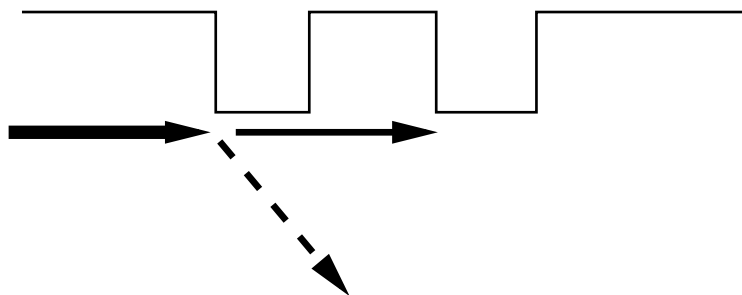


Figure 4.1. Side-view of paths for energy in grooved aluminum. Attenuation of the transmitted surface wave is caused by diffraction of energy to body waves.

information about the structure of a medium at scales less than a wavelength and the decoupling of scattering and absorption effects.

First, the Green's function for an attenuating 1D radiative transfer model is derived.¹ This solution to the radiative transfer equation describes the data with parameters such as scattering strength, attenuation and energy velocity. Even though formally speaking, energy is localized in 1D random media, our data and theory (Sheng, 1995, equation (P6.41)) suggest there is a window where energy behaves diffusively, and the radiative transfer model is valid.

4.3 The radiative transfer equation

The radiative transfer equation can be derived from energy balance considerations (Morse & Feshbach, 1953; Ishimaru, 1997; Turner, 1994). Instead, here I lay out the underlying physical picture of the surface wave scattering model. Consider the incident surface wave encountering a groove. A detailed discussion of this can be found in Chapter 5 and Viktorov (1967), but intuitively the case is made here that part of the energy is diffracted to body waves, at the impedance contrast imposed by the groove. Conservation of energy ensures that the transmitted surface wave is of less energy than the incident one. This procedure is schematically depicted in Figure 4.1; the arrows represent directions of wave propagation, not actual ray paths. With the dimensions of the aluminum block *in casu*, the diffracted body-wave energy does not re-enter the surface wave model in the times that we measure the wave field. Therefore, diffractions are a loss term that can be represented by a characteristic loss parameter. This is the attenuation mean free path: the distance ℓ_a in the scattering medium it takes for the incident field to decay by a factor $1/e$. Of course this factor depends on the impedance contrast that the groove represents (in this case air/aluminum) and the density of scatterers (grooves per unit length).

Besides diffracted, the incident field is partially reflected *scattered* by the groove. This is also – conserving energy – a source of decay of the transmitted surface wave, denoted by

¹This was done in close collaboration with Matthew Haney (Haney *et al.*, 2003; van Wijk *et al.*, 2003b).



Figure 4.2. Side-view of paths for energy in grooved aluminum. Scattering of the incident surface wave causes loss of the transmitted field (left), but energy can be gained by being re-reflected in the direction of propagation (right).

the characteristic $1/e$ decay distance, called the extinction mean free path ℓ^* . The difference from the loss to body wave diffraction is that the scattered energy stays in our 1D surface model. In fact, when the reflected surface wave encounters another groove, it can reflect once more, and travel – delayed and weakened by two reflection events, but still – in the original direction of the incident field (Figure 4.2). This means that scattering is both a loss and a gain term when we make up the energy balance. Note the analogy to body wave propagation in thin layers, where O’Doherty & Anstey (1971) show that the transmitted wave is shaped by *peg-leg* multiples; waves that scattered an even number of times in layers thinner than the dominant wavelength (Banik *et al.*, 1985; Shapiro & Zien, 1993). Finally, note that scattering and absorption enter the energy balance in fundamentally different ways. This leads to the ability to separate these effects in the laboratory, later in the Chapter.

Radiative transfer takes the energy balance described above for a medium with a random distribution of scatterers, and states that the average intensity as a function of time and place, takes the following form:

$$(\partial_t + v \cdot \nabla) \text{intensity} = \text{source} - \text{loss} + \text{gain}. \quad (4.1)$$

The left-hand side of equation (4.1) is the total time derivative of the intensity. On the right-hand side, loss and gain mechanisms in addition to sources determine the dynamic behavior. In the absence of loss or gain, this equation becomes the advection, or one-way wave, equation. Using the same form as equation (4.1), the scalar (no mode conversions at the scatterers) radiative transfer equation valid for any dimension is

$$\begin{aligned} \frac{\partial I(\mathbf{r}, \Omega, t)}{\partial t} + v \hat{n}(\Omega) \cdot \nabla I(\mathbf{r}, \Omega, t) &= S(\mathbf{r}, \Omega, t) - \frac{1}{\tau_s} I(\mathbf{r}, \Omega, t) - \frac{1}{\tau_a} I(\mathbf{r}, \Omega, t) + \\ &\frac{1}{\tau_s} \int \frac{1}{\sigma_s} \frac{\partial \sigma_s}{\partial \Omega'} I(\mathbf{r}, \Omega', t) d\Omega', \end{aligned} \quad (4.2)$$

where $I(\mathbf{r}, \Omega, t)$ is the intensity, or average squared wave field, at position \mathbf{r} propagating in direction Ω , v is the group velocity of the average (coherent) wave field, \hat{n} is the unit vector in the direction of propagation, and $S(\mathbf{r}, \Omega, t)$ is the angle-resolved source function. The differential scattering cross section, $\partial \sigma_s / \partial \Omega'$, describes the exchange of energy traveling from direction Ω into direction Ω' . The characteristic time between these exchanges is τ_s ,

the scattering mean free time. The total scattering cross section, σ_s , is the energy exchanged into all directions:

$$\sigma_s = \int \frac{\partial \sigma_s}{\partial \Omega'} d\Omega'. \quad (4.3)$$

Attenuation is addressed by including the characteristic absorption time τ_a . Using terminology originally coined by Clausius in 1858, it is common to define mean free paths for scattering and absorption, ℓ_s and ℓ_a , according to the relations $\ell_s = v\tau_s$ and $\ell_a = v\tau_a$. The scattering mean free path, ℓ_s , can be thought of as the typical distance a wave travels between scatterings. Under most circumstances, ℓ_s is inversely proportional to the number density of scatterers, ρ , and their scattering cross section:

$$\ell_s = \frac{1}{\rho\sigma_s}. \quad (4.4)$$

This equation is called the independent scattering approximation and it holds when the scatterers are separated by more than a wavelength. It can be obtained from a stationary phase argument applied to the average wave field in random media (Ishimaru, 1997). From equation (4.4), ℓ_s contains information about the product of ρ and σ_s in a way analogous to a wave reflected from an interface containing information about the acoustic impedance.

4.4 Radiative transfer in 1D

Because in 1D only two directions of propagation exist, a general expression for the differential scattering cross section, appearing under the integral in equation (4.2), is

$$\frac{\partial \sigma_s(\Omega, \Omega')}{\partial \Omega'} = E_f \delta(\Omega' - \Omega) + E_b \delta(\Omega' - \Omega - 180^\circ), \quad (4.5)$$

where E_b and E_f represent amounts of energy back-scattered and forward-scattered divided by the energy of the incident wave. Their sum is equal to the total scattering cross section:

$$\sigma_s = E_b + E_f. \quad (4.6)$$

Hence, in equation (4.2), the differential scattering cross section divided by the total scattering cross section becomes

$$\frac{1}{\sigma_s} \frac{\partial \sigma_s(\Omega, \Omega')}{\partial \Omega'} = \frac{E_f}{E_b + E_f} \delta(\Omega' - \Omega) + \frac{E_b}{E_b + E_f} \delta(\Omega' - \Omega - 180^\circ). \quad (4.7)$$

The ratios $E_f/(E_b + E_f)$ and $E_b/(E_b + E_f)$ are denoted by F and B respectively, where $B + F = 1$. In the case of isotropic scattering, $B = F = 0.5$ (Paasschens, 1997).

For a general 1D scatterer, B and F can be related to the total transmission and reflection coefficients of a thin bed, T_t and R_t (Sheng, 1995):

$$B = \frac{|R_t|^2}{|R_t|^2 + |T_t - 1|^2} \quad \text{and} \quad F = \frac{|T_t - 1|^2}{|R_t|^2 + |T_t - 1|^2}. \quad (4.8)$$

Note that a thin bed consists of two interfaces, and hence R_t and T_t are not simple reflection and transmission coefficients. The quantities R_t and T_t can be related to a geometric summation of the interface reflection and transmission coefficients via generalized rays (Aki & Richards, 1980).

Inserting equation (4.7) into equation (4.2), we obtain that

$$\begin{aligned} \frac{\partial I(x, \Omega, t)}{\partial t} + v \hat{n}(\Omega) \frac{\partial I(x, \Omega, t)}{\partial x} &= S(x, \Omega, t) - \frac{1}{\tau_s} I(x, \Omega, t) - \frac{1}{\tau_a} I(x, \Omega, t) + \\ &\frac{1}{\tau_s} \int [F \delta(\Omega' - \Omega) + B \delta(\Omega' - \Omega - 180^\circ)] I(\mathbf{r}, \Omega', t) d\Omega' = \\ &\frac{B}{\tau_s} I(x, \Omega + 180^\circ, t) - \frac{B}{\tau_s} I(x, \Omega, t) - \frac{1}{\tau_a} I(x, \Omega, t) + S(x, \Omega, t), \end{aligned} \quad (4.9)$$

where we have used the fact that $B + F = 1$. Equation (4.9) can be evaluated for the two possible directions in 1D, $\Omega = 0^\circ$ or 180° . Here, these directions are referred to as right and left, respectively. For simplicity, the total intensity propagating in direction $\Omega = 0^\circ$, $I(\mathbf{r}, 0^\circ, t)$, is represented by I_r , $I(\mathbf{r}, 180^\circ, t)$ is I_l , and the source function is split into S_r and S_l . The coordinate system is defined such that $\hat{n}(0^\circ) = 1$ and $\hat{n}(180^\circ) = -1$. The two equations that describe the propagation of right-going and left-going intensities are

$$\frac{\partial I_r}{\partial t} + v \frac{\partial I_r}{\partial x} = \frac{B}{\tau_s} (I_l - I_r) - \frac{I_r}{\tau_a} + S_r, \quad (4.10)$$

$$\frac{\partial I_l}{\partial t} - v \frac{\partial I_l}{\partial x} = \frac{B}{\tau_s} (I_r - I_l) - \frac{I_l}{\tau_a} + S_l. \quad (4.11)$$

This system of partial differential equations comprises radiative transfer in 1D and has been derived by other methods (Goedecke, 1977). In Appendix B.3, the system of partial differential equations is solved for both I_r and I_l . For now, we solve for the total intensity, $I_t = I_r + I_l$, since this is commonly measured in practice.

Two new quantities emerge from adding and subtracting equations (4.10) and (4.11). In addition to the total intensity, I_t , the net right-going intensity, $I_n = I_r - I_l$, appears. Similarly, the source function can be expressed as its total and net right-going components: $S_t = S_r + S_l$ and $S_n = S_r - S_l$. The result of adding equations (4.10) and (4.11) is

$$\frac{\partial I_t}{\partial t} + v \frac{\partial I_n}{\partial x} = -\frac{I_t}{\tau_a} + S_t, \quad (4.12)$$

Subtracting equations (4.10) and (4.11) yields:

$$\frac{\partial I_n}{\partial t} + v \frac{\partial I_t}{\partial x} = -\frac{2B}{\tau_s} I_n - \frac{I_n}{\tau_a} + S_n. \quad (4.13)$$

From these two equations, we derive a single partial differential equation in terms of what

we measure, I_t , by taking the spatial derivative of equation (4.13):

$$\frac{\partial}{\partial t} \frac{\partial I_n}{\partial x} + v \frac{\partial^2 I_t}{\partial x^2} = \left[-\frac{2B}{\tau_s} - \frac{1}{\tau_a} \right] \frac{\partial I_n}{\partial x} + \frac{\partial S_n}{\partial x}. \quad (4.14)$$

But we know from equation (4.12) that

$$\frac{\partial I_n}{\partial x} = \frac{1}{v} \left[-\frac{I_t}{\tau_a} - \frac{\partial I_t}{\partial t} + S_t \right]. \quad (4.15)$$

Substituting equation (4.15) into equation (4.14) yields a single partial differential equation in I_t . Omitting some algebraic manipulation, we find that

$$\begin{aligned} \frac{\partial^2 I_t}{\partial x^2} &= \frac{1}{v^2} \frac{\partial^2 I_t}{\partial t^2} + \left[\frac{2B}{v\ell_s} + \frac{2}{v\ell_a} \right] \frac{\partial I_t}{\partial t} + \frac{1}{\ell_a} \left[\frac{2B}{\ell_s} + \frac{1}{\ell_a} \right] I_t - \\ &\quad \left[\frac{2B}{v\ell_s} + \frac{1}{v\ell_a} \right] S_t - \frac{1}{v^2} \frac{\partial S_t}{\partial t} + \frac{1}{v} \frac{\partial S_n}{\partial x}, \end{aligned} \quad (4.16)$$

Equation (4.16) encapsulates a wealth of information. First of all, in the absence of a source, the scattering and attenuation show up in both the first and zeroth order time derivatives of the total intensity. For a medium with no scattering or attenuation, $\ell_s^{-1} = \ell_a^{-1} = 0$, we are left with the 1D wave equation. Also, in order to solve for the Green's function of the total intensity, we cannot simply insert a δ -source into the homogeneous form of equation (4.16). Instead, a more complicated combination of the source and its time and spatial derivatives must be inserted.

4.4.1 The Green's function of the total intensity

To solve for the Green's function of the total intensity in 1D, we find the Green's function of the homogeneous form of equation (4.16) and construct the total intensity Green's function from it. First, take an impulsive total source function:

$$S_t = \delta(x)\delta(t), \quad (4.17)$$

and a general form for its net right-going component:

$$S_n = cS_t, \quad (4.18)$$

where $c \in [-1, 1]$. The parameter c allows the radiation pattern of the impulsive source function to directionally vary from left-going ($c = -1$), to isotropic ($c = 0$), to right-going ($c = 1$), and to any combination in between. After inserting this source into equation (4.16), we find that the *effective source*, denoted S_e , is a combination of a δ -function in time, its time derivative, and its x -derivative:

$$S_e = \left[\frac{2B}{v\ell_s} + \frac{1}{v\ell_a} \right] \delta(x)\delta(t) + \frac{1}{v^2} \delta(x)\delta'(t) - \frac{c}{v} \delta'(x)\delta(t). \quad (4.19)$$

This effective source can be constructed from the knowledge of the Green's function, P of the homogeneous form of equation (4.16):

$$\frac{\partial^2 P}{\partial x^2} = \frac{1}{v^2} \frac{\partial^2 P}{\partial t^2} + \left[\frac{2B}{v\ell_s} + \frac{2}{v\ell_a} \right] \frac{\partial P}{\partial t} + \frac{1}{\ell_a} \left[\frac{2B}{\ell_s} + \frac{1}{\ell_a} \right] P - \delta(x)\delta(t). \quad (4.20)$$

Note that P is not the Green's function for the total intensity. This equation is a variation of the telegraph equation, there being a zeroth order derivative appearing due to the presence of attenuation. Morse & Feshbach (1953) solve the Green's function of the telegraph equation via a spatial Fourier transform and a Laplace transform over time. Applying the same technique, the Green's function of equation (4.20) can be readily obtained by generalizing their solution:

$$P(x, t) = \frac{v}{2} \exp(-Bvt/\ell_s - vt/\ell_a) J_0 \left(\frac{B}{\ell_s} \sqrt{x^2 - v^2 t^2} \right) u(vt - |x|), \quad (4.21)$$

where $u(vt - |x|)$ is the unit step-function, guaranteeing causality. This Green's function only differs from the one for the telegraph equation by the exponential damping factor due to attenuation. The Green's function for the total intensity, denoted I_t , can be expressed in terms of the above Green's function through equation (4.19):

$$I_t = \left[\frac{2B}{v\ell_s} + \frac{1}{v\ell_a} \right] P + \frac{1}{v^2} \frac{\partial P}{\partial t} - \frac{c}{v} \frac{\partial P}{\partial x}. \quad (4.22)$$

Taking the necessary derivatives of P , we obtain for $B \in [0, 1]$ and $c \in [-1, 1]$:

$$I_t(x, t) = \frac{1}{2} \exp(-Bvt/\ell_s - vt/\ell_a) [(1-c)\delta(vt+x) + (1+c)\delta(vt-x) + \frac{B}{\ell_s} u(vt - |x|) \left[I_0 \left(\frac{B}{\ell_s} \sqrt{v^2 t^2 - x^2} \right) + \frac{vt + cx}{\sqrt{v^2 t^2 - x^2}} I_1 \left(\frac{B}{\ell_s} \sqrt{v^2 t^2 - x^2} \right) \right]], \quad (4.23)$$

where I_0 and I_1 are the modified Bessel functions of the zeroth and first orders. These should not be confused with the symbols used for the various intensities (I_t , I_r , I_l , and I_n). A previous result by Hemmer (1961) is obtained from equation (4.23) for the case of an isotropic source ($c = 0$) and isotropic scattering, $B = 0.5$.

The Green's function for the total intensity can be broken up into two parts. The term with the δ -function propagates like a wave and is called the coherent intensity. The rest of the total intensity is referred to as the incoherent intensity. It does not propagate ballistically, and Appendix B.4 shows that at late times it propagates diffusively. Also, Appendix B.3 shows that each Bessel function represents a different direction of propagation for the incoherent energy. The decay of coherent intensity due to scattering, described by the first exponential term in equation (4.23), goes with distance by the factor ℓ_s/B and not ℓ_s . This new length scale, determining the decay of the coherent energy, is called the *extinction* mean free path, ℓ^* . The fact that $\ell^* \neq \ell_s$ is unique to 1D (Paasschens, 1997).

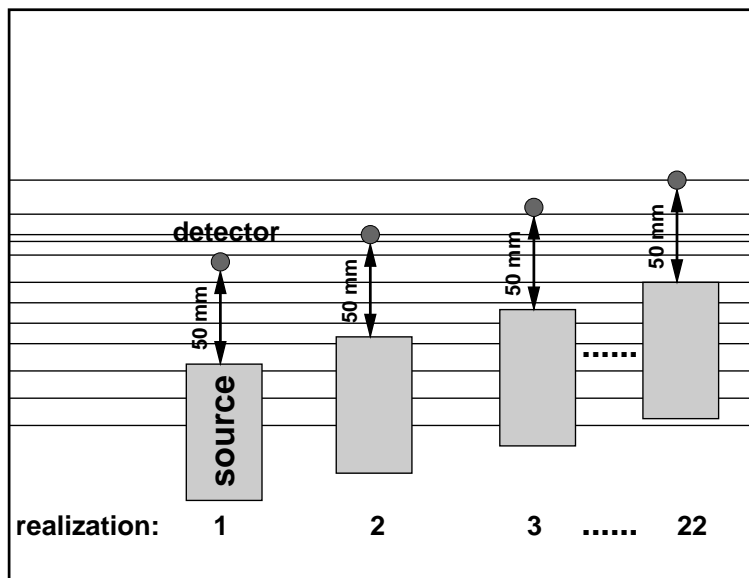


Figure 4.3. Top-view of the procedure to obtain an ensemble average.

4.5 Radiative transfer on the grooved face

To obtain ensemble measurements over the disordered medium, particle velocity measurements at fixed source-detector distances are collected for different positions in the groove sequence (Figure 4.3). We used 3 sets of 22 realizations with the detector 25, 50 and 75 mm from the leading edge of the source. Figure 4.4 contains waveforms recorded at 50 mm source-detector spacing. It shows particle velocity for the 22 source-detector locations in the ensemble measurement. Around 0.025 ms all traces contain relatively large amplitudes that are in phase. This is the coherent signal. This part of the signal is independent of local variations in the scattering distribution, whereas the later arrivals (also known as *coda*) vary in phase and amplitude for each source-detector location. This is the incoherent signal due to scattering from the micro-structure in the medium. These features are even more clear in the average trace in the left panel of Figure 4.5: while the incoherent signal tends to average out, the coherent signal is enhanced in the averaging procedure. The right panel contains the ensemble-averaged intensities. The total intensity is the average of each squared particle velocity trace from the left panel, and the coherent intensity is the square of the mean of the particle velocity traces. The coherent intensity is smoothed by a running window of width 25 samples to suppress large fluctuations caused by zero crossings intrinsic to the coherent wave forms. By definition, the coherent intensity is less than the total intensity (Ishimaru, 1997).

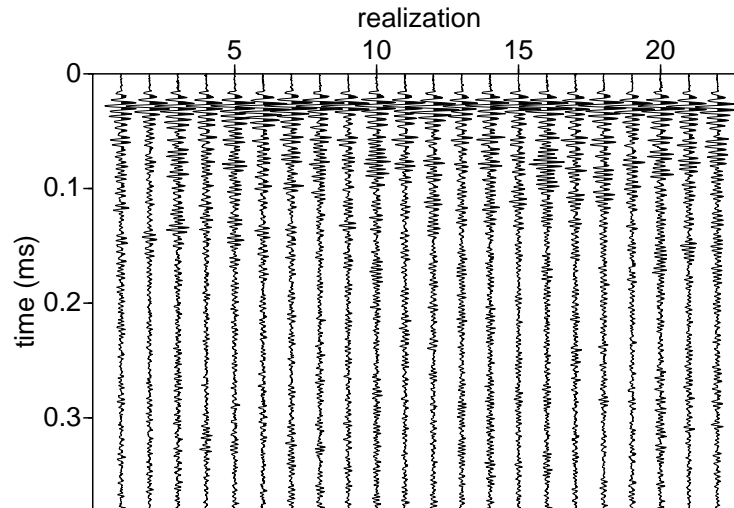


Figure 4.4. Particle velocity at 50 mm source-detector offset for 22 locations of the source-detector pair within the groove sequence.

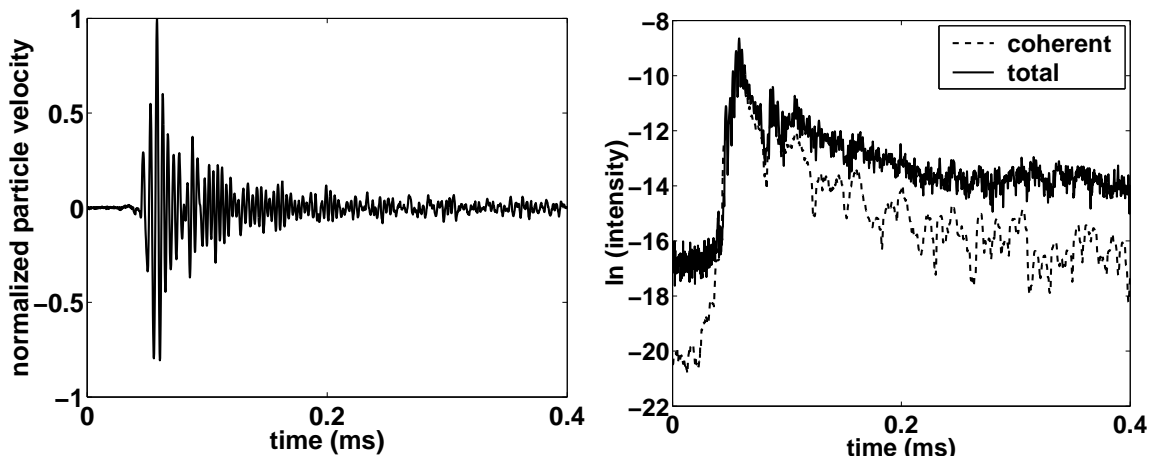


Figure 4.5. Data at 50 mm source-detector offset. The left panel is the average particle velocity for the 22 realizations, and the right panel the natural logarithm of the total and coherent intensity.

4.5.1 Fitting the data with radiative transfer

Recapping, the Green's function for the 1D scalar radiative transfer equation with attenuation and a directional source ($c = 1$ in equation (4.23)) is

$$G(x, t) \propto \exp(-vt(R/\ell_s + 1/\ell_a)) \times \left[2\delta\left(\frac{\ell_s}{R}(vt - x)\right) + u(vt - x) \left(I_0(\eta) + \sqrt{\frac{vt+x}{vt-x}} I_1(\eta) \right) \right]. \quad (4.24)$$

The argument of the Modified Bessel functions of order zero (I_0) and one (I_1) is

$$\eta = \frac{R}{\ell_s} \sqrt{(vt)^2 - x^2},$$

where v is the energy velocity and u the step function to assure causality in the system. The energy losses to body wave diffractions at the grooves are modeled by the attenuation term ℓ_a . R is the backscattering cross-section for a single groove and ℓ_s is the scattering mean free path. Note that R and ℓ_s are coupled, so they cannot be resolved individually from expression (4.24).

The term with the Dirac delta function represents the ballistic propagation of energy, or the coherent signal, from here on denoted as $C(x, t)$, while the Bessel functions describe the incoherent signal $I(x, t)$. Each Bessel function represents the incoherent energy propagating in a specific direction (Appendix B.3). Both terms decay exponentially depending on attenuation (in our case body-wave diffraction) and scattering; the latter being a redirection of energy due to scattering. For late times ($vt \gg x$) the coherent energy is zero and the incoherent signal simplifies to the diffusion equation used to model the data in Chapter 3.

We now determine the scattering and absorption mean free paths and the energy velocity using the radiative transfer equation by fitting the laboratory data. Since we are able to separate both the data and the radiative transfer equation into a coherent and an incoherent part, we will treat the parameter fitting problem for each part separately. From here on, we drop scaling terms in the solution to the radiative transfer equation for clarity, since all data and simulations are normalized with respect to the first source-detector offset.

The Green's function in expression (4.24) is convolved with the band-limited input energy pulse. Actually determining the source signal is not trivial, because as the source is moved across the grooves, the source wavelet is not that of the source mounted on the smooth surface of aluminum. Not only is the coupling between the source wedge and the model different, its characteristics are changed as scattering takes place at the grooves *under* the source wedge, effectively low-pass filtering the source wavelet, shown in Appendix A.

Coherent intensity The coherent part $C(x, t)$ of the Green's function of the 1D attenuative radiative transfer equation is

$$C(x, t) \propto \delta(x - vt) \exp(-\alpha vt). \quad (4.25)$$

The solid lines in Figure 4.6 are the modeled envelopes of the coherent intensity for $\alpha = R/\ell_s + 1/\ell_a = 17.8 \text{ m}^{-1}$ and velocity $v = 1818 \pm 123 \text{ m/s}$. In our case the coherent velocity equals the transport velocity, even though especially for resonant scattering the velocity of the coherent signal can be significantly higher than the group (transport) velocity (e.g., Page *et al.*, 1996; Kuga *et al.*, 1993; van Albada *et al.*, 1991). The energy of the coherent signal travels dispersively. We therefore model the energy velocity to be a function of frequency: as lower frequency surface waves penetrate the model deeper, they travel for a larger part undisturbed by the scatterers, while higher frequencies are slowed by stronger scattering due to the grooves (Appendix C). The smaller, secondary peak in the coherent intensity is not modeled. This peak is most likely a part of the source wavelet, not accounted for in the model.

Incoherent intensity The incoherent intensity is the coherent intensity subtracted from the total intensity. The data are the solid lines in Figure 4.7. The dashed lines are the result of modeling the incoherent part $I(x, t)$ of equation (4.24):

$$I(x, t) \propto \exp(-\alpha vt) \left(I_0(\eta) + \sqrt{\frac{vt+x}{vt-x}} I_1(\eta) \right). \quad (4.26)$$

Using the energy velocity of 1818 m/s and $\alpha = 17.8 \text{ m}^{-1}$, the resulting fits in Figure 4.7 are for $R/\ell_s = 11.1 \text{ m}^{-1}$. We only fit the incoherent signal at intermediate times. At short times the incoherent data are incomplete, and at late times energy comes back into the system from reflections off the back of the model, but in the intermediate time window, the fit describes the average measured incoherent intensity. Note that the incoherent intensity for all three offsets is of equal amplitude in this intermediate window.

Fitting parameters With $R/\ell_s + 1/\ell_a = 17.8 \text{ m}^{-1}$ and $R/\ell_s = 11.1 \text{ m}^{-1}$, the absorption length is $\ell_a = 0.15 \text{ m}$. If $R = 0.5$, the mean of the range of possible values, the scattering mean free path is $\ell_s = 0.05 \text{ m}$. Data at source-detector offsets around ℓ_s , put us in the transitional regime from ballistic to diffusive energy propagation.

Formally, these parameters in the radiative transfer are functions of frequency, since our scatterers have a finite depth, while surface wave frequencies sample different depths of the model. However, the data fit is obtained with an average value of the scattering and absorption parameters. To account for dispersion in the coherent signal, only the energy velocity was treated as a function of frequency.

A direct application in geophysics of radiative transfer modeling is presented in Appendix D: independent estimates of scattering and intrinsic attenuation (Q), are known to double as direct indicators of fluid content in the rock. Partial saturation of the rock has little effect on the scattering properties, but the bulk motion of the fluid attenuates the seismic energy.

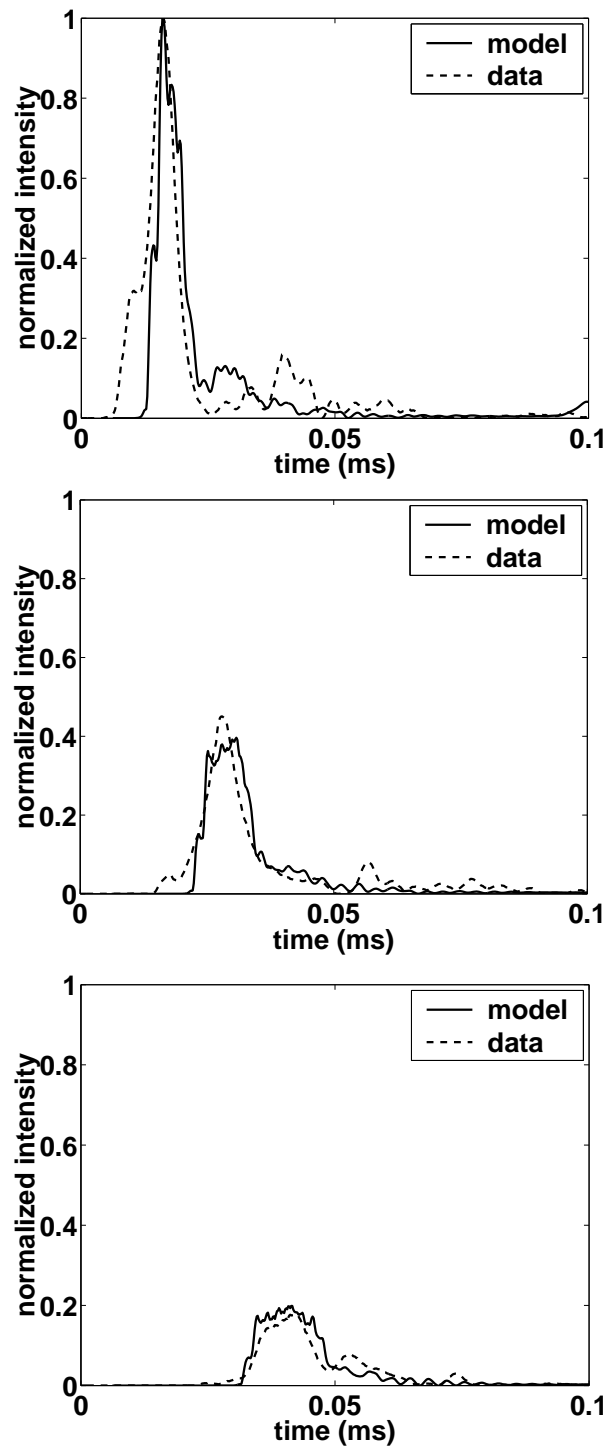


Figure 4.6. Comparison between the measured and modeled coherent intensities for source-detector offsets of 25 (top), 50 (middle) and 75 mm (bottom).

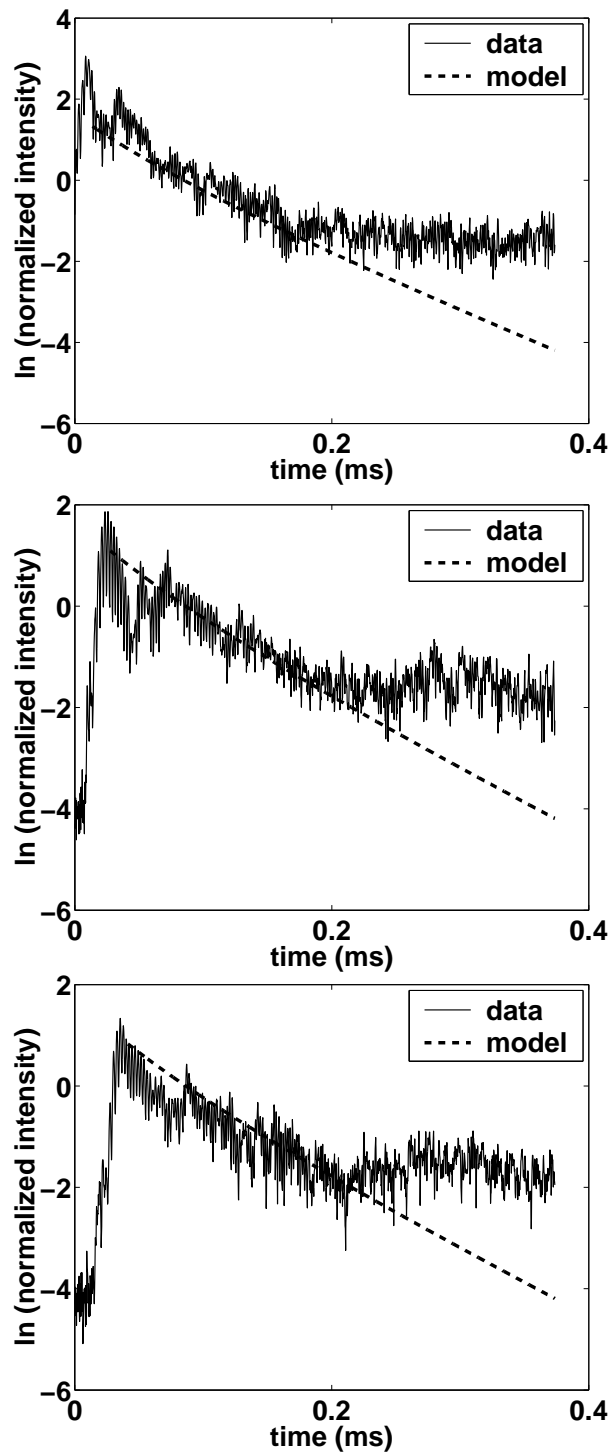


Figure 4.7. Comparison between the measured and modeled incoherent intensities for source-detector offsets of 25 (top), 50 (middle) and 75 mm (bottom).

4.6 Conclusions

This strongly scattering surface wave model shows great flexibility in understanding multiple scattering media. Not only can we measure phase and amplitude of the surface waves (allowing us to separate the coherent from the incoherent signal), we also have the advantage of probing the medium between scatterers. We found that in a region around a mean free path, 1D radiative transfer can describe our scattering medium, so that fitting both the coherent and incoherent energy allows us to estimate average values for the scattering and absorption mean free paths.

Chapter 5

Multiple scattering at the microscopic scale

5.1 Summary

Spectral-element simulations of surface wave propagation in our surface wave laboratory provide us with a powerful tool for understanding the complex dynamics of diffraction and scattering. For example, we see in both the experiment and simulation diffracted body waves which are weak precursors to the dominant surface waves; these events may be analogous to diffractions from the Earth's core-mantle boundary. In addition, the numerical code confirms flexural modes of the thin areas of aluminum between grooves and the influence of the source wedge itself on the wave field.

5.2 Introduction

Bulk properties of the propagation, including attenuation and dispersion, were studied to describe the scattering model on the macroscopic scale in Chapter 3, while Chapter 4 shows results of modeling multiple scattered data in the mesoscopic regime, separating scattering attenuation from absorption. This Chapter describes two-dimensional (2D) numerical simulations of the physical system, using the spectral-element method (SEM) (e.g., Komatitsch & Tromp, 1999) to model the ultrasonic experiment with sharp topographic features, and investigate subtle details in the laboratory data on the scale of the individual scatterer (i.e. the microscopic scale).

A 2D version of the spectral-element method (SEM), mostly used and validated in seismology (e.g., Priolo *et al.*, 1994; Faccioli *et al.*, 1997; Komatitsch & Vilotte, 1998; Komatitsch & Tromp, 1999, 2002a; Komatitsch *et al.*, 2002), is used to simulate wave propagation at ultrasonic frequencies in a model that contains a large number of sharp grooves. The SEM is ideal for this purpose because of its flexibility to mesh the grooved structure based on a geometrically non-conforming mesh and also because it has been shown to be accurate to model surface waves (Komatitsch & Tromp, 1999). The simulations can be compared to measurements at every surface location, because the optical detector can record at any location on the surface of the block. The source in the simulations is the analytic solution to a Rayleigh wave (e.g., Komatitsch *et al.*, 1999) and detectors are located in a line directly in front of the source. Attenuation is so weak in aluminum that elastic simulations are meaningful.

Henceforth, I refer to the vertical component of the particle velocity measured in laboratory experiments as *data* and to the numerical results as *simulations*.

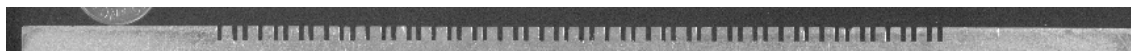


Figure 5.1. Scan at 2400 dots-per-inch of the side of the grooves. The top-left corner shows part of a penny (a US\$ one-cent coin) for scale: the total length of the block is 215 mm.

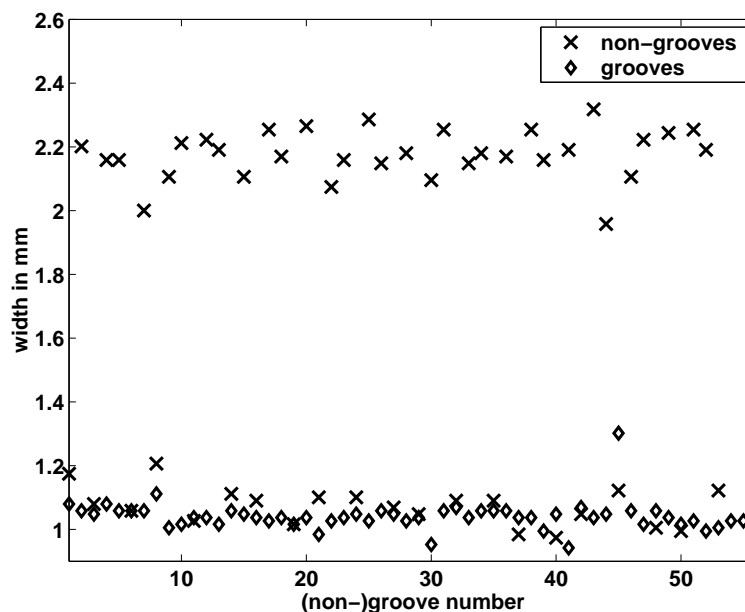


Figure 5.2. Width of the grooves and non-grooves. The basic unit h for the Fibonacci sequence is overall more than 1 mm.

5.3 Numerical modeling

Near the surface, the block is modeled by a mesh with cells whose size is on the order of a scatterer, but the mesh size is doubled twice with depth to reduce the total number of cells (i.e. spectral elements) to 11426. The wave field is interpolated on a polynomial of degree $N=4$ in each quadrangular cell; the total number of grid points is 184141. The time step used in the explicit integration scheme is $\Delta t = 10^{-5}$ ms and the signal is propagated or 0.2 ms.

5.4 Scanning the grooves

Nominally, the grooves are 1-mm wide and 2.75-mm deep, while the dominant wavelength of the surface waves is about 15 mm, so there are many scatterers per wavelength as waves propagate perpendicular to the grooves. However, a scan of the grooves at 2400 dots-per-inch shows detailed deviations from the Fibonacci pattern (Figure 5.1). Overall the grooves are indeed 2.75-mm deep, but their width varies, as shown in Figure 5.2.

5.5 Comparing data and simulations

Let us compare data and simulations at 20 detector locations at 5-mm increments on the smooth side of the model, and on the first 42 non-grooves along a line perpendicular to the grooves (strong scattering). In both experiments, the source-detector offset for the first trace is 2 mm.

The data and simulations on the smooth aluminum surface are shown in Figure 5.3. Both panels show a large direct surface-wave arrival, followed by a reflection from the far end of the aluminum block. The wavelet in the data has some energy after the main pulse caused by ringing in the transducer. This energy is not included in the source term of the simulations. The data show little attenuation and no evidence of reflections from the sides of the block, which means that the source energy emitted has little geometrical spreading, justifying 2D elastic simulations.

Figure 5.4 shows the data (top) and simulations (bottom) for waveforms in the strong scattering case. At each groove, energy is partially reflected, causing the direct arrival to be attenuated, and the group velocity to be lowered compared to the un-scattered wave propagation, which has been shown to lead to a diffusive character of energy propagation (Scales & van Wijk, 2001). The strongest events are interfering surface waves, which look qualitatively similar in the two panels. These strong events show coherence in the sense that a single phase can be tracked from one detector location to the next, whereas for late times, scattering causes arrivals to be incoherent from trace to trace. In general, detailed differences between the numerical mesh and the grooved block are amplified at later times as a result of multiple scattering, much as in coda wave interferometry (Snieder *et al.*, 2002): waves bouncing back-and-forth numerous times between scatterers highlight errors in the numerical representation. The later events especially show greater discrepancy in amplitude, because the path-lengths for the multiply scattered events are longer than the early arrivals, so that neglecting attenuation in aluminum becomes a significant source for the difference between data and simulations.

The amplitude of the maximum correlation between data and simulations directly reflects the accuracy of the simulations: correlation of unity means that data and simulations are identical. It is our experience that discrepancies between the physical and numerical models on the order of a fraction of the size of a single scatterer have a noticeable influence on the accuracy of the simulations.

The maximum cross-correlation for the case of strong scattering is overall lower than for the experiment on the smooth side (Figure 5.5). Especially for source-detector distances greater than 90 mm from the source, small discrepancies between the physical model and numerical representation get amplified. However, the simulations are of such precision that data and simulations on a non-groove with the size on the order of 1 mm show considerably more energy at later times than traces on the thicker non-grooves. An example of this is detector 12, compared to detector 4 (Figures 5.6 and 5.7, respectively): the relatively thin ridge of aluminum under detector 12 is excited in a 300-kHz resonance (Figure 5.8). While this mode is too low in frequency to represent a trapping of energy in the non-groove, it is possible that this resonance is a flexural mode of the thin non-groove (Rossing & Fletcher,

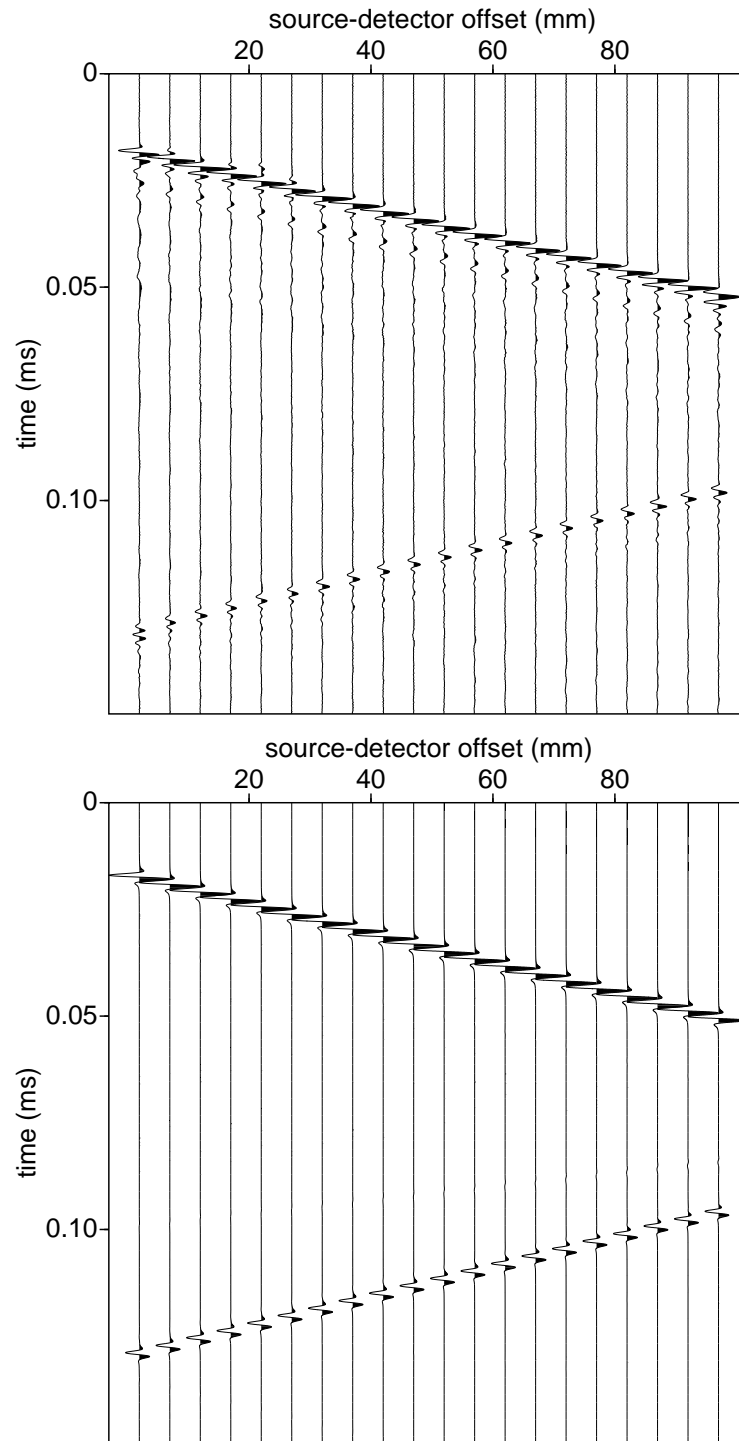


Figure 5.3. Data (top) and simulations (bottom) for wave fields on the smooth side of the model.

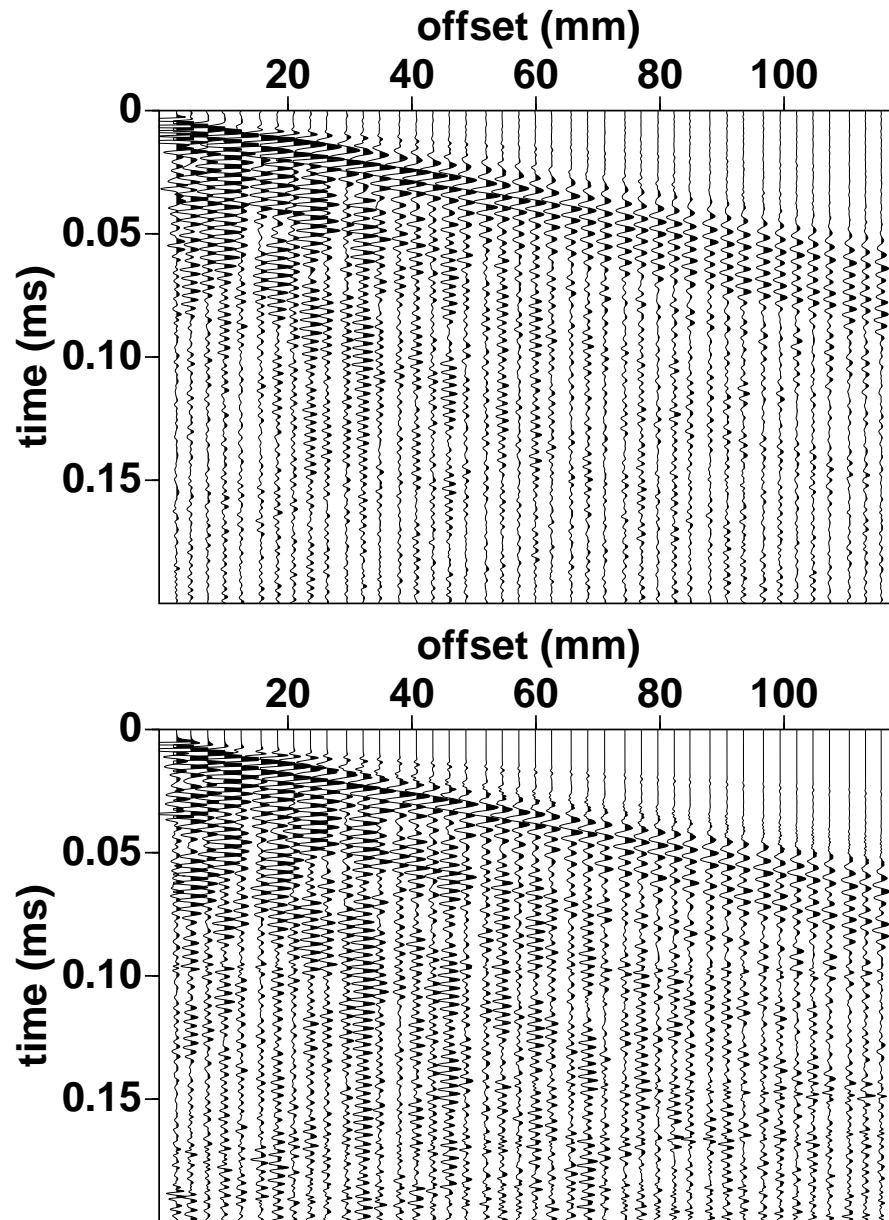


Figure 5.4. Data (top) and simulations (bottom) for wave fields on the grooved side of the model. The main energy consists of surface waves bouncing between grooves, but the small-amplitude, faster events are body-waves diffracted at the grooves.

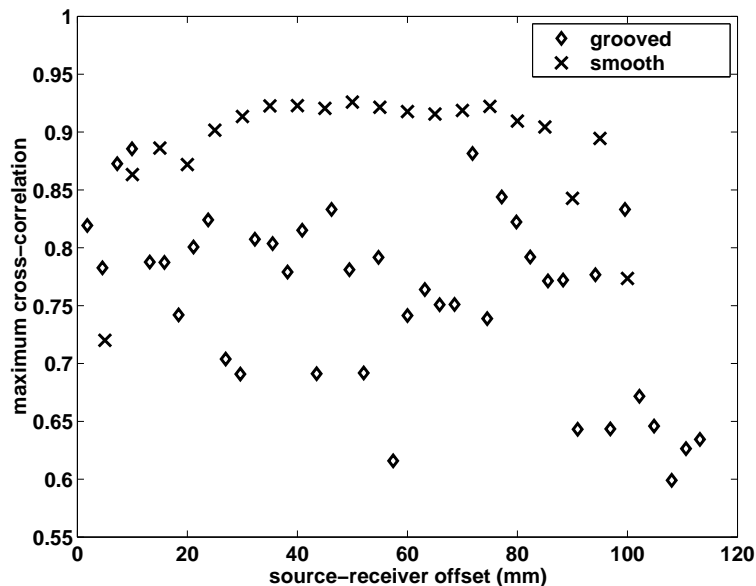


Figure 5.5. Maximum correlation between data and simulations, both on the smooth side and the grooved side of the model. Identical traces have correlation 1.

1995).

The source wedge acts as an additional scatterer in the model, causing the maximum correlation on the smooth side of the aluminum to be smallest for detector 1 (Figure 5.5). Note the differences in amplitude and phase in the direct arrival and more clearly in the reflected event (Figure 5.9), when compared to the other traces in Figure 5.3. This is due to the influence of the source wedge, which is located only 2 mm from detector 1. The second reflection from the side near the source is almost undetected in the data, because it requires the Rayleigh wave to travel along the surface between the bottom of the source wedge and the aluminum block. This is not an obstacle in the simulations, because the source is modeled by an analytically incident Rayleigh wave. A completely non-contacting experimental setup with a laser source in addition to the optical detector (Scales & Malcolm, 2003) would be ideal, but for this application the laser source is too high in frequency for energy to penetrate the groove sequence significantly.

5.6 Precursors

In the strong-scattering case, relatively lower-amplitude and faster events arrive before the main surface-wave energy (Figure 5.4). The data panel shows two coherent events with the P-wave velocity of aluminum. The first, starting at $t=0$, is caused by the angle-beam transducer producing some P-waves in addition to surface-wave energy. This event is not present in the simulations, because the source is a pure Rayleigh wave. The second event

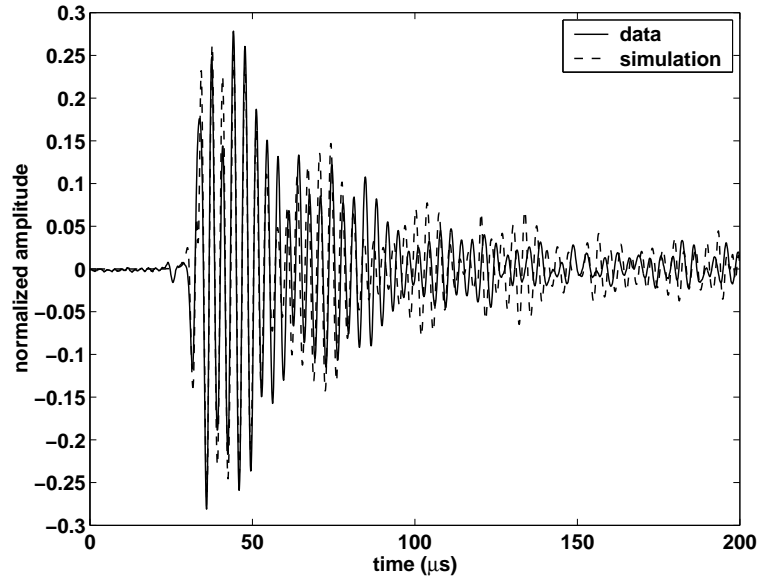


Figure 5.6. Comparison between data and simulations for detector 4 on the grooved side of the model. This detector is located on a thick non-groove.

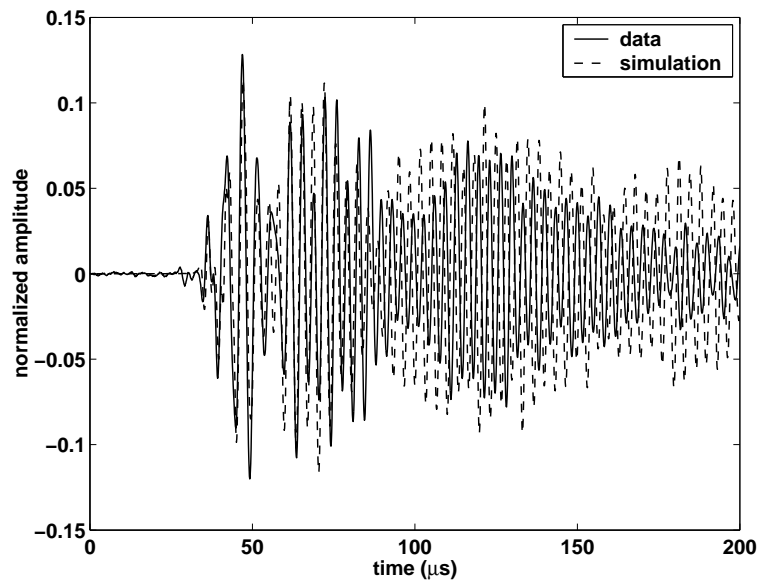


Figure 5.7. Comparison between data and simulations for detector 12 on the grooved side of the model. This detector is located on a thin non-groove. Note the relatively stronger amplitudes at later times than for detector 4.

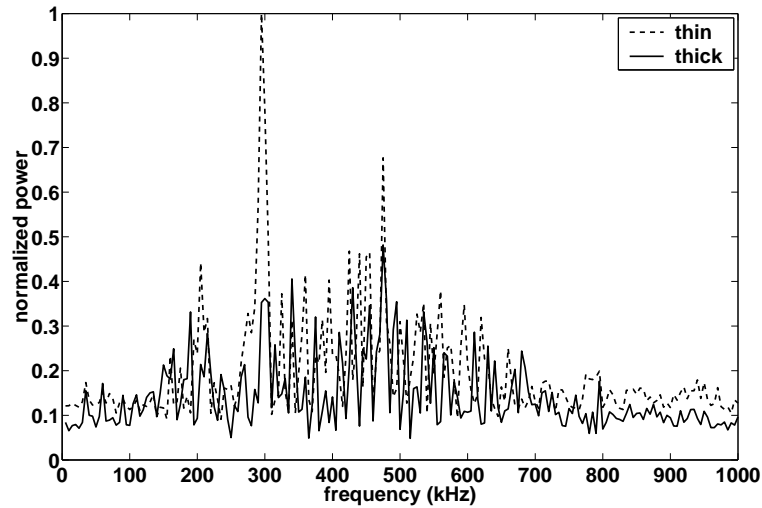


Figure 5.8. Driving the source with a sweep of sinusoids, shows that the thin grooves resonate at 300 kHz. The results are the average over five thick and five thin grooves, respectively.

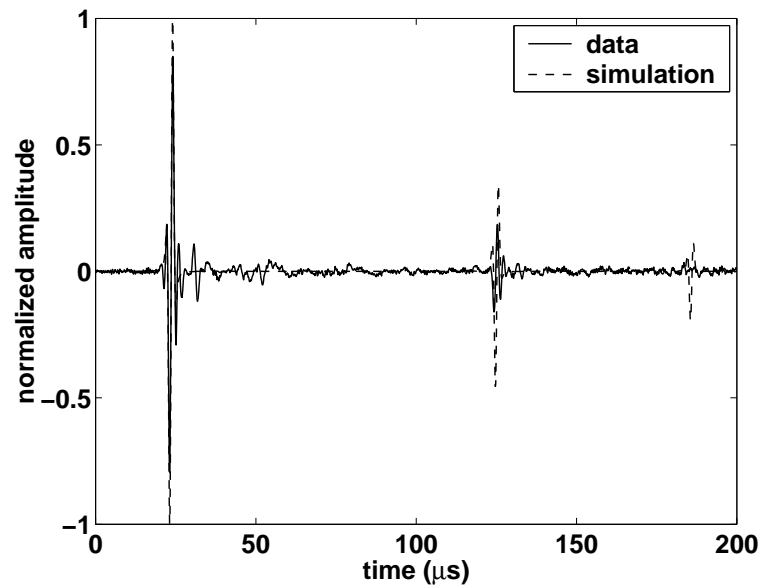


Figure 5.9. Comparison between data and simulations for detector 1 on the smooth side of the model.

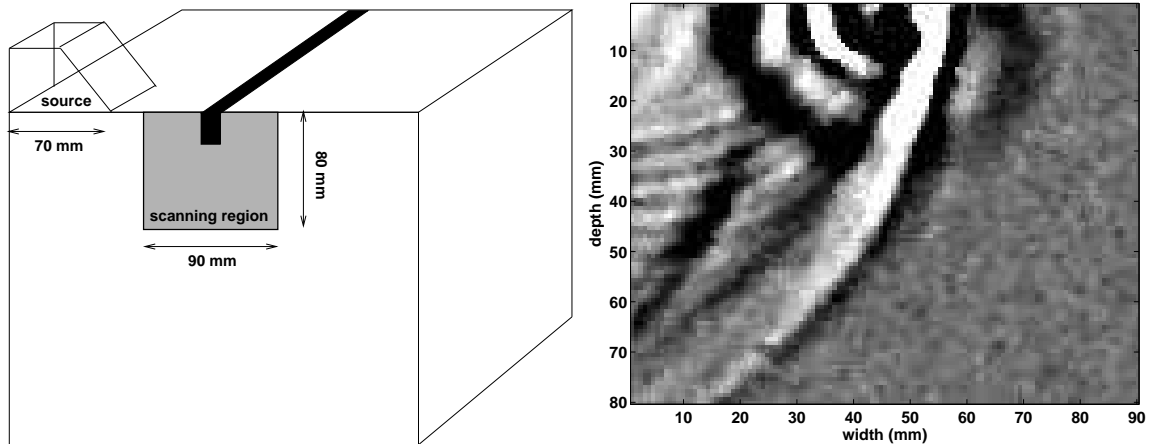


Figure 5.10. Left: experimental configuration, where the source is perpendicular to a single groove on the top of the block, while the detector scans the side. Right: snap-shot of particle motion in the scanned region after the incident field scattered off a single groove.

with a P-wave velocity cannot be seen until the 6th or 7th trace at $t = 0.01$ ms, but is confirmed by the simulations. These events are spherical body-wave fronts diffracted at the individual grooves, which arrive before the Rayleigh waves, and may be analogous to precursors to the seismic phase PKKP in global seismology, believed to be caused by scattering at the rough boundary between the Earth's outer-core and mantle (Earle & Shearer, 1997).

To support the existence of body-wave precursors to the surface-wave energy, a second experiment was conducted, where the source is mounted on the side of the aluminum model with a single groove, while the detector scans the side of the model (see the left panel of Figure 5.10). The right panel of Figure 5.10 shows a snap-shot of particle motion, measured shortly after the incident wave interacted with the single groove. The side of the aluminum block breaks the symmetry of the Rayleigh-wave motion purely in the x - and z -direction, creating particle motion in the y -direction. In the top-left corner, one can see energy due to ringing of the source, and the incident field is the (close to) linear event. The circular events are body-waves scattered off the single groove. Scattering to body waves is stronger in the backward direction, but significant P-wave energy travels ahead of the surface wave, causing the precursors observed in Figure 5.4.

5.7 Conclusions

Relatively small-amplitude features from individual scatterers are confirmed by spectral-element simulations. For example, body-wave precursors to the main surface-wave energy are caused by diffraction from the scatterers, which may be analogous to PKKP precursors, believed to be caused by scattering at the core-mantle boundary. Also, flexural resonance

modes were detected for the thinner spaces between grooves.

Chapter 6

Measuring, imaging and suppressing scattered surface waves

6.1 Summary

Near-surface scattering can contaminate the arrival of energy from target reflectors. We developed a 3D wave-theoretical method to reduce the presence of near-surface scattering on the records, as a multi-channel alternative for short-wavelength static corrections. The method was successfully tested on laboratory data, excited and monitored with a computer controlled, non-contacting system.

6.2 Introduction

When a wave front travels through a complex overburden, it is disturbed by scattering from heterogeneities. For a detailed structural image of the deeper subsurface it is important to minimize these disturbances in arrival time and amplitude of upcoming reflections. Currently, residual static correction methods correct for rapid variations in arrival times of a reflector, but these techniques are based on a model that assigns the same uniform time shift to each trace from a distinct surface location (e.g., Wiggins *et al.*, 1976), assuming vertical ray paths through the overburden. Such corrections are usually referred to as time- and surface-consistent corrections (Taner *et al.*, 1974). Although statics techniques are based on this simple (transmission) model of the subsurface, they can be effective in many cases. However, in a strongly heterogeneous shallow subsurface, this statics model breaks down (e.g., Combee, 1994). Neglecting (multiply) scattered waves, as in the static assumption, can degrade the high-frequency content of the data, due to destructive interference of rapidly varying traces during stacking.

We estimate a surface impedance distribution of the region directly under the receivers from one particular event and subsequently predict and subtract the scattered energy for the entire record, improving resolution of the target reflectors. This method is based on an integral-equation formulation of the scattering process near the surface, developed by Delft University of Technology (Blonk & Herman, 1994; Ernst *et al.*, 2002; Campman *et al.*, 2003). We present examples based on laboratory models, where we excite and measure wave fields that are scattered at the near surface. With our non-contacting data acquisition, receiver intervals are less than the dominant wavelength, allowing us to filter in the wavenumber domain, as with the dense receiver arrays that are currently being tested in exploration

geophysics (Baeten *et al.*, 2000).

6.3 Scattered noise model

Our objective is to obtain an estimate of the complete wave field without scattered energy from near-surface heterogeneities. On account of linearity of the elastic wave field, the vertical velocity component $v(\mathbf{x}, t)$, measured at position $\mathbf{x} = (x, y, z)$ and due to a fixed vertical point source of force type can be written as

$$v(\mathbf{x}, t) = v^0(\mathbf{x}, t) + v^1(\mathbf{x}, t). \quad (6.1)$$

Here, v is the measured field, v^0 is the field that would have been measured if the overburden were homogeneous and v^1 is the part of the wave field that accounts for scattering from heterogeneities close to the acquisition surface. Thus, we want an estimate of v^0 . Our approach is to find the scattered noise, v^1 , and then subtract it from the data (as expressed in equation 6.1). From the elastic wave-equation for particle displacement, we can derive an approximate integral representation for the scattered noise in terms of the vertical particle velocity, measured at the surface z_0 :

$$v^1(\mathbf{x}_l, z_0, \omega) = \int_{\mathbf{x}'_l \in \Sigma} u_z^G(\mathbf{x}_l - \mathbf{x}'_l, \Delta z, \omega) \sigma(\mathbf{x}'_l, z_1, \omega) v(\mathbf{x}'_l, z_1, \omega) d\mathbf{x}'_l, \quad (6.2)$$

where u_z^G is the vertical component of the Green's displacement tensor, due to a vertical point force (Campman *et al.*, 2003). Horizontal position is denoted by $\mathbf{x}_l = (x, y)$, z_1 is the scattering depth and $\Delta z = z_0 - z_1$. The impedance distribution is denoted by σ and ω is angular frequency. The surface Σ is the area occupied by the receivers (i.e. the acquisition surface). If the scattering takes place close to the surface ($z_1 \approx z_0$), we can approximate the field at z_1 by the field recorded field at depth z_0 and we can calculate the scattered field v^1 , once we know σ . Note that the integral is over a surface and we thus expresses scattering by a scattering volume in terms of a surface impedance distribution. The validity of this assumption for scattering of surface waves close to the surface is investigated in exploration geophysics by Blonk & Herman (1994) and in global seismology by Snieder (1986). To account for variations in the actual depth of the scatterers we allow the impedance distribution to depend on frequency.

6.4 Inverse scattering

Suppose the data contain many reflections from deeper layers. All these events excite surface waves at the same heterogeneities close to the acquisition surface. This implies that we can use the scattered energy from a single event to estimate the impedance distribution and use it to predict the scattered energy on *every* reflection using equation (6.2). In fact, this is comparable to residual statics methods, where one selects a strong reflection event from the data, to derive the time-shifts for each trace separately. Instead of this single-channel operation, we now select one event to derive an impedance distribution to estimate

the scattered energy (i.e. a multi-channel operation).

First, we select an event:

$$v(\mathbf{x}, t) = d(\mathbf{x}, t) + r(\mathbf{x}, t), \quad (6.3)$$

where v are the data, d is the selected event and r denotes the rest of the data. Selecting d can be done by time windowing. The window should be long enough to include scattering tails but it should not include other events. Next, we decompose the strong event $d(\mathbf{x}, t)$, in a similar way as in equation (6.1):

$$d(\mathbf{x}, t) = d^0(\mathbf{x}, t) + d^1(\mathbf{x}, t). \quad (6.4)$$

Here, d^0 is the field in the near surface that would exist without scattering and d^1 is the scattered field, excited by the incident field being scattered from heterogeneities in the near-surface. The impedance model is obtained from back-propagating the near-surface scattered energy with the Green's function derived in Campman *et al.* (2003). The impedance distribution is determined by minimizing an L^2 -norm, using conjugate gradient. To set up the minimization scheme, we write equation (6.2) for a single event, in the form

$$d^1 = K\sigma, \quad (6.5)$$

where σ is the surface impedance distribution and the operator K is defined as

$$\{K\sigma\}(\mathbf{x}_l, z_0, \omega) = \int_{\mathbf{x}'_l \in \Sigma} u_z^G(\mathbf{x}_l - \mathbf{x}'_l, \Delta z, \omega) \sigma(\mathbf{x}'_l, z_1, \omega) d(\mathbf{x}'_l, z_1, \omega) d\mathbf{x}'_l. \quad (6.6)$$

We then minimize the squared difference between the observed scattered field and the reconstructed scattered field, regularized by the norm of the distribution of scatterers:

$$F = \frac{\|d^1 - K\sigma\|^2}{\|d^1\|^2} + \lambda \|\sigma\|^2, \quad (6.7)$$

where the size of λ determines the penalty on the norm of the distribution of scatterers. By assumption, the scatterers are close to the surface so that in equation (6.6), we can substitute the field at depth z_1 with the field at z_0 , leaving σ the only unknown. In contrast to Born-type imaging methods, this method accounts for multiply scattered waves.

6.5 Experiment 1: a surface wave test

We measure the wave field on the surface of an aluminum block, excited by a pulsed infrared laser (e.g., Scruby & Drain, 1990). We focused the laser beam on a line to create a line surface wave source. This wave front is scattered by a cylindrical cavity with a diameter of 2 mm and a depth of 3 mm, which is roughly the size of the dominant wavelength. The wave field is detected using a scanning laser interferometer that measures the vertical component of the particle velocity on the surface of the model via the Doppler shift (Scales

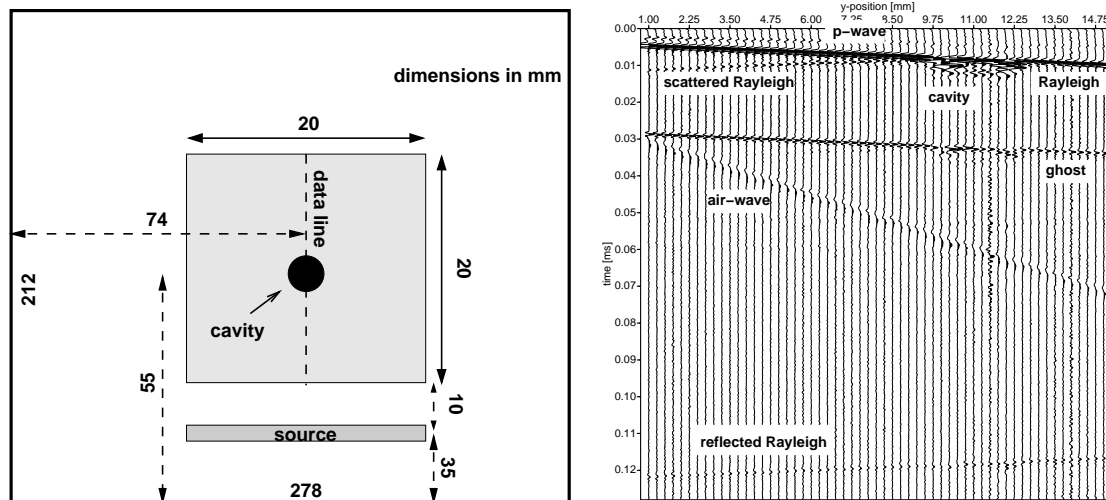


Figure 6.1. Left: top view of the aluminum block with cavity. The light shaded area is the area covered by the receivers. The source-width (dark shade) is 0.5 mm. Right: in-line panel (see left panel for location) of the data, where strong reflectors have been identified.

& van Wijk, 1999). Traces are recorded at 0.25 mm intervals, which implies about 10 samples per wavelength. The left panel of Figure 6.1 is the top view of the experimental configuration, while the right panel is an in-line panel of the 3D data set, with several surface-wave events and a body wave (P-wave) identified. The quality of these data is such, that no pre-processing is required.

6.5.1 Results

We use data from Experiment 1 to validate the algorithm. First, we select an event by time windowing; in this case the direct Rayleigh wave with the energy scattered by the cavity, plotted in the left panel of Figure 6.2. We separate the incoming (d^0) from the energy scattered by the cavity (d^1). To do so, we exploit the near-planar character of the incoming wave. Since a two-dimensional spatial Fourier transformation maps a plane wave to a point in the wavenumber-frequency domain, we can use this to separate the incoming plane wave from its local perturbations. These perturbations are attributed to the presence of the cavity. The separated scattered field d^1 is shown in the middle panel of Figure 6.2. Next, we estimate the impedance distribution using equation (6.7) and an independent estimate of the background velocity of the surface waves in aluminum. From the data, we estimate that $c_R \approx 3000$ m/s.

The impedance distribution for this in-line data set is shown in the right panel of Figure 6.2. It coincides with the actual location and in-line width of the cavity. Applying this sequence of steps for the entire 3D data volume, leads to the image of Figure 6.3. The

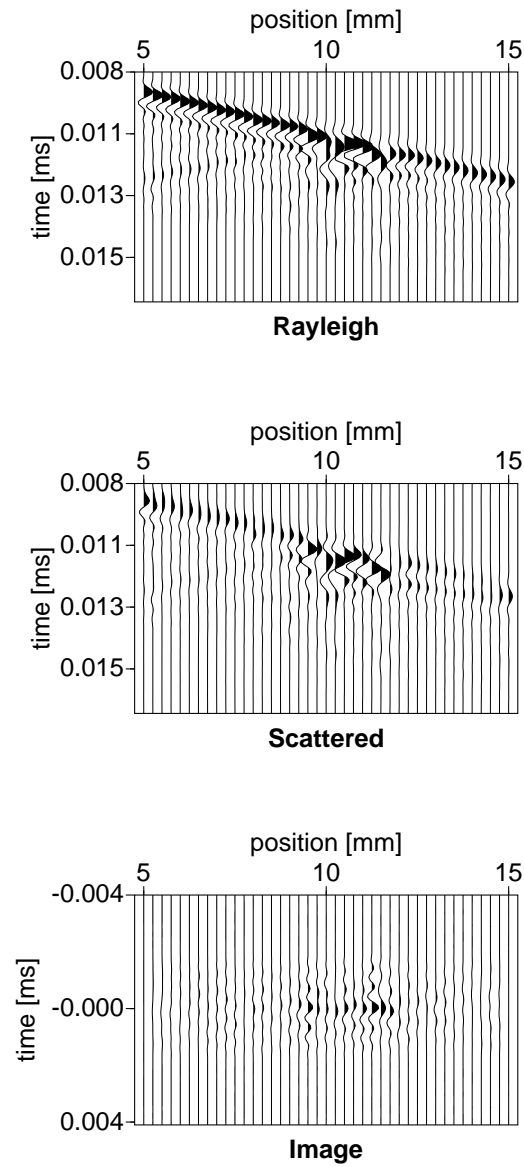


Figure 6.2. Top: part of the direct Rayleigh wave (event d in the text). This event is used to derive the scattered energy d^1 . Middle: separated scattered energy, using a wavenumber frequency domain filter. Bottom: image of the cavity along the same line.

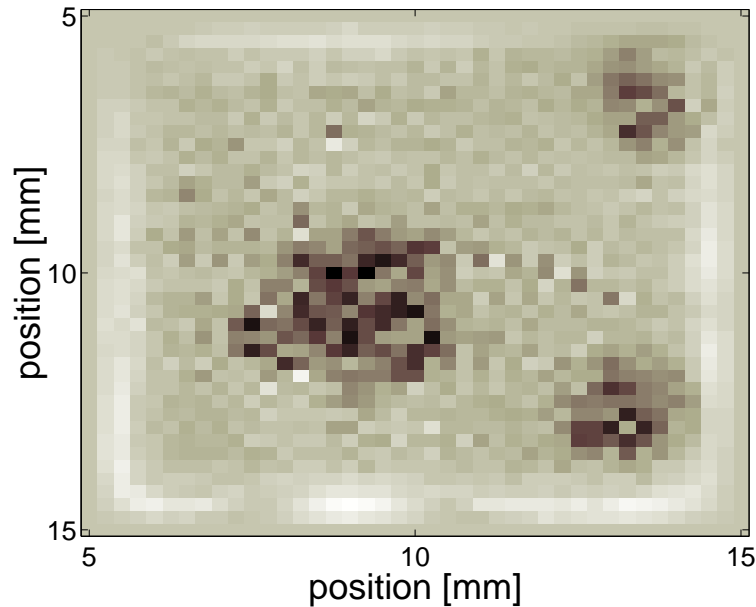


Figure 6.3. The image for Experiment 1, showing the right position and size of the cavity. The gray scale is proportional to the density of the medium. The right half of the image contains two anomalies that are due to two air bubbles between the reflective tape and the aluminum.

circular shape of the impedance distribution, slightly to the left and down from center, represents the actual shape and location of the cavity. Anomalies in the right corners of the figure are due to local data quality issues; air made its way under the reflective tape used to enhance performance of the laser vibrometer. The ability of the algorithm to image these air bubbles adds to the strength of the method.

Having obtained an estimate of the spatial impedance distribution from the direct Rayleigh wave, we calculate the scattered wave field v^1 for a *different* event. This event has not been used for determining the impedance distribution, and therefore prediction of the scattered field is a good test of the method. We select the Rayleigh wave that is reflected by the end of the aluminum block behind the source. We call this event the *ghost*, shown in the left panel of Figure 6.4. The predicted scattered field is shown in the middle panel. Finally, we obtain the wave field minus the scattered energy from equation (6.1), shown in the right panel of Figure 6.4. We observe that the scattering has been effectively removed and continuity of the reflector has increased.

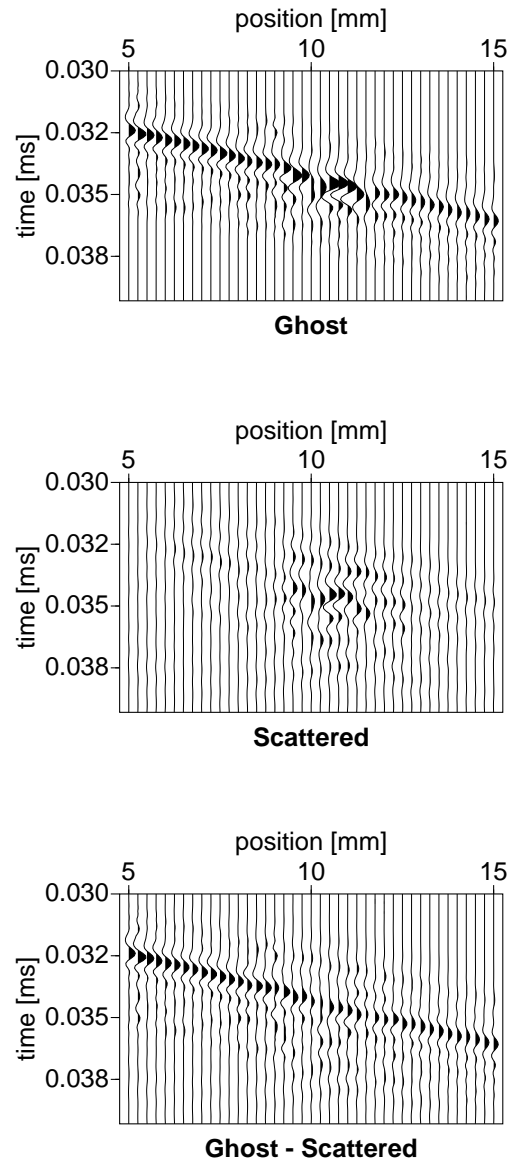


Figure 6.4. Top: the ghost Rayleigh wave. Middle: the predicted scattered field for this event. Bottom: the ghost Rayleigh wave after removing predicted near-surface scattering.

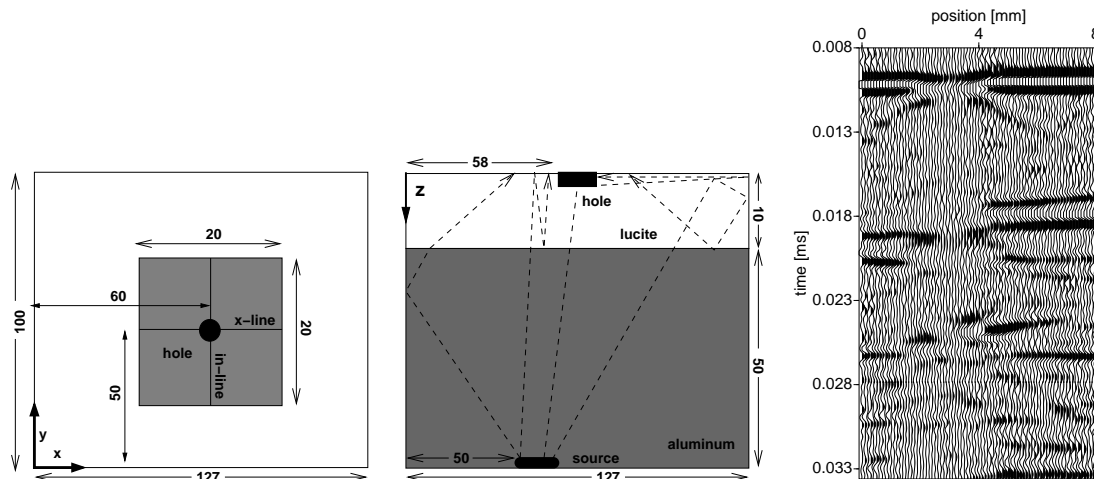


Figure 6.5. Top- (left) and side-view (middle) of the two-layered model with cavity. Right: seismogram of part of the data through the cavity.

6.6 Experiment 2: a transmission model

In order to simulate an upcoming reflection, Experiment 2 involves a transmission model. Body waves are excited at the bottom of a two-layered model, where an aluminum layer is topped by a Lucite layer, in which we drilled a 2-mm wide and 3-mm deep cavity. When the body waves reach the surface, energy is scattered at the cavity. We record the wave field in a 4 cm² region, at 0.1 mm intervals. Compared to Experiment 1, these data are further complicated by the fact that they contain multiples from the layer boundary and reflections from the sides of the aluminum block as depicted in the side-view in the left panel of Figure 6.5. Data through the cavity show the multiples between the layers, reflections from the sides, all scattered by the cavity (right panel of Figure 6.5). Pre-processing of the data consisted of tapering-off low frequencies (including a dc-component) and then stacking each trace with four adjacent traces to boost signal-to-noise.

6.6.1 Results

The data in Experiment 2 present a more challenging test for the method, because of the multiples and the interfering reflections from the sides of the aluminum. Apart from the pre-processing of these data, the algorithm is applied in the same way as in Experiment 1. Again, we start by selecting a clear event. In this case we select the first upcoming reflection, shown in the left panel of Figure 6.6. We separate the incoming (d^0) from the energy scattered by the cavity (d^1), using a narrow wavenumber-frequency domain filter. The separated scattered field is shown in the middle panel. Using the surface wave velocity in Lucite ($c_R \approx 1000$ m/s), we estimate the impedance distribution, shown in the right

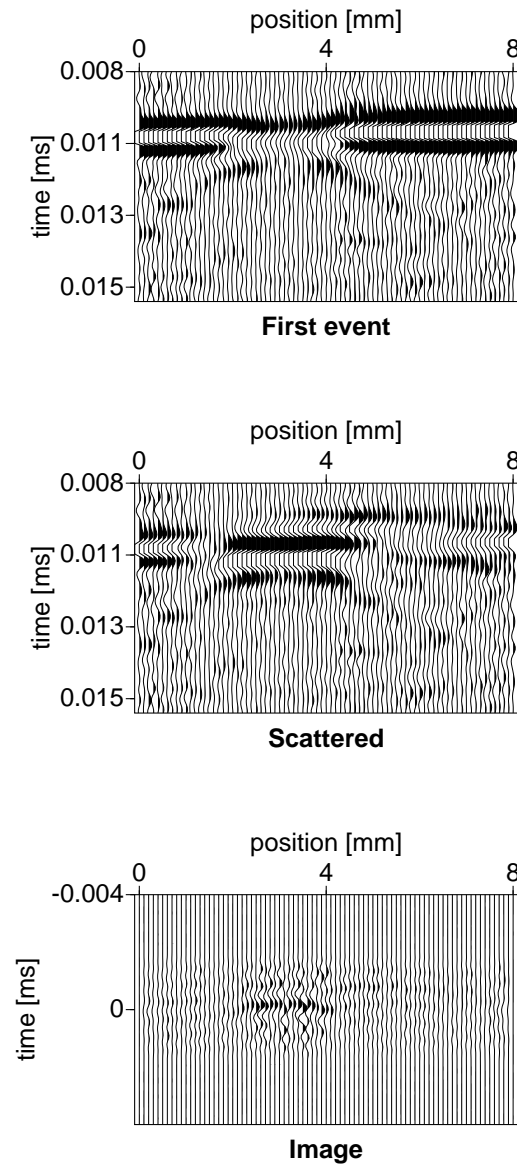


Figure 6.6. Top: the first upcoming event from the data. (event d in the text). This event is used to derive the scattered energy. Middle: separated scattered energy, d^1 , using a narrow wavenumber frequency domain filter. Bottom: image of the cavity along the same receiver line.

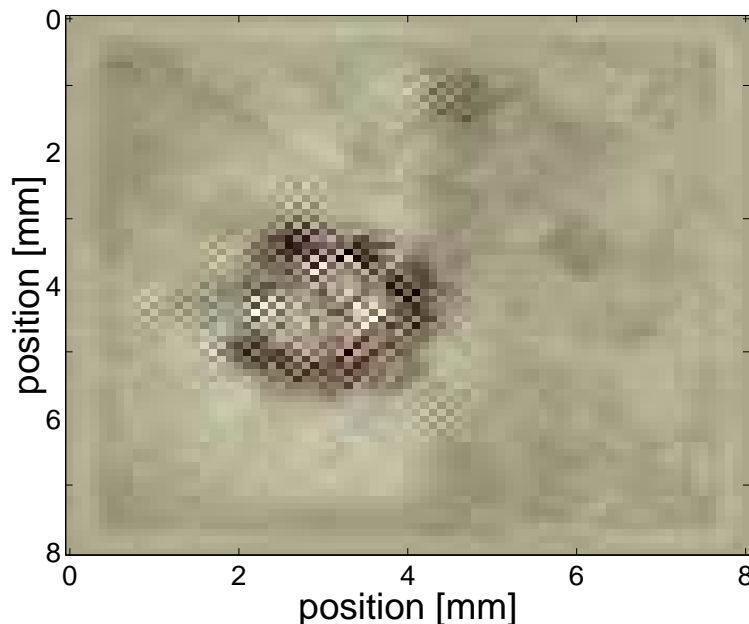


Figure 6.7. Top view of the image for Experiment 2, showing the right position and dimensions of the actual cavity. The gray scale is proportional to the density of the medium.

panel. Figure 6.7 is a top-view of the image at the surface for the entire 3D data volume. The dimensions and location of the image are in agreement with the actual cavity in the Lucite.

Finally, we predict the near-surface scattered field in the rest of the data. In the left panel of Figure 6.8 we show part of the data line crossing through the cavity, minus the first event used to construct the image. Thus, the data shown in the left panel of Figure 6.8 were not used to derive the impedance distribution. Because the surface wave velocity may not be accurately known, the desired result may still contain residual tails from surface waves, but these can be removed by dip filtering. In order to make a comparison between the data before and after applying the algorithm, we have used a dip filter on the input data v as well as in the output data v^0 . The filtered input data are shown in the middle panel of Figure 6.8. Obviously, the dip filter only removed the flanks of the surface waves, but not the apices, which have higher apparent velocities and were therefore unaffected by the filter. Especially this part of the surface waves is important to remove, because it is the interference between surface wave scattering and the incident field that diminishes the quality of the target reflector. The output v^0 after applying *the same* dip-filter is shown in the right panel of Figure 6.8. We conclude that the algorithm has improved the continuity of the reflectors.

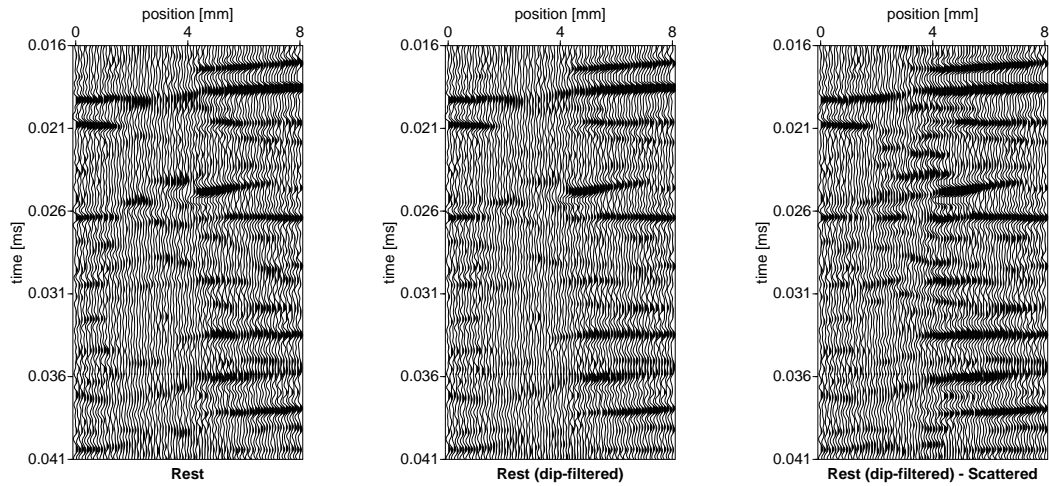


Figure 6.8. Left: part of the rest of the record. Middle: same as in the left panel but after dip-filtering to attenuate surface waves. Right: rest of the record after subtracting near-surface scattered energy and after dip-filtering.

6.7 Conclusions

We present a robust prediction-and-removal algorithm to attenuate strong near-surface scattering from seismic data. Using data from a laboratory-scale scattering experiments, we are able to estimate the surface impedance distribution using a single event. This impedance distribution is then used to predict and remove the scattered field from other events, restoring the continuity of target reflectors. A similar test on a more challenging multiple scattering experiment also gives promising results. The success of the algorithm is aided by dense 3D data acquisition, allowing filtering in the wavenumber domain.

Chapter 7

Concluding remarks

The study of our surface wave laboratory proved ideal to understand, and then exploit, wave propagation in disordered media. Tunability of the scattering strength, easy access, fast and dense acquisition in the lab and the longevity of surface waves provide a unique view *inside* the scattering medium.

Scattering induced attenuation and the decay of seismic velocities are caused by energy being transferred into the coda. These multiply scattered waves extract energy from the coherent pulse. This is why the coherent field decays exponentially due to absorption *and* scattering. It is the coherent wave that historically has been the only energy of interest in global and exploration geophysics. In medical imaging, scattering of light in biological tissue is so strong that the only recorded signal is incoherent. Their main *imaging* tool is a diffusion model. Being in the intermediate regime, where we have coherent and incoherent signal, allows a more robust medium parameter estimation. The tool of choice is radiative transfer, which describes both the coherent and the incoherent energy propagation in scattering media. Treating the scattering medium as a whole (macroscopically), medium parameters like the diffusion constant and energy velocity were revealed in scattered energy. However, in the intermediate regime, the mesoscopic scale, the treatment of the observations in terms of averaged intensity led to separate estimation of scattering attenuation and intrinsic absorption.

In higher dimensions, the radiative transfer equation becomes considerably more difficult since there are an infinite number of directions to scatter into, as compared to two directions in 1D (Paasschens, 1997). However, even in 1D, the rich character of radiative transfer is evident. Exponential decay is experienced by the direct wave due to scattering and absorption. Aspects of both wave and diffusive behavior emerge in the average total intensity, and, in the presence of both, a *mesoscopic* picture of the scattering medium can be formed.

The theory of radiative transfer has its limitations. The most severe is that it does not include wave interference. As a result of this, there exists a distance between source and receiver, known as the localization length, past which radiative transfer is incorrect. Sheng (1995) estimates that in 1D the localization length is approximately four mean free paths. This offers the possibility of an intermediate range (one to four mean free paths) where radiative transfer holds. Future work should attempt to find good bounds on this range in practice.

A direct application in geophysics of radiative transfer modeling is presented in Appendix D. Under many assumptions that need to be tested in future research, we obtain

independent estimates of scattering and intrinsic attenuation (Q). A firm handle on the explicit intrinsic attenuation is generally regarded a direct indicator of fluid content in the rock: partial saturation of the rock has little effect on the scattering properties, but the bulk motion of the fluid attenuates the seismic energy.

High precision measurements, backed by spectral-element numerical simulations, show (microscopic) details of the scattering behavior, like flexural resonance and surface wave precursors in the form of body wave diffractions. At this microscopic scale, the aluminum surface wave laboratory also provides a test-case for wave-equation based statics corrections. In this problem, near-surface scattered energy blurs reflections from seismic targets of interest at greater depth. The success of this application was aided by large degrees of freedom in non-contacting and dense data acquisition.

References

- Aki, K., & Chouet, B. 1975. Origin of coda waves: source, attenuation and scattering effects. *J. Geophys. Res.*, **80**, 3322–3342.
- Aki, K., & Richards, P. G. 1980. *Quantitative seismology: theory and practice*. Freeman.
- Anderson, H. L. (ed). 1989. *A physicist's desk reference; physics vade mecum*. 2nd edn. 335 East 45th Street, New York, NY 10017: American institute of Physics.
- Anderson, P. W. 1958. Absence of diffusion in certain random lattices. *Phys. Rev.*, **109**, 1492–1505.
- Asch, M., Kohler, W., Papanicolaou, G., Postel, M., & White, B. 1991. Frequency content of randomly scattered signals. *SIAM Review*, **33**, 519–625.
- Backus, G. 1962. Long wavelength anisotropy. *J. Geophys. Res.*, **67**, 4427–4440.
- Baeten, G., Belougne, V., Combee, L., Kragh, E., Laake, A., Martin, J., Orban, J., Ozbek, A., & Vermeer, P. L. 2000. Acquisition and processing of point receiver measurements in land seismic. *In: Expanded abstracts, 62nd Mtg.* B-06. Eur. Assn. Geosci. Eng.
- Banik, N. C., Lerche, I., & Shuey, R. T. 1985. Stratigraphic filtering, Part I: Derivation of the O'Doherty-Anstey formula. *Geophysics*, **50**, 2768–2774.
- Bleistein, N., Cohen, J. K., & Stockwell Jr., J. W. 2001. *Mathematics of multidimensional seismic imaging, migration and inversion*. New York: Springer-Verlag.
- Blonk, B., & Herman, G. C. 1994. Inverse scattering of surface waves : A new look at surface consistency. *Geophysics*, **59**, 963–972.
- Boas, D. A., Campbell, L. E., & Yodh, A. G. 1995. Scattering and imaging with diffusing temporal field correlations. *Phys. Rev. Lett*, **75**, 1855–1858.
- Boyce, W. E., & DiPrima, R. C. 1997. *Elementary differential equations*. New York: Wiley.
- Campillo, M., & Paul, A. 2003. Long-range correlations in the diffuse seismic coda. *Science*, **299**, 547–549.
- Campillo, M., Margerin, L., & Shapiro, N. 1999. Seismic wave diffusion in the Earth lithosphere. *Pages 383–404 of: Fouque, J.-P. (ed), Diffuse waves in complex media*. Kluwer.

- Campman, X. H., van Wijk, K., Scales, J. A., & Herman, G. C. 2003. Suppression of near-field scattered surface waves. *In: Extended Abstracts, 65th Mtg.* Eur. Assn. Geosci. Eng.
- Carpena, P., Gasparian, V., & Ortuño, M. 1995. Energy spectra and level statistics of Fibonacci and Thue-Morse chains. *Phys. Rev. B*, **51**(18), 12813–12816.
- Combee, L. 1994. Wavefield scattering by a 2-D near-surface elliptic anomaly. *Pages 1306–1309 of: Expanded Abstracts, 64th Ann. Intern. Mtg.* Soc. of Expl. Geoph.
- Cowan, M. L., Beaty, K., Page, J. H., Liu, Zhengyou, & Sheng, Ping. 1998. Group velocity of acoustic waves in strongly scattering media: Dependence on the volume fraction of scatterers. *Phys. Rev. E*, **58**(5), 6626–6636.
- Cowan, M. L., Jones, I. P., Page, J. H., & Weitz, D. A. 2002. Diffusing acoustic wave spectroscopy. *Phys. Rev. E*, **65**, 066605.
- Dahlen, F. A., & Tromp, J. 1998. *Theoretical global seismology*. Princeton, New Jersey: Princeton University Press.
- Dal Negro, L., Oton, C. J., Gaburro, Z., Pavesi, L., Johnson, P., Lagendijk, A., Righini, R., Colocci, M., & Wiersma, D. S. 2003. Light transport through the band-edge states of Fibonacci quasicrystals. *Phys. Rev. Lett.*, **90**(5), 055501–1,055501–4.
- Dally, J. W. 1978. Dynamic photoelastic studies of stress wave propagation. *Pages 3–21 of: Miklowitz, J., & Achenbach, J. D. (eds), Modern problems in elastic wave propagation*. New York: John Wiley & Sons.
- De Rosny, J., & Roux, P. 2001. Multiple scattering in a reflecting cavity: application to fish counting in a tank. *J. Acoust. Soc. Am.*, **109**(6), 2587–2597.
- Earle, P. S., & Shearer, P. M. 1997. Observations of PKKP precursors used to estimate small-scale topography on the core-mantle boundary. *Science*, **277**, 667–670.
- Ernst, F. E., Herman, G., & Ditzel, A. 2002. Removal of scattered guided waves from seismic data. *Geophysics*, **67**(4), 1240–1248.
- Faccioli, E., Maggio, F., Paolucci, R., & Quarteroni, A. 1997. 2D and 3D elastic wave propagation by a pseudo-spectral domain decomposition method. *J. Seismol.*, **1**, 237–251.
- Gellermann, W., Kohmoto, M., Sutherland, B., & Taylor, P. C. 1994. Localization of light waves in Fibonacci dielectric multilayers. *Phys. Rev. Lett.*, 633.
- Goedecke, G. H. 1977. Radiative transfer in closely packed media. *Journ. Opt. Soc. Am.*, **67**, 1339–1348.
- Groenenboom, J., & Snieder, R. K. 1995. Attenuation, dispersion and anisotropy by multiple scattering of transmitted waves through distributions of scatterers. *J. Acous. Soc. Am.*, **98**, 3482–3492.

- Haney, M., van Wijk, K., & Snieder, R. K. 2003. *Radiative transfer in 1D, and the connection to the O'Doherty-Anstey formula*. In CWP Project Review and submitted to Geophysics.
- Hemmer, P. C. 1961. On a generalization of Smoluchowski's diffusion equation. *Physica*, **27**, 79–82.
- Hendrich, A., Martinez, A. S., Maynard, R., & van Tiggelen, B. A. 1994. The role of the step length distribution in wave-diffusion. *Phys. Lett. A*, **185**, 110–112.
- Hennino, R., Trégourès, N., Shapiro, N. M., L. Margerin, L., Campillo, M., van Tiggelen, B. A., & Weaver, R. L. 2001. Observation of equipartition of seismic waves. *Phys. Rev. Lett.*, **86**(15), 3447–3450.
- Hess, P. 2002. Surface acoustic waves in materials science. *Physics Today*, March, 42–47.
- Ishimaru, A. 1997. *Wave propagation and scattering in random media*. Oxford University Press.
- Kennett, B. L. N. 1984. Guided wave propagation in laterally varying media – I. Theoretical development. *Geophys. J. R. astr. Soc.*, **79**, 235–255.
- Komatitsch, D., & Tromp, J. 1999. Introduction to the spectral-element method for 3-D seismic wave propagation. *Geophys. J. Int.*, **139**, 806–822.
- Komatitsch, D., & Tromp, J. 2002a. Spectral-element simulations of global seismic wave propagation-I. Validation. *Geophys. J. Int.*, **150**, 390–412.
- Komatitsch, D., & Tromp, J. 2002b. Spectral-element simulations of global seismic wave propagation-II. 3-D models, oceans, rotation, and self-gravitation. *Geophys. J. Int.*, **150**, 303–318.
- Komatitsch, D., & Vilotte, J. P. 1998. The spectral-element method: an efficient tool to simulate the seismic response of 2D and 3D geological structures. *Bull. Seism. Soc. Am.*, **88**, 368–392.
- Komatitsch, D., Vilotte, J. P., Vai, R., Castillo-Covarrubias, J. M., & Sánchez-Sesma, F. J. 1999. The spectral element method for elastic wave equations– application to 2-D and 3-D seismic problems. *Int. J. Num. Methods in Engeneering*, **45**, 1139–1164.
- Komatitsch, D., Ritsema, J., & Tromp, J. 2002. The spectral-element method, Beowulf computing, and global seismology. *Science*, **298**, 1737–1742.
- Kuga, Y., Ishimaru, A., & Rice, D. 1993. Velocity of coherent and incoherent electromagnetic waves in a dense strongly scattering medium. *Phys. Rev. B*, **48**(17), 13155–13158.
- Lemieux, P. -A., Vera, M. U., & Durian, D. J. 1998. Diffusing-light spectroscopies beyond the diffusion limit: The role of ballistic transport and anisotropic scattering. *Phys. Rev. E*, **57**(4), 4498–4515.

- Margerin, L., Campillo, M., Shapiro, N. M., & van Tiggelen, B. A. 1999. Residence time of diffusive waves in the crust as a physical interpretation of coda Q: application to seismograms recorded in Mexico. *Geoph. J. Int.*, **138**, 343–352.
- Mateeva, A. A. 2001. Spectral footprint of intrabed multiples. *Pages 255–268 of: CWP Project Review*, vol. 384. Center for Wave Phenomena, Colorado School of Mines.
- Morse, P., & Feshbach, H. 1953. *Methods of theoretical physics*. New York: McGraw-Hill.
- Narayanamurti, V., Dynes, R. C., Hu, P., Smith, H., & Brinkman, W. F. 1978. Quasiparticle and phonon propagation in bulk, superconducting lead. *Phys. Rev. B*.
- Nolet, G., & Dahlen, F. A. 2000. Wave front healing and the evolution of seismic delay times. *J. Geophys. Res.*, **105**(B8), 19,043–19,054.
- O’Doherty, R. F., & Anstey, N. A. 1971. Reflections on amplitudes. *Geophys. Prospecting*, **19**, 430–458.
- Paasschens, J. C. 1997. Solution of the time-dependent Boltzmann equation. *Phys. Rev. E*, **56**, 1135.
- Page, J. H., Sheng, P., Schriemer, H. P., Jones, I., Jing, X., & Weitz, D. A. 1996. Group velocity in strongly scattering media. *Science*, **271**(February), 634–637.
- Priolo, E., Carcione, J. M., & Seriani, G. 1994. Numerical simulations of interface waves by high-order spectral modeling techniques. *J. Acoust. Soc. Am.*, **95**, 681–693.
- Rossing, T. D., & Fletcher, N. H. 1995. *Principles of vibration and sound*. Springer-Verlag.
- Scales, J. A., & Malcolm, A. E. 2003. Laser characterization of ultrasonic wave propagation in random media. *Phys. Rev. E*, 046618.
- Scales, J. A., & van Vleck, E. S. 1997. Lyapunov exponents and localization in randomly layered media. *J. Comp. Phys.*, **133**, 27–42.
- Scales, J. A., & van Wijk, K. 1999. Multiple scattering attenuation and anisotropy of ultrasonic surface waves. *App. Phys. Lett.*, **74**, 3899–3901.
- Scales, J. A., & van Wijk, K. 2001. Tunable multiple-scattering system. *App. Phys. Lett.*, **79**, 2294–2296.
- Schuster, A. 1905. Radiation through a foggy atmosphere. *J. Astrophys.*, **21**, 1–22.
- Scruby, C. B., & Drain, L. E. 1990. *Laser ultrasonics*. Adam Hilger.
- Shapiro, S., & Zien, H. 1993. The O’Doherty-Anstey formula and localization of seismic waves. *Geophysics*, **58**, 736–740.
- Sheng, P. 1995. *Introduction to wave scattering, localization, and mesoscopic phenomena*. Academic Press.

- Smith, M. L., Sondergeld, C. H., & Norris, J. O. 1991. The Amoco array sonic logger. *The log analyst*, **32**(3), 201–214.
- Snieder, R., Grêt, A., Douma, H., & Scales, J. A. 2002. Coda wave interferometry for estimating nonlinear behavior in seismic velocity. *Science*, **295**, 2253–2255.
- Snieder, R. K. 1986. 3D Linearized scattering of surface waves and a formalism for surface wave holography. *Geophys. J. R. astr. Soc.*, **84**, 581–605.
- Strutt, J. 1885. On waves propagated on the plane surfaces of an elastic solid. *Proc. London Math. Soc.*, **17**, 4–11.
- Taner, M. T., Koehler, F., & Alhilali, K. A. 1974. Estimation and correction of near-surface time anomalies. *Geophysics*, **39**, 441–463.
- Toet, D., Potemski, M., Wang, Y. Y., & Maan, J. C. 1991. Experimental observation of Landau levels in nonperiodic (Fibonacci) superlattices. *Phys. Rev. Lett.*, **66**(2128).
- Turner, J. 1994. *Radiative transfer of ultrasound*. Ph.D. thesis, University of Illinois.
- van Albada, M. P., van Tiggelen, B. A., Lagendijk, A., & Tip, A. 1991. Speed of propagation of classical waves in strongly scattering media. *Phys. Rev. Lett.*, **66**, 3132–3135.
- van Rossum, M. C. W., & Nieuwenhuizen, Th. M. 1999. Multiple scattering of classical waves: microscopy, mesoscopy, and diffusion. *Rev. Mod. Phys.*, **71**(1), 313–371.
- van Wijk, K., Komatitsch, D., Scales, J. A., & Tromp, J. 2003a. *Analysis of strong scattering at the micro-scale*. submitted to J. Acoust. Soc. Am.
- van Wijk, K., Haney, M., & Scales, J. A. 2003b. *Energy propagation in a 1D attenuative medium in the laboratory*. Submitted to Phys. Rev. Lett.
- Viktorov, I. A. D. 1967. *Rayleigh & Lamb waves. Physical theory and application*. New York: Plenum Press.
- Wegler, U., & Lühr, B-G. 2001. Scattering behavior at Merapi volcano (Java) revealed from active seismic experiment. *Geophys. J. Int.*, **145**, 579–592.
- Wiggins, R. A., Larner, K. L., & Wisecup, R. D. 1976. Residual statics analysis as a general linear inverse problem. *Geophysics*, **41**, 922–938.
- Wolfe, J. 1998. *Imaging phonons: acoustic wave propagation in solids*. Cambridge University Press.
- Wu, R. 1985. Multiple scattering and energy transfer of seismic waves—Separation of scattering effect from intrinsic attenuation—I. Theoretical modeling. *Geophys. J. R. astr. Soc.*, **82**, 57–80.

- Wu, R. S., & Aki, K. 1985. Elastic wave scattering by a random medium and the small-scale inhomogeneities in the lithosphere. *J. Geophys. Res.*, **90**(B12), 10261–10273.
- Wu, R. S., & Aki, K. 1988. Multiple scattering and energy transfer of seismic waves—separation of scattering effect from intrinsic attenuation II. Application of the theory to Hindu Kush Region. *Pure and Applied Geophysics*, **128**(1/2).
- Xia, J., Miller, R. D., & Park, C. B. 1999. Estimation of near-surface shear-wave velocity by inversion of Rayleigh waves. *Geophysics*, **64**(3), 691–700.
- Zadler, B., Le Rousseau, J. H. L., Scales, J. A., & Smith, M. L. 2003. *Resonant ultrasound spectroscopy: theory and application*. CWP Project Review and submitted to Geoph. J. Int.

Appendix A

The angle-beam transducer source

To analyze the observations of multiply scattered waves, it is of vital importance to know the characteristics of the source. In this case, a piezo-electric crystal converts a voltage to mechanical energy, causing a compressional wave (P-wave) in a Lucite wedge, to which it is attached (see the left panel of Figure A.1). The transducer wedge has a footprint of 7 cm (in the forward direction) by 4.2 cm and is cut at an angle of 68 degrees, so that the horizontal component of the P-wave in Lucite matches the surface wave velocity in aluminum, causing the source wavelet to be predominantly a surface wave. This surface wave is otherwise known as the Rayleigh wave, named after Lord Rayleigh (J. Strutt) who showed theoretically in Strutt (1885) that waves can propagate over the plane boundary of an elastic half-space over vacuum or a gas like air. These waves have elliptical polarization, comparable to surf in the ocean. Also, their amplitude decays exponentially with depth, where the exponent is inversely proportional to its wavelength. This property of the surface wave is often exploited in near-surface characterization and global Earth seismology (Aki & Richards, 1980), where a spectral analysis assigns material properties according to the depths of penetration of the Rayleigh waves.

A.1 The source on homogeneous aluminum

The right panel of Figure A.1 shows the areas of the three areas of data acquisition. A scan of the surface of the block, where the source is located (so-called *top*), measures the vertical particle velocity of the source wavelet. The scan-area labeled *side*, provides the out-of-plane horizontal component of the source wavelet. Finally, the experiment scanning the *front* of the block, measures the out-of-plane component of the source wavelet. The source wedge is drawn on the edge of the aluminum for all three experiments, for visual purposes. This was only the location of the source, when scanning the side of the block for reasons that will become apparent in the following text. In the other two experiments, the source is away from all sides to exclude side-reflections.

Even though we have the capability to excite energy in the model in a non-contacting matter with a pulsed Nd:YAG laser (Scruby & Drain, 1990), most data are recorded with this 500-kHz Panametrics angle-beam transducer. We chose this source, because the laser source excites predominantly such short wavelengths, that the groove sequence obstructs transmission of significant energy, past a few grooves.

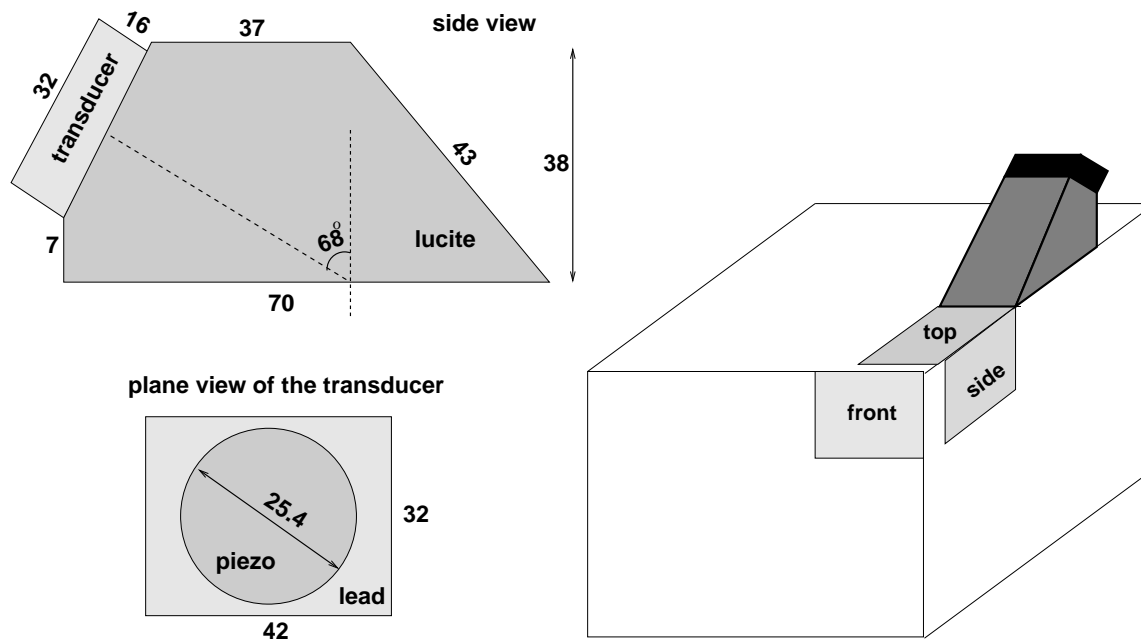


Figure A.1. Dimensions of the source components (left) and the surface areas of the three scans, with respect to the source position on the aluminum model (right).

A.1.1 The vertical component of the source

Figure A.2 is a single trace of the vertical particle velocity of the source, recorded directly in front of the center of the source wedge. It shows that the source wavelet has a Ricker-like character, followed by lower-amplitude, lower-frequency pulses that are caused by ringing of the mechanical source transducer. The right panel of Figure A.2 is its power spectrum, showing that the source spectrum is centered around 400 kHz.

The right panel of Figure A.3 is a snapshot of the entire 2000-mm² area with 3721 receivers on the top of the block. Light colors are high particle velocity of the source wavelet. It shows that across the width of the source wedge, the source wavelet is planar.

A.1.2 The out-of-plane component of the source

Theoretically, Rayleigh waves only have particle motion in the direction of propagation and in the vertical plane. However, placing the source on the edge of the aluminum block, breaks the symmetry and excites an out-of-plane component. The wave field in the right panel of Figure A.4 shows that the source decays rapidly at the surface, and that the wavefront curves at greater depth. From movies made with this data set, it is clear that the curved deeper wavefront is faster than the wavefront at the surface. It is therefore likely that the surface wave source is accompanied by a curved shear wave that is slightly faster, at greater depth.

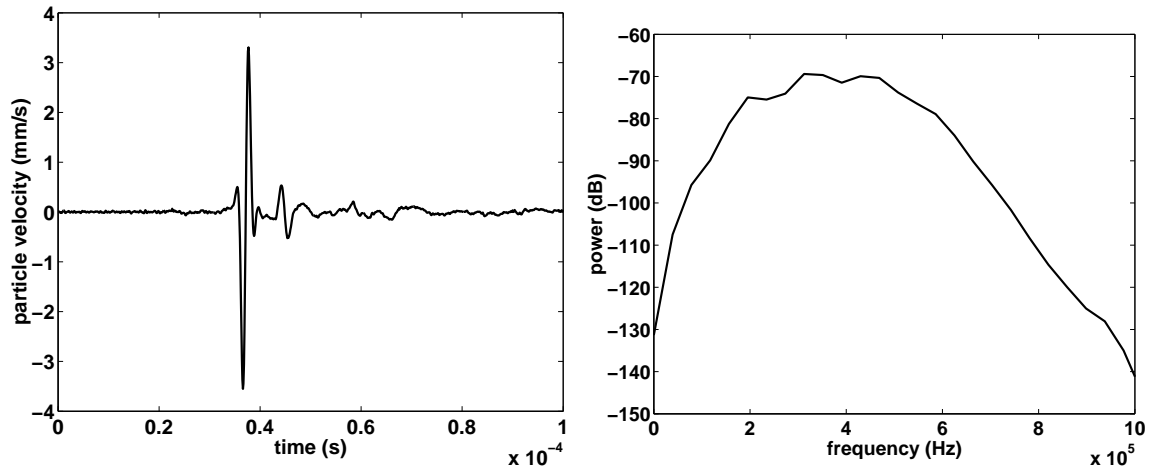


Figure A.2. Vertical component of the source wavelet, measured on the top of the block. The left panel is a single trace in front of the center of the wedge and its power spectrum is plotted on the right.

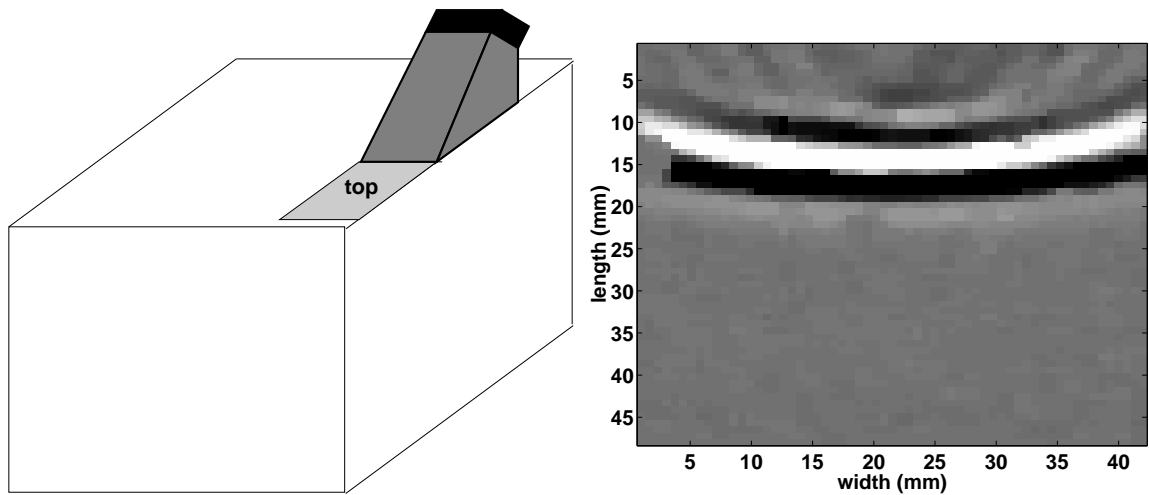


Figure A.3. Left: Experimental configuration to measure the vertical component of the source wavelet across the width of the source wedge. The right panel is a snap-shot of the experiment. Black represents large positive amplitude and white is strong, negative amplitude. The energy between the source and the main energy is ringing of the source.

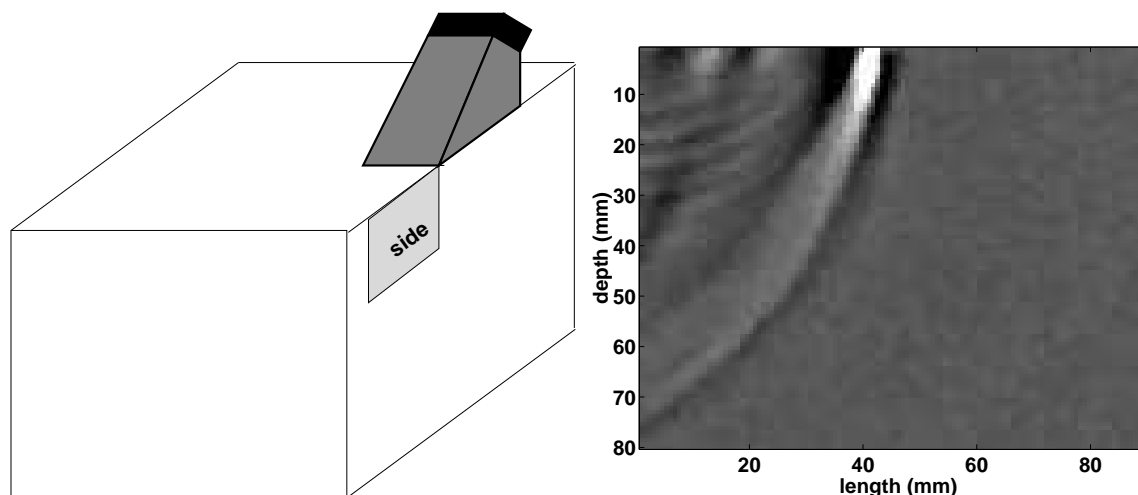


Figure A.4. Left: experimental configuration to measure the source wavelet characteristics as a function of depth. The right panel is a snap-shot of the out-of-plane component measured on the side of the block. Black represents large positive amplitude and white is strong, negative amplitude. The energy between the source and the main energy is ringing of the source.

A.1.3 The in-plane horizontal component of the source

Figure A.5 contains the wave field on the end of the block, from the surface to 65 mm depth, while the source is located 89 mm from the edge. It shows two coherent events: the curved event is the direct surface wave, whereas the linear event is the surface wave, diffracted at the edge of the aluminum block, traveling down the side of the block. The amplitude of the direct wave decays until approximately 15 mm, but is fairly constant deeper in the model. The explanation that the surface wavefront is accompanied by a deeper shear wave (S-wave), is confirmed by the earlier arrival of the deeper part of the source wavelet; at this distance from the source (89 mm), the S-wave component is ahead of the surface wave. Experimentally, this S-wave attached to the Rayleigh-wave front, was observed in photo-elastic measurements by Dally (1978).

A.2 The source on the grooves

For the ensemble measurements in Chapters 3 and 4, the source is positioned on the grooves. This leads to scattering of the source energy under its footprint and a change in coupling between the aluminum and the Lucite wedge. The resulting source wavelet is therefore not the same as on the smooth side of the aluminum. I recorded the wavelet on the smooth side of the aluminum, as well as on the grooved side. On the grooved side of the block, the source is placed on the final 70 mm of grooves, and recorded directly after the

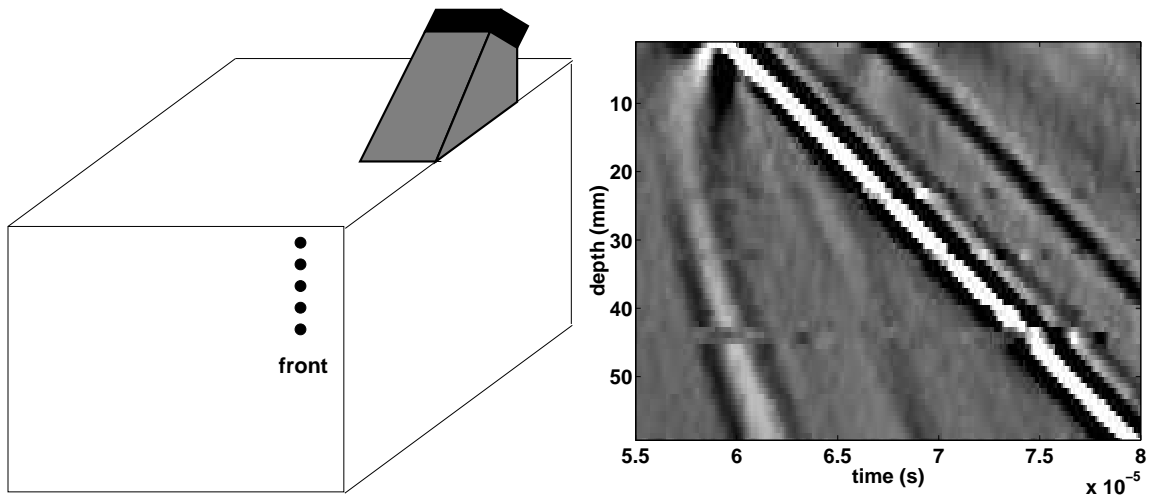


Figure A.5. Left: experimental configuration of the measurement of the in-line horizontal component of the source wavelet, measured on the end of the block, on a line of receivers down the center of the source-wedge. Right: The curved front is the direct arrival of the source wavelet, whereas the linear events are diffractions from the edge, traveling down the block.

last groove, 40 mm from the edge (Figure A.6). This last measurement can only provide a short time-window of the source wavelet on the grooves, because reflected energy off the end of the block re-enters the system. However, when we compare the source wavelet on the grooved side to a 300 kHz low-pass version of the wavelet on the smooth side of the aluminum, we see similarity that is mostly disturbed by the reflection off the back of the block later in the trace (Figure A.7). Therefore, we use the low-pass filtered source wavelet from the smooth side of the aluminum to model the ensemble measurements.

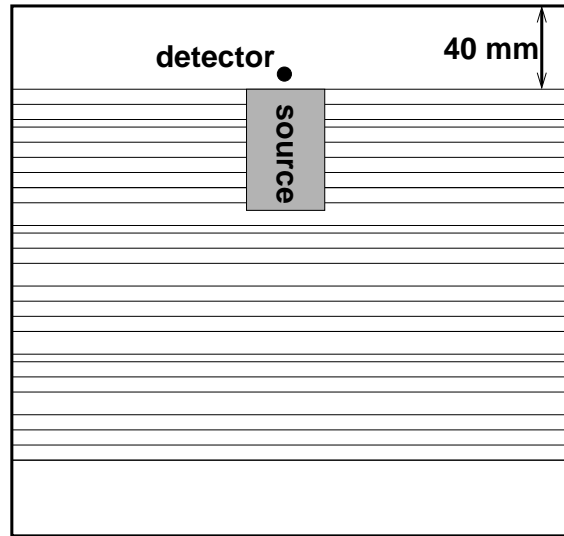


Figure A.6. Top-view of the experimental configuration to record the source wavelet as the source is mounted on the grooves.

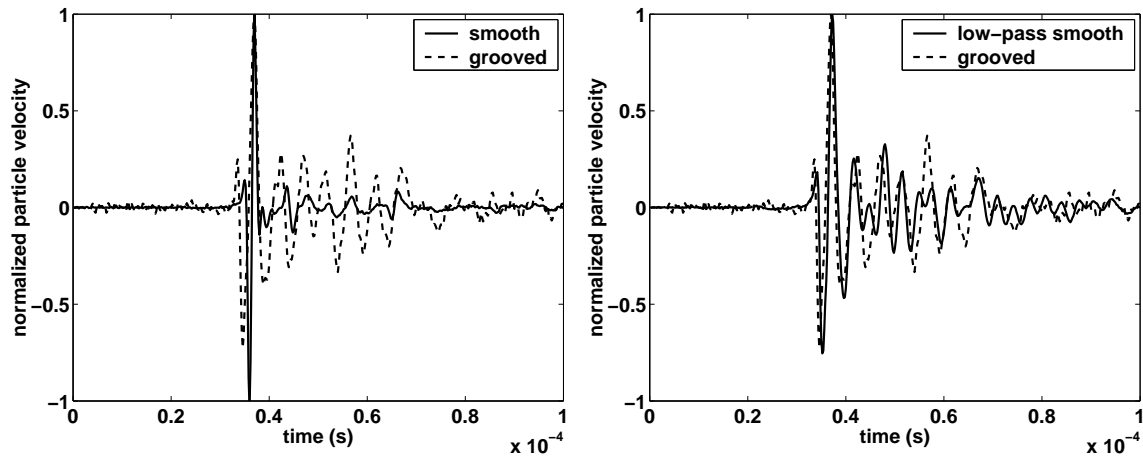


Figure A.7. Left: source wavelets as recorded on the smooth surface and on the grooves, respectively. Right: comparison between the low-pass filtered source wavelet from the smooth surface and the source wavelet recorded on the grooves. The source wavelet on the grooved side has reflections from the end of the block coming in $80/3 \mu\text{s}$ after the initial energy.

Appendix B

Insights in the radiative transfer equation

In the geophysical community, the theory of radiative transfer is relatively novel. This Appendix is an attempt to relate our results in this analysis of energy propagation to more familiar results used in exploration and global seismology.

B.1 The coherent intensity and the O’Doherty-Anstey formula

We derive results from radiative transfer that agree with results from mean field theory, namely the O’Doherty-Anstey formula. Such an equivalence suggests that radiative transfer is a proper extension of mean field theory (a “variance field” theory) for the fluctuating, multiply-scattered waves. In the field of exploration geophysics, a well known result for waves multiply scattered by a 1D layering is that obtained by O’Doherty & Anstey (1971). The O’Doherty-Anstey formula has subsequently been derived from mean field theory (Banik *et al.*, 1985). One outcome of O’Doherty-Anstey is that the amplitude of a wave transmitted through a stack of layers decays exponentially with distance as (Shapiro & Zien, 1993):

$$|T| \sim \exp(-\tilde{R}(k)x), \quad (\text{B.1})$$

where $\tilde{R}(k)$ represents the power spectrum of the average reflection coefficient series normalized by two-way travel distance (Banik *et al.*, 1985). From the solution for the total intensity obtained in the last section, equation (4.23), radiative transfer also predicts an exponential decay for the transmitted, or coherent, wave with distance:

$$|T| \sim \exp(-Bx/2\ell_s), \quad (\text{B.2})$$

where the distance x has replaced vt in equation (4.23) since the δ -function is only non-zero at $x = vt$. The factor of $1/2$ in the exponent of this equation shows up since radiative transfer predicts decay of the transmitted intensity - the square of the true transmission coefficient. We investigate the equivalence of these two theories for the transmission of normally incident waves through assemblages of weak 1D point scatterers (thin beds). The two theories are equivalent if:

$$\tilde{R}(k) = B/2\ell_s. \quad (\text{B.3})$$

Depicted in Figure B.1 is the random medium we will consider: a series of thin layers of varying strength are embedded in a constant velocity background medium. In the parlance of O’Doherty-Anstey, this would be called a “cyclic” sequence. It happens to be the type

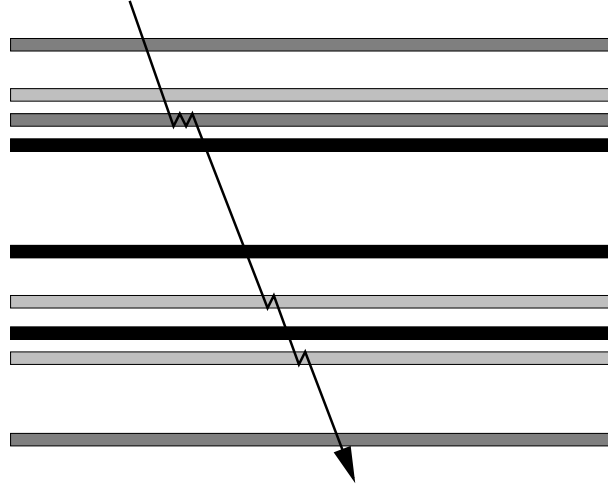


Figure B.1. A wave transmitted through a random sequence of thin beds of varying strength. The thin beds are embedded in a constant background medium.

of medium that radiative transfer, and scattering theory, are geared for. The reflection coefficient series, $RC(x)$, for such a medium would be a series of delta functions of oscillating plus and minus sign:

$$RC(x) = \sum_{j=1}^N R_j [\delta(x - d_j) - \delta(x - h - d_j)], \quad (\text{B.4})$$

where h is the thickness of the beds, R_j and d_j represent the reflection coefficient and location of the j -th bed, respectively, and N is the number of beds.

To calculate $\tilde{R}(k)$, we take the Fourier transform of equation (B.3), square its magnitude to get the power spectrum, and divide by the two-way travel distance:

$$\tilde{R}(k) = 1/2L \left| \int_{-\infty}^{\infty} RC(x) \exp(-i2kx) dx \right|^2. \quad (\text{B.5})$$

Note that the Fourier transform is with respect to $2k$ and not k , similar to a Born inversion formula in 1D (Bleistein *et al.*, 2001). This is evident from standard references in the literature (Banik *et al.*, 1985; Shapiro & Zien, 1993).

Inserting equation (B.4) into equation (B.5) results in

$$\tilde{R}(k) = 1/2L \left| \sum_{j=1}^N R_j \exp(2ikd_j)(1 - \exp(2ikh)) \right|^2. \quad (\text{B.6})$$

For thin layers, $kh \ll 1$ and a first order Taylor series expansion in h leads to $1 - \exp(2ikh) \approx -2ikh$. Pulling it out of the summation yields

$$\tilde{R}(k) = \frac{4k^2h^2}{2L} \left| \sum_{j=1}^N R_j \exp(2ikd_j) \right|^2. \quad (\text{B.7})$$

We now use a standard argument from the theory of multiple scattering: if d_j , the spacing of the thin beds, is a random variable, the cross terms in the square of the summation in equation (B.7) cancel in the *average* and the squaring can be brought inside the summation:

$$\tilde{R}(k) = \frac{2k^2h^2}{L} \sum_{j=1}^N |R_j \exp(2ikd_j)|^2. \quad (\text{B.8})$$

Now, inside the summation, the exponential does not contribute to the magnitude and we are left with

$$\tilde{R}(k) = \frac{1}{2L} 4k^2h^2 \sum_{j=1}^N |R_j|^2 = \frac{1}{L} 2k^2h^2 N \langle |R_j|^2 \rangle, \quad (\text{B.9})$$

where $\langle |R_j|^2 \rangle$ is the mean-square of the interface reflection coefficients.

Returning to equation (B.3), to prove that radiative transfer and the O'Doherty-Anstey formula predict the same exponential decay for the transmitted wave, we set equation (B.9) to:

$$\frac{B}{2\ell_s} = \frac{1}{L} 2k^2h^2 N \langle |R_j|^2 \rangle. \quad (\text{B.10})$$

For (Rayleigh) point scatterers in 1D, the radiation is isotropic. Hence, $B = 0.5$. Rearranging equation (B.10):

$$\ell_s = \frac{1}{8k^2h^2 \langle |R_j|^2 \rangle \frac{N}{L}}. \quad (\text{B.11})$$

The quantity N/L is simply the number density of the thin beds, ρ . In the limit of weak scatterers (such that $R_j \ll 1$) $8k^2h^2 \langle |R_j|^2 \rangle = \sigma_s$, the scattering cross section (see Section B.2). The presence of weak reflection coefficients is an underlying assumption in the O'Doherty-Anstey result (Banik *et al.*, 1985), so that equation (B.11) can now be rewritten in a familiar form:

$$\ell_s = \frac{1}{\rho\sigma_s}. \quad (\text{B.12})$$

This is recognized as equation (4.4), the independent scattering approximation. Equation (B.12) demonstrates that, for this model, the exponential decay of the transmitted wave from O'Doherty-Anstey, or mean-field theory, is equivalent to that predicted by radiative transfer. A conceptual diagram of this equivalence is shown in Figure B.2. From mean field theory, both the phase and the amplitude of the transmitted wave can be obtained; however, the incoherent energy, for which the mean is zero, falls out. Similarly, 1D radiative transfer can address the amplitude of the transmitted wave and the behavior of

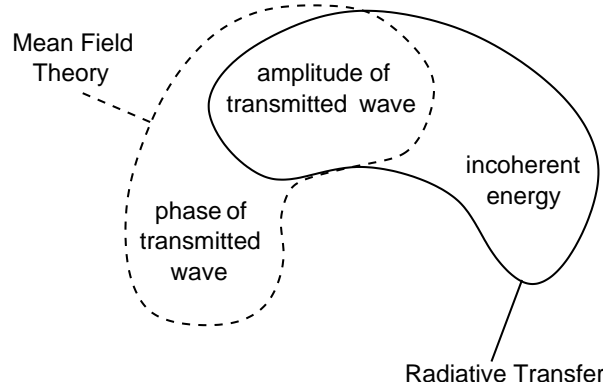


Figure B.2. A diagram representing the overlap of mean field theory and radiative transfer for the amplitude of the transmitted wave through a medium like that depicted in Figure B.1.

the incoherent intensity, but phase information is lost. Both theories agree in their region of overlap, as demonstrated by the case of random layering we considered here.

Previously, we stated that for expression 4.4 to hold, the scatterers (thin beds) had to be separated by at least a wavelength. Hence, in this model, no reflections from below the recording depth interfere with the transmitted wave. All the interference resulting in the exponential decay of the direct wave originates from peg-leg multiples within the thin beds, not between them (Figure B.1).

B.2 The scattering cross-section in the limit of weak scattering

The scattering cross section for a thin bed is (Sheng, 1995, equation (P3.54)):

$$\sigma_s(k) = \frac{1}{2}k^2h^2 \left[1 - \left(\frac{c}{c_0} \right)^2 \right]^2, \quad (\text{B.13})$$

where k is the wavenumber, h is the thickness of the thin bed, c is the velocity of the thin bed, and c_0 is the velocity of the background medium. The k^2 dependence of σ_s is the hallmark of Rayleigh scattering in 1D. Equation (B.13) is the first term of a power series in kh and can be derived from the 1D scalar wave equation by requiring that the displacement and its spatial derivative be continuous at both boundaries of a 1D scatterer, or thin bed. These same boundary conditions at an interface yield the reflection and transmission coefficients:

$$R = \frac{c - c_0}{c + c_0} \quad \text{and} \quad T = \frac{2c}{c + c_0}. \quad (\text{B.14})$$

Assume that the velocity of the thin bed can be expressed as $c = c_0(1 + \alpha)$ with α

a small parameter. This is the case of a small reflection coefficient. For an assemblage of thin beds with varying velocities, α represents the RMS perturbation from the background velocity. Substituting this relation for c into equation (B.13):

$$\sigma_s(k) = \frac{1}{2}k^2h^2(1 - (1 + \alpha)^2)^2. \quad (\text{B.15})$$

Keeping the lowest order term in α :

$$\sigma_s(k) \approx 2k^2h^2\alpha^2. \quad (\text{B.16})$$

To satisfy equation (B.3), we need to show that the scattering cross section in the weak scattering limit, equation (B.16), is equal to $8k^2h^2R^2$. From equation (B.14), we know that

$$8k^2h^2R^2 = 8k^2h^2 \left(\frac{c - c_0}{c + c_0} \right)^2. \quad (\text{B.17})$$

Substituting $c = c_0(1 + \alpha)$ into equation (B.17) gives

$$8k^2h^2R^2 = 8k^2h^2 \left(\frac{\alpha}{2 + \alpha} \right)^2. \quad (\text{B.18})$$

Again, keeping the lowest order term in α , we obtain that the right-hand side of equation (B.18) equals $2k^2h^2\alpha^2$, identical to equation (B.16). Hence, in the weak scattering limit for thin beds, $8k^2h^2R^2 = \sigma_s$.

B.3 The Green's function for the directional intensity

Expressions (4.10) and (4.11) show that the 1D radiative transfer equation can be split into a system of PDEs in terms of the left and right-going intensities. So far, only the reduced PDE governing the total intensity has been studied. This is due to the fact that measuring either the left or right-going intensity entails splitting the wave field into left and right-going waves. Such a decomposition requires dense spatial sampling to perform the type of filtering routinely done in Vertical Seismic Profiling: separating up from down-going waves. Here, we show that knowledge of the individual left and right-going energies can give us more detailed insight into the incoherent energy.

Assuming that the wave field has been decomposed into left and right-going waves, we now solve the system of 2 partial differential equations that comprise the full radiative transfer equation. To begin, we write equations (4.10) and (4.11) in matrix form:

$$\frac{\partial \mathbf{I}}{\partial t} + M \frac{\partial \mathbf{I}}{\partial x} = N \mathbf{I} + \mathbf{S}, \quad (\text{B.19})$$

where \mathbf{I} , M , N , and \mathbf{S} are:

$$\begin{aligned}\mathbf{I} &= \begin{bmatrix} I_r \\ I_l \end{bmatrix}, M = \begin{bmatrix} v & 0 \\ 0 & -v \end{bmatrix}, \\ N &= \begin{bmatrix} -\frac{B}{\tau_s} - \frac{1}{\tau_a} & \frac{B}{\tau_s} \\ \frac{B}{\tau_s} & -\frac{B}{\tau_s} - \frac{1}{\tau_a} \end{bmatrix}, \\ \mathbf{S} &= \begin{bmatrix} S_r \\ S_l \end{bmatrix}.\end{aligned}\quad (\text{B.20})$$

There exists no general theory for solving systems of PDEs as there is for systems of ODEs. Hence, we proceed by Fourier transforming equation (B.19) over space, solving the system of ODEs, and inverse Fourier transforming back to spatial coordinates. With the Fourier conventions:

$$\mathbf{I}(x) = \int_{-\infty}^{\infty} \tilde{I}(k) \exp(-ikx) dk \tilde{I}(k) = \frac{1}{2\pi} \int_{-\infty}^{\infty} \mathbf{I}(x) \exp(ikx) dx, \quad (\text{B.21})$$

equation (B.19) becomes a system of 2 ODEs:

$$\frac{\partial \tilde{I}}{\partial t} = (N + ikM)\tilde{I} + \tilde{S}. \quad (\text{B.22})$$

For the source function, we again take a general directional point source with right and left-going components S_r and S_l . Allowing the parameter c to govern the directivity of the source as we did previously, the source vector is:

$$\mathbf{S} = \begin{bmatrix} 1+c \\ 1-c \end{bmatrix} \frac{\delta(x)\delta(t)}{2}. \quad (\text{B.23})$$

The solution of the system of ODEs follows that given in standard texts on differential equations (Boyce & DiPrima, 1997). Here we give the solution in the k -domain:

$$\begin{aligned}I_r(k, t) &= \frac{1}{4\pi} \exp(-Bvt/\ell_s) \exp(-vt/\ell_a) \left((1-c)\frac{B}{\tau_s} + i(1+c)kv \right) \times \\ &\sinh \left(t\sqrt{\frac{B^2}{\tau_s^2} - k^2v^2} \right) \left(\frac{B^2}{\tau_s^2} - k^2v^2 \right)^{-1/2} + (1+c) \cosh \left(t\sqrt{\frac{B^2}{\tau_s^2} - k^2v^2} \right).\end{aligned}\quad (\text{B.24})$$

$$\begin{aligned}I_l(k, t) &= \frac{1}{4\pi} \exp(-Bvt/\ell_s) \exp(-vt/\ell_a) l \left((1+c)\frac{B}{\tau_s} - i(1-c)kv \right) \times \\ &\sinh \left(t\sqrt{\frac{B^2}{\tau_s^2} - k^2v^2} \right) \left(\frac{B^2}{\tau_s^2} - k^2v^2 \right)^{-1/2} + (1-c) \cosh \left(t\sqrt{\frac{B^2}{\tau_s^2} - k^2v^2} \right).\end{aligned}\quad (\text{B.25})$$

To get the directional intensities in the spatial domain, we must inverse Fourier transform equations (B.24) and (B.25). Two identities are needed for this inversion:

$$ix \int_{-\infty}^{\infty} \tilde{I}(k) \exp(-ikx) dk = \int_{-\infty}^{\infty} \frac{\partial \tilde{I}(k)}{\partial k} \exp(-ikx) dk, \quad (\text{B.26})$$

and from the theory of Bessel functions (Hemmer, 1961):

$$\int_{-\infty}^{\infty} \cos(kx) \frac{\sin\left(t\sqrt{k^2v^2 - \frac{B^2}{\tau_s^2}}\right)}{\sqrt{k^2v^2 - \frac{B^2}{\tau_s^2}}} dk = \frac{\pi}{v} I_0 \left[\frac{B}{\ell_s} \sqrt{v^2t^2 - x^2} \right] u(vt - |x|). \quad (\text{B.27})$$

After inverting the Fourier transform, we obtain for the right-going intensity:

$$\begin{aligned} I_r(x, t) = & \frac{1}{4} \exp(-Bvt/\ell_s) \exp(-vt/\ell_a) \left[2(1+c)\delta(vt-x) + \frac{B}{\ell_s} u(vt-|x|) \times \right. \\ & \left[(1-c)I_0\left(\frac{B}{\ell_s}\sqrt{v^2t^2-x^2}\right) + \right. \\ & \left. \left. (1+c)\sqrt{\frac{vt+x}{vt-x}} I_1\left(\frac{B}{\ell_s}\sqrt{v^2t^2-x^2}\right) \right] \right], \end{aligned} \quad (\text{B.28})$$

and for the left-going intensity:

$$\begin{aligned} I_l(x, t) = & \frac{1}{4} \exp(-Bvt/\ell_s) \exp(-vt/\ell_a) \left[2(1-c)\delta(vt+x) + \frac{B}{\ell_s} u(vt-|x|) \times \right. \\ & \left[(1+c)I_0\left(\frac{B}{\ell_s}\sqrt{v^2t^2-x^2}\right) + \right. \\ & \left. \left. (1-c)\sqrt{\frac{vt-x}{vt+x}} I_1\left(\frac{B}{\ell_s}\sqrt{v^2t^2-x^2}\right) \right] \right], \end{aligned} \quad (\text{B.29})$$

These equations for the two intensities show that the two Bessel functions that make up the incoherent intensity are sensitive to different aspects of the source radiation pattern. For instance, if the source were unidirectional, $c = -1$ or $c = 1$ and the zero order Bessel function would come from one direction and the first order Bessel from the other. It can also be verified that adding equations (B.28) and (B.29) gives the total intensity, equation (4.23). In the absence of phase information, perhaps the directional intensities can yield important information about spatial variations in the material properties.

B.4 The diffusion approximation in infinite 1D media

At late times, we demonstrate that radiative transfer can be simplified even further by approximating its behavior as the solution to a diffusion equation. Results of finite-difference

simulations of the 1D wave equation with random scatterers (Haney *et al.*, 2003) support the accuracy of this approximation. Using correct values for the parameters needed to describe the scattering, the average intensity of the numerical simulations is seen to approach the diffusive limit with time.

In addition to the coherent intensity, physical insight can be gained on the incoherent part of the total intensity. The general expression for the Green's function for radiative transfer in 1D, equation (4.23), shows that for late times the coherent term is zero and the incoherent field, defined by a combination of Bessel functions, approximates the solution to the diffusion equation (Ishimaru, 1997). Especially in optics, where it is hard to obtain phase information, inferences on the statistical properties of the medium are often based on this late-time diffusive behavior (Boas *et al.*, 1995). In elastic wave-scattering, the incoherent field is used to decipher the different mechanisms of attenuation (Margerin *et al.*, 1999).

To derive the diffusion approximation from equation (4.23), all we need is that $vt \gg x$. Noting that the zeroth and first modified Bessel functions have the asymptotic forms:

$$I_0(z) \approx I_1(z) \approx (2\pi z)^{-\frac{1}{2}} \exp(z) \quad \text{for } z \gg 1, \quad (\text{B.30})$$

we can write equation (4.23) in the late-time limit as:

$$I_t(x, t) = \frac{B}{\ell_s} \exp(-Bvt/\ell_s - vt/\ell_a) \exp\left(\frac{B}{\ell_s} \sqrt{v^2 t^2 - x^2}\right) \left(2\pi \frac{B}{\ell_s} \sqrt{v^2 t^2 - x^2}\right)^{-1/2}. \quad (\text{B.31})$$

In this expression, the delta functions from equation (4.23) have fallen out. Organizing terms in equation (B.31), expanding the square root in the exponential as a Taylor series in the small parameter x/vt , and keeping the lowest order in x/vt , we get:

$$I_t(x, t) = \exp(-Bvt/\ell_s - vt/\ell_a) \exp\left(\frac{Bvt}{\ell_s} \left(1 - \frac{1}{2}(x/vt)^2\right)\right) \left(2\pi \frac{\ell_s}{B} vt\right)^{-1/2}. \quad (\text{B.32})$$

Two of the exponentials cancel in equation (B.32) and, after isolating the term $\ell_s/2B$, the late-time limit of the radiative transfer equation can finally be written as

$$I_t(x, t) = \exp\left(-\frac{x^2}{4\left(\frac{\ell_s}{2B}\right)vt} - \frac{vt}{\ell_a}\right) \left(4\pi \left(\frac{\ell_s}{2B}\right)vt\right)^{-1/2}. \quad (\text{B.33})$$

In the case of no attenuation ($\ell_a \rightarrow \infty$), equation (B.33) can be identified as the Green's function for the 1D diffusion equation with the diffusion constant $D = (\ell_s/2B)v$ (see equation (B.52)). This implies that the movement of energy at late times has an effective mean free path different from ℓ_s or ℓ^* . This effective mean free path is called the *transport* mean free path, $\ell_{tr} = \ell_s/2B$. In 1D, $\ell_{tr} = \frac{1}{2}\ell^*$, since $\ell^* = \ell_s/B$. Note that the transport mean free path can be determined from the extinction mean free path without knowledge of the underlying details of the scattering.

It is common to relate ℓ_{tr} to ℓ_s via:

$$\ell_{tr} = \frac{\ell_s}{1 - \langle \cos\theta \rangle}, \quad (\text{B.34})$$

where $\langle \cos\theta \rangle$ represents the average scattered energy in all directions weighted by the cosine of that direction. For isotropic scattering, $\langle \cos\theta \rangle = 0$ and the two mean free paths are identical. However, using the general relation $\langle \cos\theta \rangle = F - B$ (Hendrich *et al.*, 1994) and the fact that $F + B = 1$, equation (B.34) can be rewritten as

$$\ell_{tr} = \frac{\ell_s}{1 - F + B} = \frac{\ell_s}{2B}, \quad (\text{B.35})$$

which is exactly the relationship we have derived from the diffusion approximation.

B.5 The diffusion approximation in finite 1D media

The above derivation of the diffusion approximation showed how the solution of the radiative transfer equation approaches that of the diffusion equation at late times. In this section, we prove that the underlying governing equation for the total intensity at late times also becomes the diffusion equation. While the radiative transfer equation cannot be analytically solved for in a finite geometry, its late time equivalent – the diffusion equation – can be solved with boundary conditions.

Neglecting absorption ($\ell_a \rightarrow \infty$), we can rearrange equation (4.13) as

$$\frac{\partial I_n}{\partial t} + \frac{2B}{\tau_s} I_n = -v \frac{\partial I_t}{\partial x}. \quad (\text{B.36})$$

In the diffusive regime, we assume that (Morse & Feshbach, 1953):

$$\frac{2B}{\tau_s} I_n \gg \frac{\partial I_n}{\partial t}, \quad (\text{B.37})$$

meaning that the time rate of change of the right and left-going intensities is relatively small. Under this condition, equation (B.36) becomes

$$\frac{2B}{\tau_s} I_n = -v \frac{\partial I_t}{\partial x}. \quad (\text{B.38})$$

Substituting equation (B.38) into equation (4.12) for I_n yields

$$\frac{\partial I_t}{\partial t} + v \frac{\partial}{\partial x} \left[-\frac{\tau_s v}{2B} \frac{\partial I_t}{\partial x} \right] = 0. \quad (\text{B.39})$$

Under the assumption that v and τ_s do not depend on position, equation (B.39) takes the

form:

$$\frac{\partial I_t}{\partial t} = v \left(\frac{\ell_s}{2B} \right) \frac{\partial^2 I_t}{\partial x^2}, \quad (\text{B.40})$$

which we recognize as the 1D diffusion equation with the same diffusion constant $D = v(\ell_s/2B) = v\ell_{tr}$ we obtained in the previous section.

Now assume there is a boundary at $x = 0$ where scattering occurs to the right (positive values of x), but not to the left (negative values of x). Then, at $x = 0$, there is no intensity coming *into* the scattering region, i.e. the right-going intensity is zero. We can express the right-going intensity as the sum of the total intensity and the net right-going intensity (flux) and set it to zero at $x = 0$:

$$I_r = \frac{1}{2}I_t + \frac{1}{2}I_n = 0 \quad \text{at } x = 0. \quad (\text{B.41})$$

Using the approximation we derived in equation (B.38), the I_n -term can be replaced by a spatial derivative of I_t :

$$\frac{1}{2}I_t + \frac{1}{2} \left(-\frac{\ell_s}{2B} \frac{\partial I_t}{\partial x} \right) = 0. \quad (\text{B.42})$$

From this equation, we learn that

$$I_t = \frac{\ell_s}{2B} \frac{\partial I_t}{\partial x} = \ell_{tr} \frac{\partial I_t}{\partial x}. \quad (\text{B.43})$$

The solution to equation (B.43) states that, near $x = 0$, I_t has the form:

$$I_t \sim x + \ell_{tr}. \quad (\text{B.44})$$

Extrapolating away from the boundary according to equation (B.44), $I_t = 0$ at $x = -\ell_{tr}$. Hence, the presence of a boundary that radiates energy out of a finite scattering region can be approximated by a Dirichlet boundary condition a distance ℓ_{tr} *outside* the scattering region. Suppose there is a region of length L extending from $x = 0$ to $x = L$. Then, at late times, the Green's function for the total intensity should obey the boundary value problem:

$$\begin{aligned} \frac{\partial I_t}{\partial t} &= D \frac{\partial^2 I_t}{\partial x^2} + \delta(x - x')\delta(t) \\ I_t &= 0 \quad \text{at } x = -\ell_{tr} \text{ and } x = \ell_{tr} + L. \end{aligned} \quad (\text{B.45})$$

where $D = v\ell_{tr}$. In 1D, this PDE can be solved by expanding over the modes of the Laplacian:

$$I_t(x, x', t) = \sum_{m=1}^{\infty} \exp\left(-\frac{m^2\pi^2 Dt}{(L + 2\ell_{tr})^2}\right) \sin\left(\frac{m\pi(x + \ell_{tr})}{L + 2\ell_{tr}}\right) \sin\left(\frac{m\pi(x' + \ell_{tr})}{L + 2\ell_{tr}}\right). \quad (\text{B.46})$$

The PDE could have equivalently been solved by the method of images.

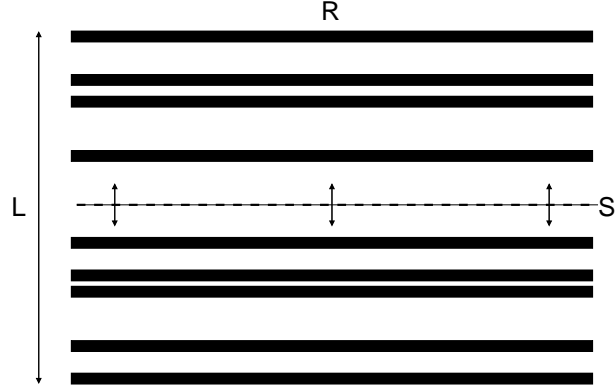


Figure B.3. The geometry of the 1D numerical scattering experiments. The source was at the center of a region with thin random layers and a receiver was positioned above the layers for each experiment. The size L of the scattering region varied between experiments with the values 80 m, 120 m, 160 m, 200 m, and 240 m.

B.6 Green's function for diffusion in an infinite 1D medium

To find the Green's function, I solve the 1D diffusion equation with attenuation using a delta function source:

$$\frac{\partial I}{\partial t} - D \frac{\partial^2 I}{\partial x^2} + D\kappa^2 I = \delta(x)\delta(t), \quad (\text{B.47})$$

where D is the diffusion constant, $\delta(x)\delta(t)$ the source term, and κ an absorption coefficient, caused by diffraction from the bottom of the grooves. In the (ω, k) domain, it follows that:

$$I(\omega, k) = \frac{1}{D(k^2 + \kappa^2) - i\omega}, \quad (\text{B.48})$$

so the intensity as a function of space and time is

$$\begin{aligned} I(t, x) &= \frac{1}{(2\pi)^2} \int_{-\infty}^{\infty} \int_{-\infty}^{\infty} \frac{\exp(-ikx) \exp(-i\omega t) dk d\omega}{D(k^2 + \kappa^2) - i\omega} \\ &= \exp\left(-\frac{x^2}{4Dt} - D\kappa^2 t\right) (4\pi Dt)^{-1/2}. \end{aligned} \quad (\text{B.49})$$

We first integrate over frequency:

$$\int_{-\infty}^{\infty} \frac{\exp(-i\omega t)}{\alpha - i\omega} d\omega = 2\pi \exp(-\alpha t), \quad (\text{B.50})$$

after integration in the complex plane. Note that $\alpha = D(k^2 + \kappa^2)$. So now we are left with

$$\int_{-\infty}^{\infty} \exp(-ikx - Dk^2t) = \sqrt{\frac{\pi}{Dt}} \exp\left(-\frac{x^2}{4Dt}\right). \quad (\text{B.51})$$

Factoring in all the constants, gives us the Green's function for 1D diffusion with absorption:

$$I(x, t) = \exp\left(-\frac{x^2}{4Dt} - D\kappa^2t\right) (4\pi Dt)^{-1/2}. \quad (\text{B.52})$$

This is the same result as obtained by making the late-time assumption in the radiative transfer equation in equation (B.33).

Appendix C

Wave speeds in scattering media

When considering wave propagation in a scattering medium, we can define the phase, group and energy (or transport) velocity, but how do these relate to the speeds of the coherent and incoherent signal from ensemble measurements? Factors are the size (van Albada *et al.*, 1991) and density (Cowan *et al.*, 1998) of the scatterers, compared to the wavelength of the signal, for instance. Here we try to unravel the different speeds, to avoid mistakes in modeling observations in the lab.

In the radiative transfer equation, there is a single velocity parameter. This is generally called the energy or transport velocity. Is it:

1. the group velocity,
2. the move-out of the envelope of the wave field with increasing source-detector offset,
or
3. the move-out of the coherent signal with increasing source-detector offset?

Note that the last two are only different in the sense that the coherent signal is the ensemble average of 2.

C.1 Group velocity

By definition, the group velocity is

$$v_g = \frac{d\omega(k)}{dk}. \quad (\text{C.1})$$

There is an obvious relation between the group and the phase velocity c :

$$v_g = k \frac{dc}{dk} + c(k), \quad (\text{C.2})$$

from which it can be determined what we already knew: in the absence of dispersion (c is frequency independent), the group velocity *is* the phase velocity. Note also, that for negative dispersion, the group velocity can be greater than the phase velocity.

The velocity of the energy package can be described by following the envelope of the trace as it moves out with increasing source-detector offset. In seismology, it is common practice to determine the group velocity in this manner. More detailed information about

the seismic velocities can be obtained by band-pass filtering the seismic trace. This gives direct information on $c(k)$ and thus indirectly on $v_g(k)$. This envelope velocity has also been called the incoherent or the diffusive velocity, but it has been shown that for resonant scatterers the observed envelope velocity is significantly lower than the incoherent velocity (Kuga *et al.*, 1993).

C.2 Coherent velocity

To estimate the coherent signal in a scattering media, we need to acquire an ensemble measurement. For instance, we ping a fish bowl with sound-scattering fish swimming around (De Rosny & Roux, 2001) or measure the wave field for different locations of a fixed source-receiver distance (Scales & van Wijk, 2001). The coherent signal is the square of the mean trace in the ensemble. With ensemble measurements at different source-detector separations, a regression on the coherent signal determines the coherent velocity v_c .

There is a obvious link between the coherent and the group or envelope velocity. The coherent velocity is speed of the envelope of an ensemble averaged intensity. Scattered energy later in the traces is averaged out. This means that the peak of the envelope of the coherent signal cannot arrive later than the peak of the envelopes of the individual traces, as we used to determine the group velocity. Conversely, if the scattered energy is strong, the peak of the envelope of a single measurement can be shifted in time, slowing the group velocity. A prime example of this effect is in the case of resonant scattering; energy is being slowed by resonance of the scatterers (van Albada *et al.*, 1991).

C.3 Observations

Figure C.1 contains the picks of an individual phase and that of peaks of the envelope of the surface-wave field in Figure 3.7. The straight lines are the regressions with slopes $c = 2800 \pm 14$ m/s and $v_g = 1488 \pm 54$ m/s. The phase velocity c in the scattering medium is less than the velocity on the smooth side of the aluminum model: $c_{al} = 2870 \pm 5$ m/s. This is caused by scatterings between the grooves, destructively interfering with the coherent wave, like in the case of thin-bed multiples (O’Doherty & Anstey, 1971). Note that editing the picks of the envelopes for late times, increases the group velocity to $v_g = 1855 \pm 35$ m/s. Throwing away the outliers for large times is validated by the much lower signal-to-noise ratio, and by the possible loss of coherency for such large source-detector offsets.

The velocity of the coherent signal was calculated from ensemble measurements at 6 source-detector offsets (Figure C.2): $v_c = 1818 \pm 123$ m/s. This is in agreement with the group velocity within one standard deviation for the picks up to 0.085 ms. Theory supports that in the Rayleigh scattering regime, the group velocity (incoherent velocity) is equal to the coherent velocity (Figures 2 and 3 in Kuga *et al.*, 1993). Physically, this means that the coherent signal is strong enough, for the source-detector offsets measured, that scattering does not change the location of the coherent peak.

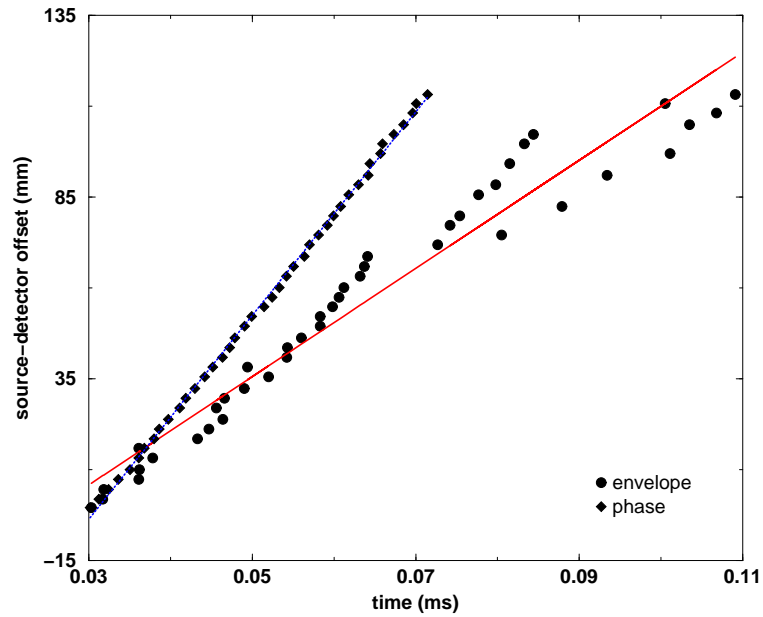


Figure C.1. Picks for a single phase and for the peak of the envelope of each surface-wave field. The straight lines are their respective regressions.

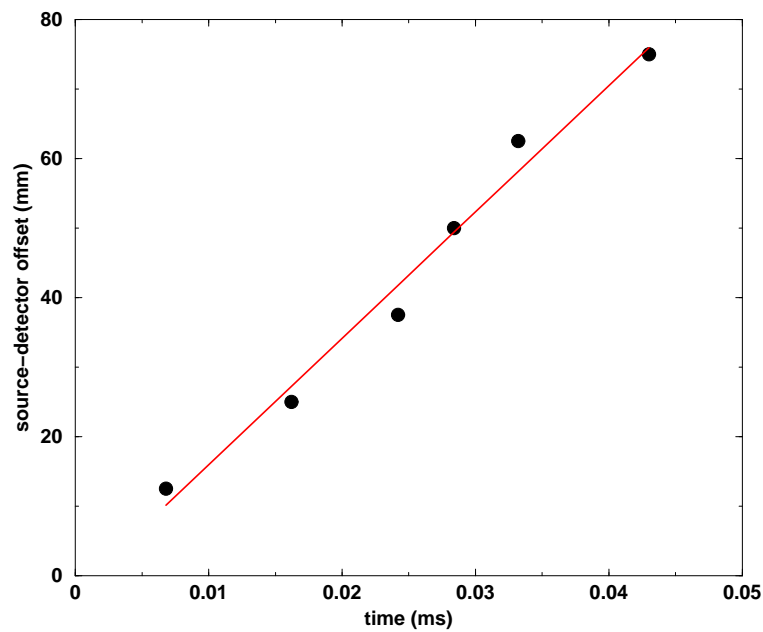


Figure C.2. Regression on the move-out of the peak of the coherent energy. The regression estimates $v_e = 1818 \pm 123$ m/s.

C.4 Phase velocity of the ensemble-averaged trace

Regression on the 6 ensemble-averaged traces, leads to an *average* phase velocity of 2766 ± 60 m/s. This is in agreement with the phase velocity recorded for a single realization (Figure C.1).

C.5 Conclusions

The energy velocity is either the velocity of the coherent signal (for non-resonant scattering) or the velocity of the envelope of the trace, i.e. the group velocity (for resonant scattering). In the case on non-resonant (Rayleigh) scattering, the group velocity is the same as the coherent velocity. Since we have many grooves per wavelength, we are in the Rayleigh scattering regime and the energy velocity is the group velocity is the coherent velocity: $v \approx 1825$ m/s. It should be noted that in the Mie scattering regime, the radiative transfer equation with a single energy velocity is not a good candidate to describe energy propagation, because when scattering is resonant, the coherent signal travels faster than the incoherent energy.

Appendix D

scattering attenuation and absorption in sonic logging

Intrinsic absorption in geophysical data is of great interest to the geophysical community, because it is generally considered a direct fluid indicator. However, geophysical data is attenuated by absorption *and* scattering (Scales & van Wijk, 1999). Unraveling this combination of parameters is not easy, but radiative transfer models suggest opportunities to accomplish just that. In a full-waveform sonic log, the radiative transfer model (van Wijk *et al.*, 2003b) leads to estimates of scattering attenuation and absorption, separately. This study is done on a data set of unknown location, just to show the feasibility of the method. Tying the results to geology is left to future studies.

D.1 Observations

The sonic tool has a pressure source and 8 hydrophones at 8-inch spacing (Smith *et al.*, 1991). There are 100 shot locations, 3 inches apart. Figure D.2 shows one common-shot (left) and one common-receiver record (right). On the common-shot record one can identify, from early times to late:

1. the trigger (no move-out),
2. the P-wave propagating at 4373 m/s,
3. the S-wave propagating at 2133 m/s, shortly followed by
4. the Stoneley wave, and
5. multiples between these coherent events and after the Stoneley wave.

The (multiples of) Stoneley waves can also be viewed as some normal modes of the bore-hole, or they can be treated as waves bouncing around in the vertical direction. Either way, they sample a mix of the content of the bore-hole and surrounding medium (Figure D.1).

D.2 Radiative transfer

The ensemble average of the intensities satisfies the model of radiative transfer. With only one realization of the medium at hands (Earth), we assume ergodicity in the geology and treat the stack of common-receiver sections as our ensemble average: the total intensity

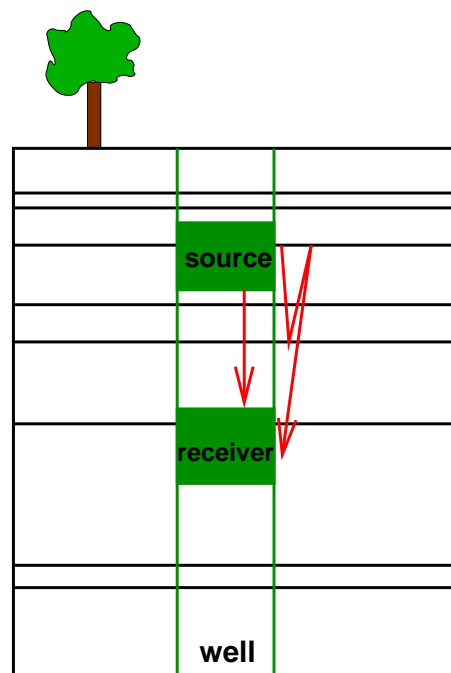


Figure D.1. Possible origin of the coda. The rays are drawn at non-zero incidence, for visual purposes: we assume that multiples are in the vertical plane only, bouncing between layers near the borehole wall.

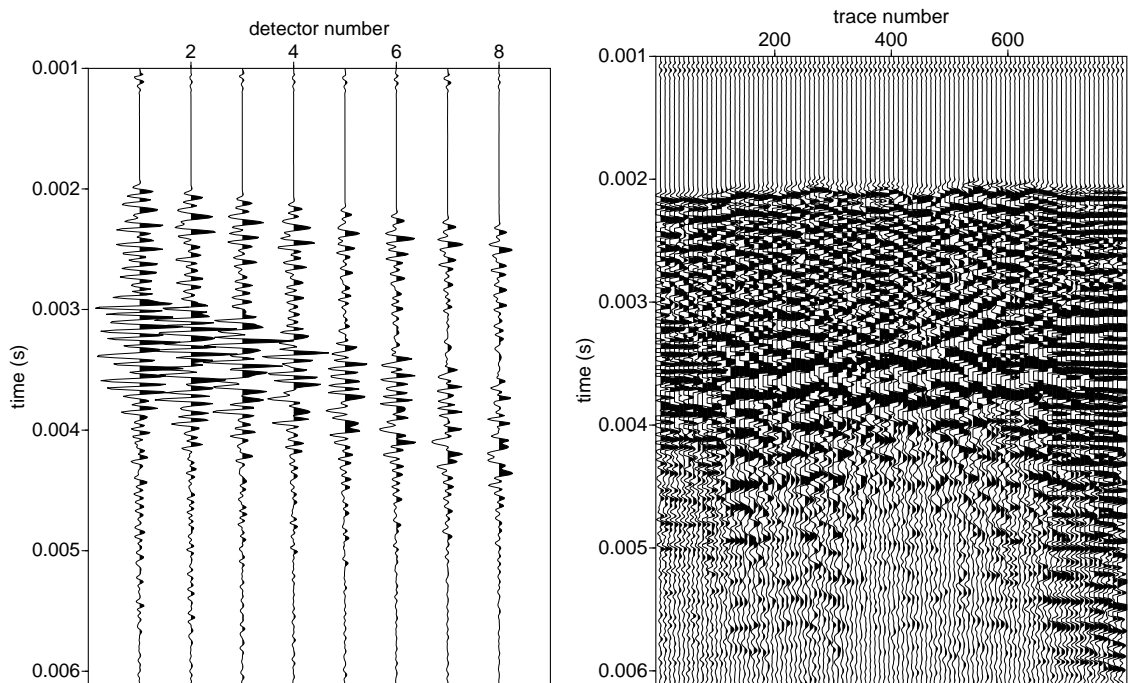


Figure D.2. Slices of the data volume. The left plot is a common-shot record and the right is a common-receiver record. Note that the recorded energy at 0.006 s is still significantly above the background noise level.

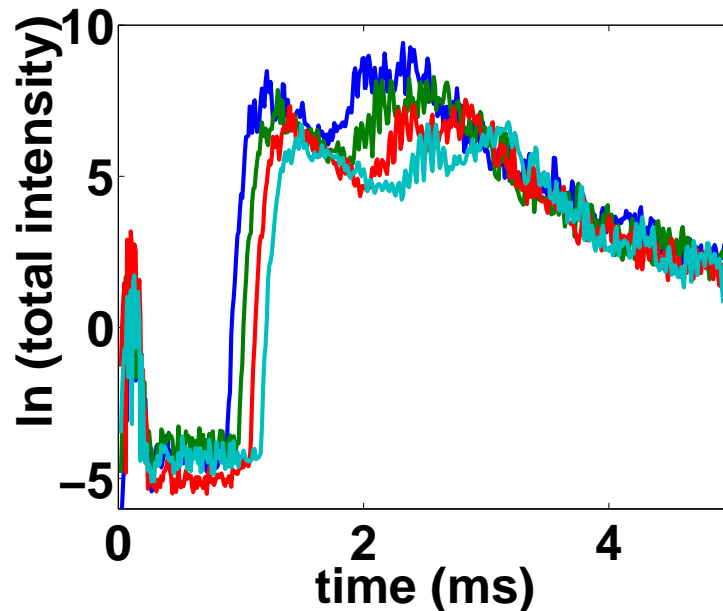


Figure D.3. Total intensities for 4 detectors. The maximum energy on each of the curves is the coherent surface wave. Lighter shaded curves are the intensities for larger source-detector offsets.

is the average of each squared trace, and the coherent intensity is the square of the mean of the traces (Scales & van Wijk, 1999). The incoherent intensity is the difference between total and coherent intensity. For illustration, I have plotted the intensities for four receivers in Figure D.3. It is assumed that waves travel only in the vertical direction, making the problem 1D. One can observe a decay of the coherent arrivals for P-, S- and surface waves, followed by a more-or-less exponential decay of the coda.

D.3 Fitting the data

The radiative transfer model in 1D lets us fit the coherent and the incoherent intensity. This is the key to the separation of scattering from absorption. Since we do not have the source signature, we can only determine the total mean free path from the decay of the coherent maximum. I only use the Stoneley coherent energy and all arrivals after that, assuming that they are multiples of the Stoneley wave. This gives us

$$1/l_a + R/l_s = 2.5 \text{ m}^{-1},$$

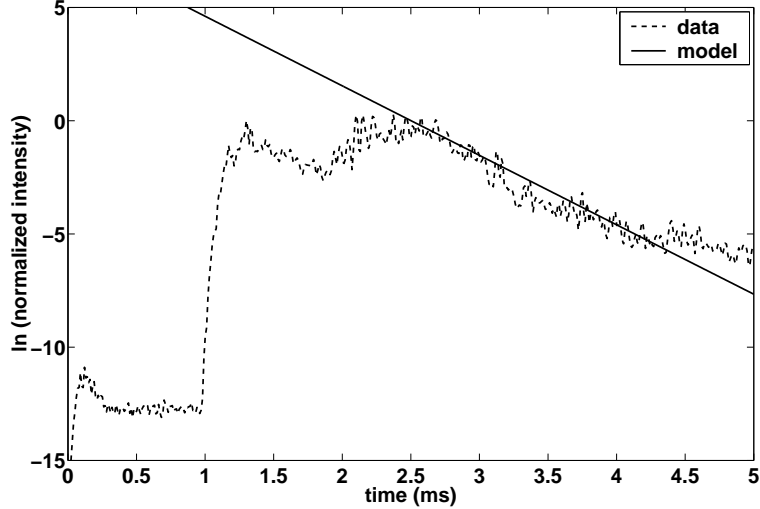


Figure D.4. The dashed line is the incoherent intensity for receiver 4. The solid line is the estimate of the incoherent intensity obtained with radiative transfer, for scattering attenuation $Q_s = 250$ and intrinsic absorption $Q_a = 10$.

with a 5 percent variance in the estimate. From fitting the incoherent intensity, we find that

$$l_s/R = 10 \text{ m} \quad \text{and} \quad l_a = 0.4 \text{ m},$$

where the variance in the estimate of the scattering mean free path is 2 percent. Especially the estimate of the absorption is very sensitive to small changes, suggesting it is well resolved. Estimates with the other 7 receivers give the same numbers, but are left out to not clutter this study.

D.3.1 Relating to Q

Relating the mean free paths to the quality factor Q , which is defined as a decay-rate per cycle, we find that

$$Q = \frac{2\pi fl}{v}. \quad (\text{D.1})$$

This means that $Q_a = 10$ and $Q_s = 250$, which are not un-physical values, but need further studies to determine the validity. However, the variance in these estimates is less than 5 percent, suggesting the estimate is stable. The bias in these estimates are left for future studies: How bad is the 1D assumption? What part of the energy travels only through the borehole, instead of the formation?

Note that the incoherent P-wave energy displays a similar decay, so maybe the same analysis as presented here for the S-waves can be performed on it.

D.4 Discussion

The right panel of Figure D.2 suggests that the statistical properties of the geology vary with depth. Clearly, one can see that especially the deep part of the borehole shows coherent reflectors, even at late times. Therefore, a more precise treatment of this data set should separate the data in regions of similar data characteristics. In this case, we merely want to point out the possibility of an analysis with radiative transfer theory.

A possible problem with an interpretation of the multiply scattered sonic waves, is that we are sampling a mix of the mud in the bore-hole and the formation, but the advantage of sonic logging is that source-receiver pairs moving down the hole form an ensemble measurement. A Vertical Seismic Profile (VSP) might give us the best of both worlds, since it samples the formation only. There, we would have to separate up- from down-going energy in the FK-domain to use the down-going energy as the source, but poses no large problems, as this is already done routinely.

D.5 Conclusions

The characteristics of the sonic data suggests that waves are multiply scattered in and around the borehole. These late arrivals are necessary to estimate intrinsic absorption, a strong fluid indicator. Under some strong assumptions, radiative transfer estimates of scattering and absorption Q , separately. The challenges ahead are to separate the influence from the mud and the formation and to test if attenuating parameters can be linked to geology and the fluid content of the rock.

Appendix E

The angle-beam transducer source

Recent research has shown that the view of ray paths propagating through anomalies in the Earth are the ones most influenced by this anomaly, is not correct. In fact, these rays return to their unperturbed stage after several wavelengths, while the rays off to the side of the anomaly are perturbed most. This has potentially large implications in ray-based imaging. Laboratory data supports this view and provides a tool to further analyze this behavior called wave-front healing (Nolet & Dahlen, 2000).

A plane surface wave hits a scatterer roughly the size of the dominant wavelength (Figure E.1). We have 81-by-81 receivers in the 20-by-20 mm² shaded region, but shown in Figure E.2 are two cross-lines of data. Line 1 is close to the scatterer, while line 2 is roughly three wavelengths past the scatterer. Disturbances on the plane wave are visible on line 2, but the wavefront has *healed* directly behind the scatterer. We have 40 lines of data between lines 1 and 2, so we can *track* the healing process, to see if the wavefront behaves as predicted in the theory of Nolet & Dahlen (2000).

Appendix E. The angle-beam transducer source

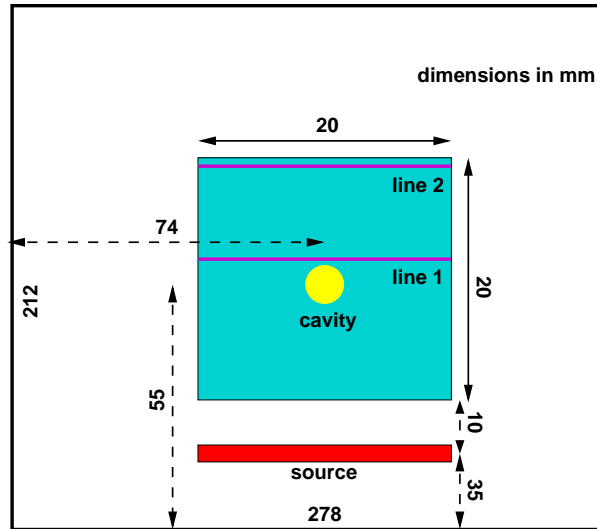


Figure E.1. Plan-view of the experiment. Note the locations of data lines 1 and 2.

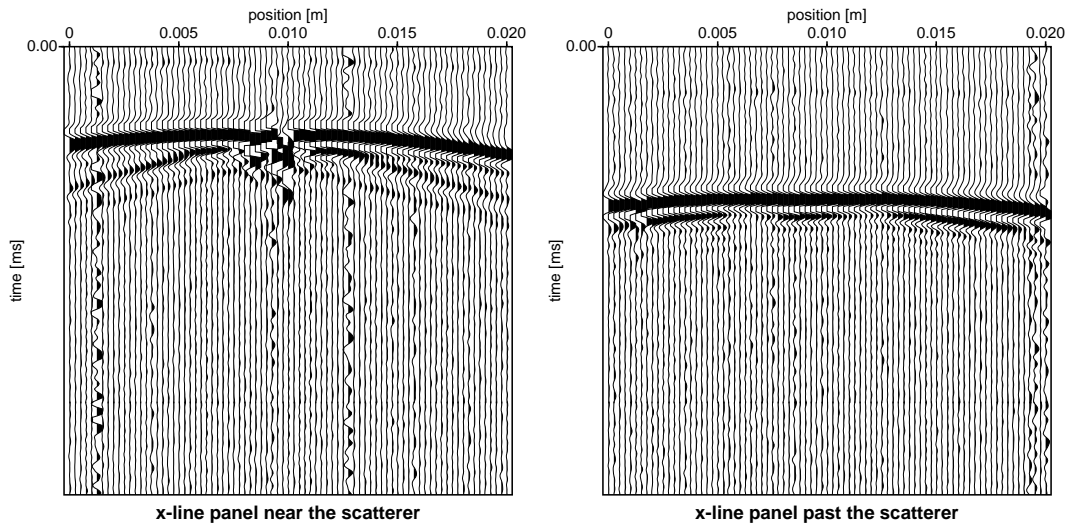


Figure E.2. Data at the receivers on line 1 and 2. While the influence of the scatterer in line 1 is clear in the traces nearest the cavity, line 2 shows that the wavefront healed in the shadow zone behind the scatterer.